Investigations of disorder, extraordinary transmission, and polarization conversion in photonic crystals

by
Mag. Oleksandr Glushko
submitted in fulfillment of the requirements for the degree of
Doktor der montanistischen Wissenschaften
at the Institute of Physics
Montanuniversitaet Leoben, Austria

Under supervision of
Em.O.Univ.-Prof. Dr. Friedemar Kuchar
and
Ao.Univ.-Prof. Dr. Ronald Meisels

refereed by
Ao.Univ.-Prof. Dr. Ronald Meisels
and
Prof. Dr. DI. Kurt Hingerl

February 2011

Eidesstattliche erklärung

I declare in lieu of oath, that I wrote this thesis and performed the associated research myself, using only literature cited in this volume.

Leben, December 2010

Oleksandr Glushko

Abstract.

The rising demand for new materials for controlling light signals at a micrometer scale is a general trend in development of optics and photonics during last two decades. Among such promising new materials are photonic crystals – composite structures where the dielectric constant depends periodically on the spatial coordinates. Photonic crystals can exhibit frequency regions of total reflection which are known as photonic band gaps. In addition, the optical properties of photonic crystals (e.g. spectral positions of the band gaps) can be easily varied by a proper choice of their geometry or even dynamically.

This thesis presents investigations of several aspects of photonic crystal properties and applications.

The influence of the surface roughness of 1D photonic crystals was investigated theoretically and experimentally. The calculated transmission spectra showed high robustness of the lowest band gap to surface roughness. With increasing frequency the effect of surface roughness on transmittance becomes more pronounced: the gaps become shallower and narrower; between the gaps the interference fringes smear out and the average transmittance decreases. The experimental transmission spectra are found to be in a very good agreement with the calculations. We believe that our results provide a fast and convenient way to estimate whether imperfections during the fabrication of a submicron 1D PhC will affect its transmission and reflection properties.

The effect of disorder on the reflection peak of dilute 3D colloidal photonic crystals with bcc lattice was investigated by means of 3D FDTD calculations. In the case of disorder in the radii only a high amount (40% and more) has a visible effect on the reflection peak. Positional disorder decreases the maximal value of the peak only if the spheres are randomly shifted out of the (110) planes. Random removal of 20% of silica spheres from the structure results in a clearly visible decrease of the maximum of the reflection peak. We did not observe any broadening of the reflection peak as effect of disorder – only the maximal value is reduced.

In the last Chapter of this thesis we explore the effects of extraordinary transmission and polarization conversion observed in 2D photonic crystal slabs covered with a metal layer. It was shown that these effects occur due to resonant coupling of the incident wave to specific doubly-degenerate photonic crystal eigenmodes with dipole symmetry. The excited modes are localized within a subwavelength distance below the metal and are polarized perpendicularly to the polarization of the incident wave. Beyond the fundamental interest the presented effects can be utilized for the improvement of the sensitivity of quantum well infrared photodetectors, to coupling of light to planar photonics elements or for the fabrication of transparent metal contacts.

Zusammenfassung.

Im Verlauf der letzten zwei Dekaden wuchs der Bedarf an neuen Technologien zur Beeinflussung der Lichtausbreitung auf der Mikrometer-Skala deutlich an. Eine vielverspechende Technologie beruht auf den sogenannten Photonischen Kristallen (PhC) – Strukturen, in denen die Dielektrizitätskonstante örtlich periodisch ist. PhC können Frequenzbereiche mit Totalreflexion - “Photonische Bandlücken” aufweisen. Außerdem können die optischen Eigenschaften der PhC, etwa die Lage der Bandlücken, durch Veränderung der Geometrie, aber auch dynamisch, verändert werden.

Diese Arbeit behandelt wesentliche Aspekte der PhC und deren Relevanz für Anwendungen.

Ein solcher Aspekt ist die Auswirkung von Unordnung in der Kristallstruktur. Diese wurde an nominell ein-dimensionalen (1D) Strukturen mit Oberflächenrauheit untersucht. Die berechneten Spektren der Transmission zeigen eine hohe Widerstandsfähigkeit der untersten Bandlücke gegenüber der Oberflächenrauheit. Bei höheren Frequenzen wird der Einfluss der Rauheit deutlicher: die Lücken weren schmäler und die Transmission dort größer; in den Bereichen dazwischen werden die Fabry-Perot Muster verschmiert und der Mittelwert der Transmission sinkt. Experimentelle Spektren weisen eine gute Übereinstimmung mit den Berechnungen auf. Dies bestätigt, dass auf diese Weise auf schnelle Weise festgestellt werden kann, inwieweit Unregelmäßigkeiten bei der Herstellung Einfluss auf die Transmissions- und Reflexions-eigenschaften eines 1D PhC haben.

Weiters wurde der Effekt der Unordnung an 3D kolloidalen PhC aus Quarz-Mikrokugeln mit krz Gitter mit FDTD Rechnungen untersucht. Bei den Radien hatten nur Variationen von mehr als 40% einen deutlichen Einfluss auf die (110) Bragg-Reflexions-Maxima. Bei positioneller Unordnung wirkten sich nur Verschiebungen der Kugeln aus den (110)-Ebenen heraus. Erst eine Leerstellendichte von 20% bewirkte eine deutliche Erniedrigung, aber keine Verbreiterung, der Maxima.

Schließlich wurden der EOT-Effekt (außerordentliche Transmission) und die Umwandlung der Polarisation durch einseitig goldbeschichtete Plättchen mit PhC Struktur untersucht. Es wird gezeigt, dass diese Effekte in der resonanten Kopplung zu bestimmten Eigenmoden der Struktur mit Dipolsymmetrie begründet sind. Diese Moden sind in einem Bereich weniger μm unter der Goldschicht lokalisiert und dort normal zur ursprünglichen Richtung polarisiert. Abgesehen vom theoretische Interesse können die behandelten Effekte zur Verbesserung der Empflindlichkeit sogenannter QWIP-Photo-Detektoren, zur Kopplung von Strahlung an integrierte Photonik, oder für (wenn auch schmalbandig) transparente Metall-Kontakte verwendet werden.

CONTENTS

Chapter 1. Background

1.1. Photonic crystals

In this section we provide the fundamentals of photonic crystals including the basic properties and definitions, historical overview, and some most important applications.

1.1.1 Basic properties and definitions

Photonic crystals (PhCs) are materials where the refractive index is a periodic function of the spatial coordinates. Depending on the number of the directions of the periodicity PhCs can be classified in one-, two-, or three-dimensional (Fig. 1.1). In other words, a photonic crystal is a superlattice with spatially varying refractive index. Under certain conditions an electromagnetic wave propagating through such a periodic structure can experience a destructive interference. In this case one can say that the propagation of such a wave is *forbidden*, and the frequency region where the propagation is forbidden is called *photonic band gap*. From the theoretical point of view, an electromagnetic (EM) wave with the frequency lying in a photonic band gap does not have propagating solutions inside the PhC, it can be only exponentially decaying. Thus if a PhC consists of two loss-less dielectric materials, then the photonic band gap regions should reveal themselves by 100 % reflectance. The concept of the photonic band gap can be most easily demonstrated on the example of 1D PhCs or Bragg reflectors (Fig. 1.1a) whose property to exhibit spectral ranges of perfect reflectance is well-known for more than 50 years [1].

The presence or absence of a photonic band gap in a PhC depends on three main structural parameters. The first is the optical contrast, i.e. the ratio of the dielectric constants of the constituents $\varepsilon_a/\varepsilon_b$. Generally, PhCs with higher contrast have spectrally larger photonic band gaps. The second is the symmetry of the superlattice and the shape of the "atoms". For instance, a 2D PhC shown in Fig. 1.1b has circular 2D "atoms" with radius R arranged in a hexagonal lattice with lattice constant a. And the third parameter is the filling fraction f_a, namely, the fraction of the volume which is occupied by a material with ε_a.

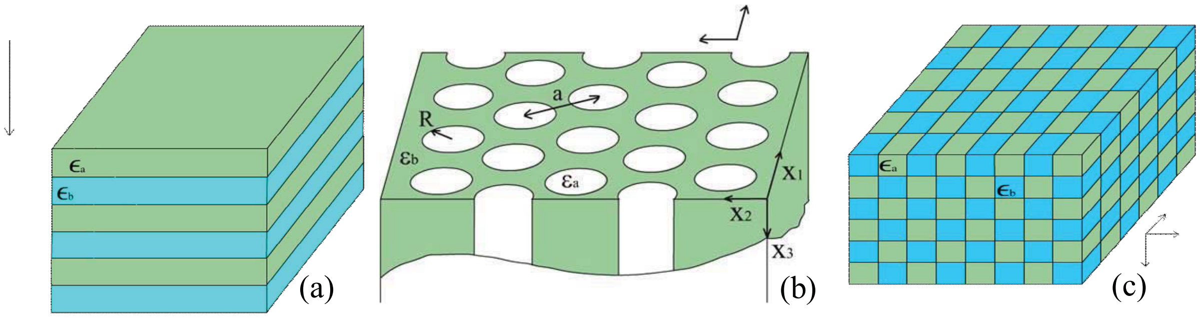

Fig. 1.1. Schematic examples of 1D (a), 2D (b), and 3D (c) photonic crystals. The arrows show the directions of periodicity

The interaction between an EM wave and a PhC depends also on the parameters of the wave. In addition to the frequency, the polarization and propagation direction of a wave are also important. In a 3D PhC it is possible to observe an *absolute* or *complete* photonic band gap which is independent of the propagation direction as well as of the polarization. In 2D PhCs an absolute band gap is usually understood to be a polarization-independent band gap for the waves propagating in the plane of periodicity. A photonic band gap which exists for all propagation directions is also called *omnidirectional*. If a photonic band gap exists only for a specific propagation direction then it is called a *pseudogap* or an *unidirectional* band gap. In 2D structures the waves propagating in the plane of periodicity can be split into TE (the magnetic field is perpendicular to the plane of periodicity) and TM (the electric field is perpendicular to the plane of periodicity) polarized. If a photonic band gap exists only for a particular polarization then it is called TE or TM photonic band gap.

Another important property of PhCs is their scalability. The interference of an EM wave on a periodic superlattice is defined by the period of the superlattice. Thus, by proper choice of the periodicity of a PhC the spectral position of a photonic band gap can be

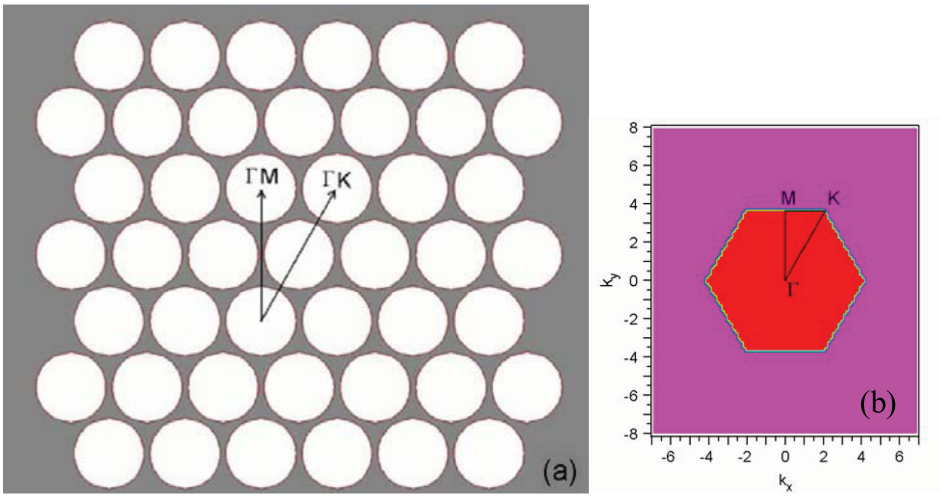

Fig. 1.2. (a) The scheme of the 2D PhC with triangular lattice. The white circles are the air pores and the grey background is the high-index material. The arrows show the Γ-M and Γ-K directions of a wave propagation. (b) The first Brillouin zone for triangular lattice. The black triangle is the irreducible part of the Brillouin zone. Γ, M, and K are the high-symmetry points.

varied from the UV part of spectrum to the microwave by increasing the structural dimensions.

In order to visualize the basic properties of photonic crystals let us consider a 2D periodic structure consisting of a triangular lattice of air holes embedded in a dielectric medium with the following parameters: the dielectric constant of the dielectric meduim ε_b=12, the dielectric constant of the pores ε_a=1, radius of the pores R=0.46a, where a is the lattice constant of the triangular lattice. Figs. 1.2a and 1.2b show the scheme of such photonic crystal and the first Brillouin zone of the triangular lattice, respectively.

In Figs. 1.3a and 1.3b the *photonic band structures* of such 2D PhC are shown for TM and TE polarization, respectively. A photonic band structure, by analogy with electronic band structure of solid state, shows the eigenfrequencies for different values of the quasi-wavevector. The values of the quasi-wavevector are usually taken from the edge of the irreducible part of the Brillouin zone (see Fig. 1.2b). The hatched areas on both plots depict the frequency regions where there are no propagating eigenmodes – the photonic band gaps.

It is necessary to note that in the photonic crystal literature the so-called reduced frequencies are commonly used. The reduced frequencies expressed as $\omega a/(2\pi c)$ (ω is the angular frequency, c is the speed of light) or a/λ (λ is the wavelength in vacuum) reflect the fact that the spectral properties of a PhC scale with the period of the lattice. For instance, the spectral position of the band gap shown in Fig. 1.3a is from 0.407 to 0.460 reduced frequencies. If the period of the structure is a = 1 μm than the band gap will be located between λ=2.17 μm (a/λ=0.46) and λ=2.46 μm (a/λ=0.407). Of course, one should take into account, that the properties of the constituent materials (e.g. dielectric constants) can be different in different spectral regions.

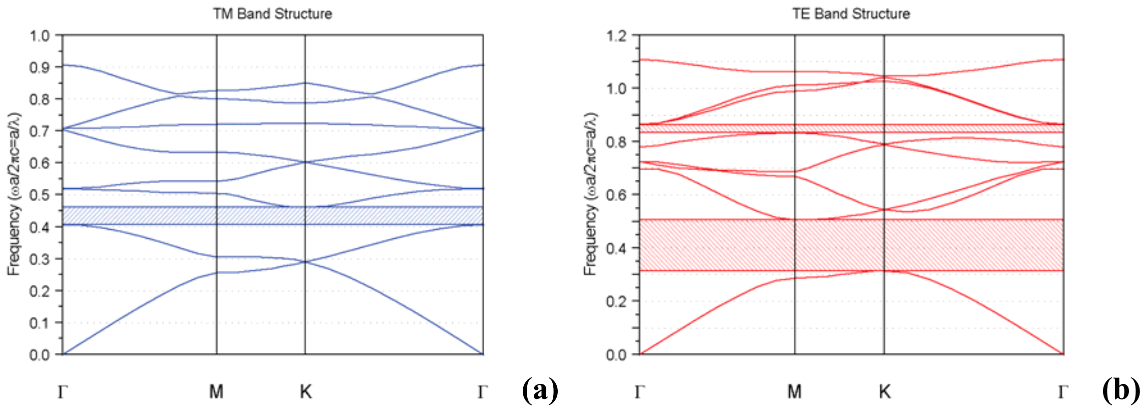

Fig. 1.3. The TM (a) and TE (b) photonic band structure of a 2D triangular lattice photonic crystal. The 8 lowest dispersion curves are shown. The hatched areas depict the photonic band gaps.

The considered structure exhibits omnidirectional band gaps for TM and TE polarization as shown in Fig. 1.3. The spectral region where TE and TM gaps exist simultaneously would be an absolute band gap. In current case the absolute band gap coincides with the TM band gap being located at reduced frequencies between 0.407 and 0.460.

A photonic band structure is defined by the eigenmodes of a perfectly periodic infinite system. In reality one always deals with spatially finite samples. Moreover, excitation as well as detection is usually performed externally meaning that the source and the detector are located outside the sample. Thus, a question arises:

How are the intrinsic properties of a PhC (such as the band structure) connected with the experimentally measurable extrinsic properties (such as transmittance and reflectance)?

To answer this question let us consider the transmittance of a 2D PhC with the same parameters as in the band structure calculations shown in Fig. 1.3. The structure is now spatially finite having 7 rows of pores in the direction of the EM wave propagation. The calculations are performed by the finite-difference time-domain method (FDTD). Figs. 1.4a and 1.4c show the transmittance of TM-polarized waves propagating in Γ-M and Γ-K directions, respectively. The TE spectra are shown in Figs. 1.4b and 1.4d for Γ-M and Γ-K directions, respectively. Above each spectrum the corresponding part of the band structure is plotted. The vertical red dashed lines depict the edges of the *unidirectional* band gaps. Since the constituent materials are loss-less (no absorption) the reflectance can be deduced by the simple formula R=1-T, where R is the reflectance and T is the transmittance.

One should mention that the omnidirectional band gaps shown in Fig. 1.3 appear in all transmission spectra as regions with virtually zero transmittance. Besides, each spectrum exhibit additional low transmittance areas which correspond to the unidirectional gaps. For instance, the spectrum for Γ-M direction and TM polarization (Fig. 1.4a) has three low-transmittance regions.

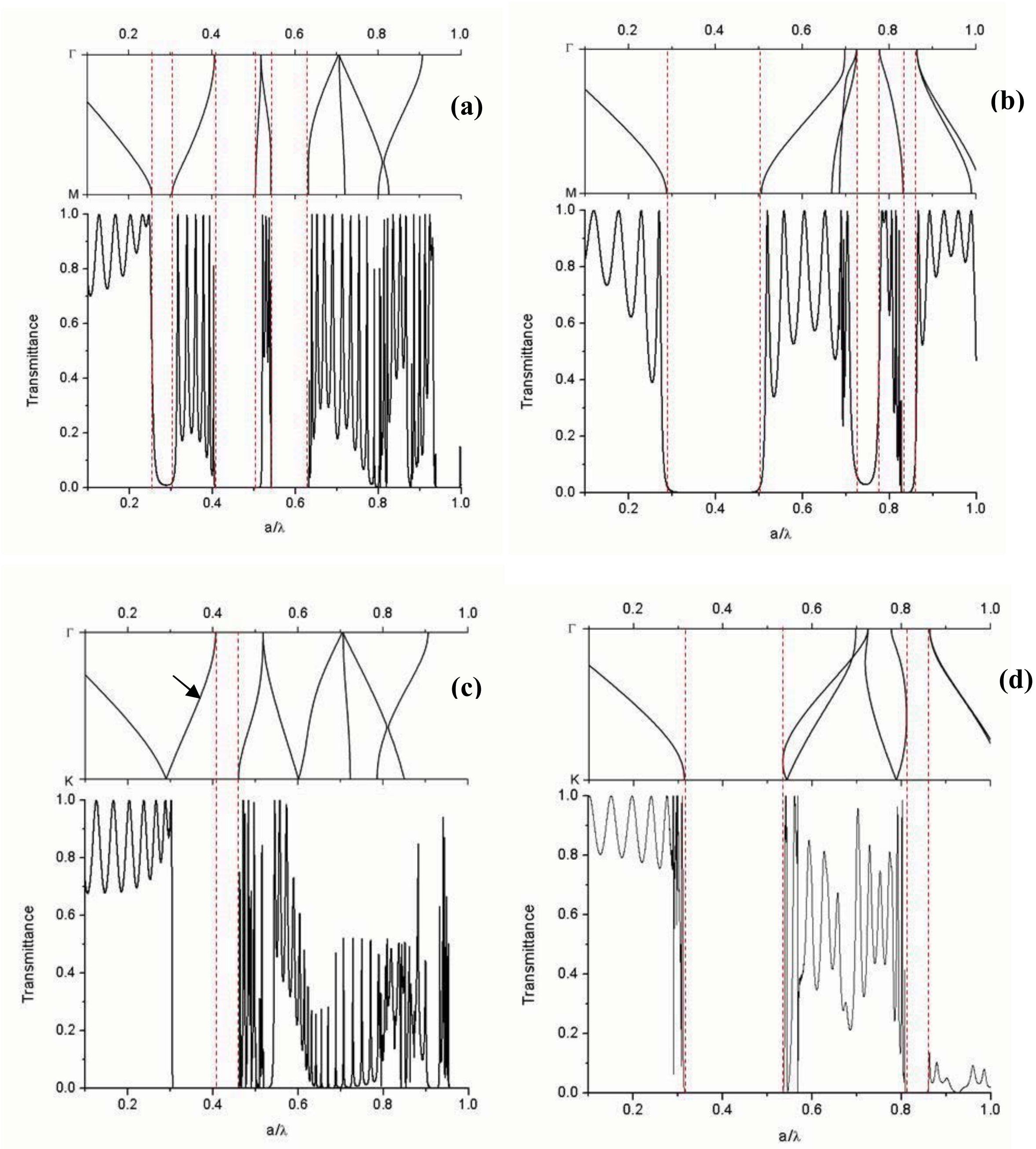

Fig. 1.4. Calculated transmission spectra for a finite 2D PhC with the same parameters as in Fig. 1.3 for (a): Γ-M direction and TM polarization; (b) Γ-M direction and TE polarization; (c): Γ-K direction and TM polarization; (d): Γ-K direction and TE polarization. On the top of each spectrum the corresponding part of the band structure is shown. The vertical red dashed lines show the edges of the unidirectional band gaps. The arrow in (c) points onto the eigenmode with odd symmetry which does not couple to external plane waves.

However, the presented transmission spectra have more complicated structure due to several effects:

(i) Our 2D photonic crystal is surrounded by air. Therefore, the interference between the waves reflected from the PhC-air interfaces results in the appearance of Fabry-Perot interference fringes within the transmission bands of the photonic crystal. This effect is most clearly seen in the low-frequency part of the spectra below the first band gap. In these regions the wavelength is much larger than the period and the radius of the holes and the PhC can be approximated by a homogeneous slab with some effective refractive index. At the higher frequencies (lower wavelengths) the interferences between the pores and within a single pore are superimposed with interferences from the PhC-air interfaces resulting in complex and "spiky" transmission spectra.

(ii) A photonic band gap is by definition a property of an infinite periodic structure. Since we consider a finite structure with only 7 rows of pores in the propagation direction, the transmittance within some unidirectional gaps does not go to zero. Particularly, within the first gap in Fig. 1.4a the transmittance is about 1% and for the second gap in Fig. 1.4b the transmittance is more than 3%. For all other gaps (both uni- and omnidirectional) the transmittance is below 0.01%.

(iii) The transmission minimum in Fig. 1.4c is much larger than the corresponding gap. This is because the eigenmodes lying in the second band (marked by arrow) for Γ-K direction in TM band structure cannot be excited from the outside. To be more precise, an *external* plane wave cannot *couple* to these *eigenmodes* of the photonic crystal. This happens because these eigenmodes are antisymmetric with respect to the propagation axis while the incident plane wave is always symmetric. The "symmetry mismatch" between the eigenmodes of a PhC is discussed in details in [2].

1.1.2. Historical overview

The discovery of photonic crystals is usually attributed to the pioneering works of Yablonovich [3] and John [4]. In these works periodic three-dimensional superlattices are proposed to be used for controlling the processes of spontaneous emission in semiconductors. It was assumed that if a periodic superlattice is designed in such a way that the frequency of photons emitted by electrons is lying in a photonic band gap then such electronic transitions would become forbidden.

The first photonic crystals were experimentally fabricated in 1989 by Yablonovich and Gmitter [5] and had a fcc lattice with a lattice constant of approximately 12 mm. Although several tens of PhCs with different dielectric constants and filling fractions were fabricated, a photonic band gap was observed in only one case (Fig. 1.5a). These results were in controversy with theoretical calculations of photonic band structure [6, 7] based on the scalar-wave approximation (the vector nature of EM waves is not taken into account) which predicted that a photonic band gap should be observed for a wide spectrum of PhCs configurations. This lack of a proper theoretical model was mentioned in the experimental work [5] with the following expression: "This tedious cut-and-carry approach was very time consuming, but it tended to ensure that no possibilities were overlooked".

In 1990 three groups reported on full vector calculations of a photonic band structure of 3D PhCs by means of the plane-wave expansion method (PWEM) [8, 9, 10]. In Fig.

1.5b a photonic band structure calculated in [10] for the same PhC configuration as in experiments of [5] is shown. Despite a good general agreement between experimental (Fig. 1.5a) and theoretical (Fig.1.5b) band structures in the latter case a photonic band gap does not appear. It was shown also in [8, 9] that an absolute photonic band gap does not appear in PhCs with fcc lattice due to the degeneracy of the dispersion curves in the U and W symmetry points of the Brillouin zone. Later, Eli Yablonovich published a review on his first efforts of experimental observation of photonic band gap [11] where he admitted that the band structure exhibiting a band gap (Fig. 1.5a) "harbored a serious error". The "error" leading to the disappearance of the degeneracy of the dispersion curves in the points U and W was attributed to the finite size of the experimentally fabricated structure.

However, theoretical calculations showed not only proofs of the absence of photonic band gaps: in [8] was shown that a *diamond lattice* of spherical "atoms" exhibits a full photonic band gap for a wide spectrum of dielectric constants and filling fractions.

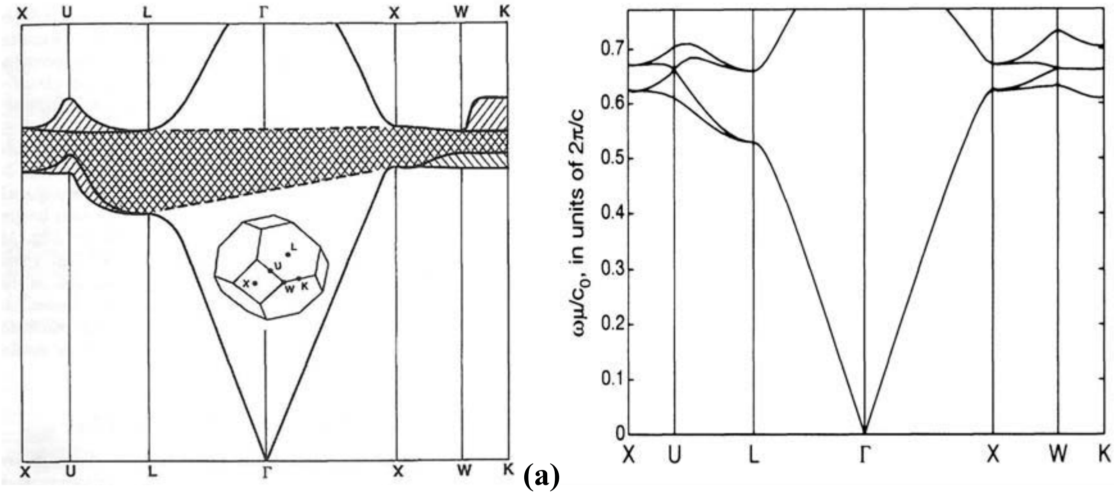

Fig. 1.5. (a) Experimentally measured photonic band structure reported in [5]; (b) Theoretically calculated band structure for the same PhC as in the case (a) [10]

This success in the theoretical description of PhCs properties inspired scientists to new experimental efforts. In [12] a new type of PhCs was proposed: fcc lattice with non-spherical "atoms". A 3D lattice was created by drilling cylindrical holes in three different directions at an angle of 35.26° to the surface normal (Fig. 1.6a). Due to the nonsphericity of the "atoms" the degeneracy of the bands was lifted up and a clear band gap between 13 and 16 GHz appeared in the measurements. This PhC configuration was called "Yablonovite" in honor of Eli Yablonovich. Another configuration of 3D PhC called "woodpile" was proposed in [13, 14, 15]. A PhC shown in Fig. 1.6b was made of Al_2O_3 rods with a diameter of 0.318 cm and length of 15.24 cm. The structure was formed layer-by-layer, the rods in each successive layer were rotated at 90 degrees with respect to the previous one. The resulting PhC had a face-centered tetragonal lattice with lattice constant of 1.123 cm and an alumina filling factor of 0.26. Experimentally measured photonic band gap was located between 11.9 GHz and 14 GHz which was in good agreement with the theoretical calculations (11.7 GHz – 13.7 GHz).

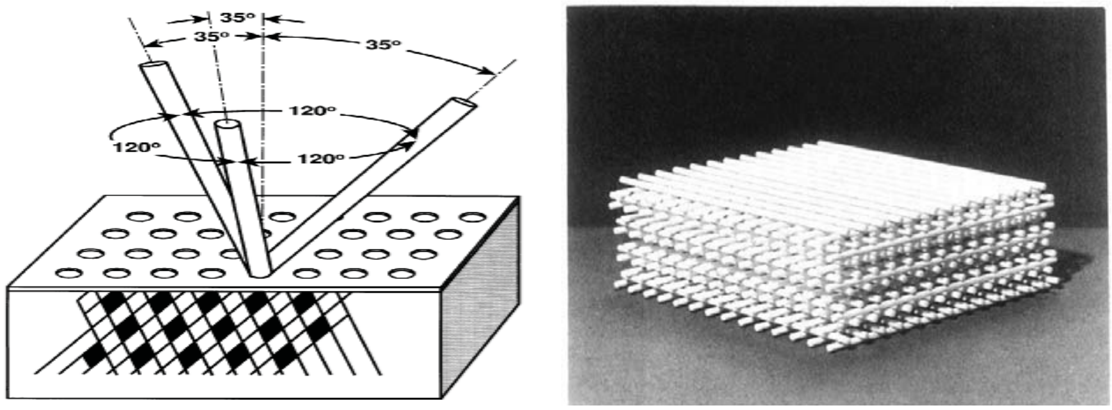

(a) **(b)**

Fig. 1.6. Configurations of three-dimensional PhC with absolute photonic band gap. (a): "Yablonovite" [12]; (b): "Woodpile" [15].

The PWEM was also applied to calculations of 2D photonic crystals [16, 17, 18, 19]. Various configurations of 2D PhCs were investigated: triangular and square lattice, high-index rods in air and pores in high-index material, circular and square "atoms". It was found out that, as a rule of thumb, 2D lattices of high-index rods exhibit rather TM band gaps while TE band gaps are favored in 2D lattices of pores in a high-index background. An absolute band gap was found to appear in a triangular lattice of air pores in a background material with $\varepsilon=13$ at high values of air filling factor (>0.7). Experimentally, a 2D photonic band gap was measured for the first time in [20] at microwave frequencies.

The end of 1990's and the beginning of 2000's was characterized by a rapid grow of interest in photonic crystals. New fabrication methods, new simulations techniques as well as a number of possible applications of photonic crystals were proposed in that time. Quantitatively, the number of publications concerning various aspects of photonic crystals was growing nearly exponentially till the year 2005 that is shown in Fig. 1.7. A detailed review of all significant papers concerning photonic crystals is out of scope of this thesis. However, the most interesting applications are shortly reviewed in the next subsection.

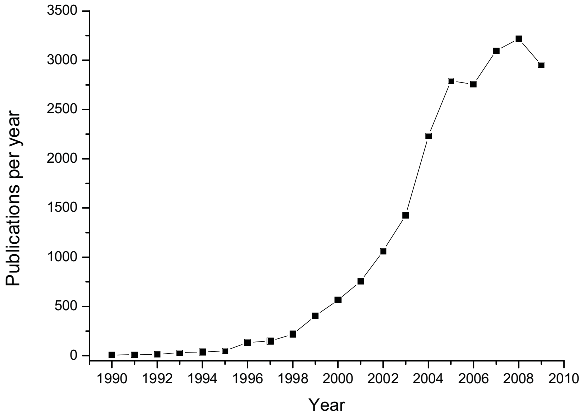

Fig. 1.7. Dynamic of publications concerning various aspects of photonic crystals. Obtained from www.scopus.com.

1.1.3. Applications

In this subsection we provide a short review of some applications of photonic crystals.

Cavities and waveguides. Photonic crystal cavities are based on the property of the defects (e.g. a missing pore in a 2D PhC) in otherwise periodic structures to confine the light if the frequency lies in a band gap of the PhC. A waveguide can be realized by a line defect (e.g. missing row of pores in a 2D PhC).

The first experimental observation of a defect state in a PhC was reported in [20]. The experiment was performed at microwave frequencies on a 2D PhC consisting of a square lattice of alumina rods in air. The defect was presented by a missing rod in an otherwise periodic structure. The measured distribution of electromagnetic power around the defect is shown in Fig. 1.8

The defect modes in 3D "Yablonovite" structure were observed in. [21]. A donor

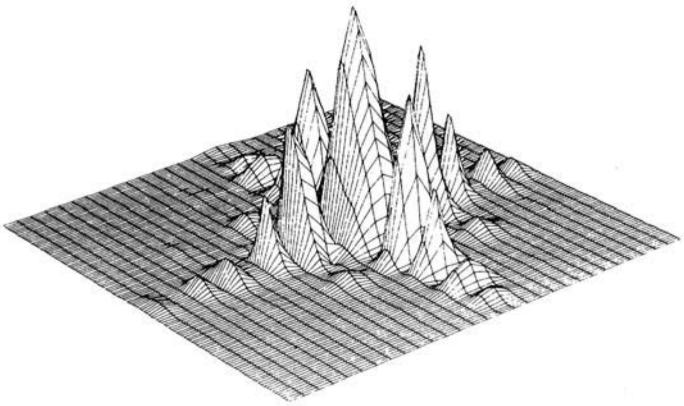

Fig. 1.8. The spatial power distribution around a defect in a 2D PhC created by removing a single rod. Taken from [20].

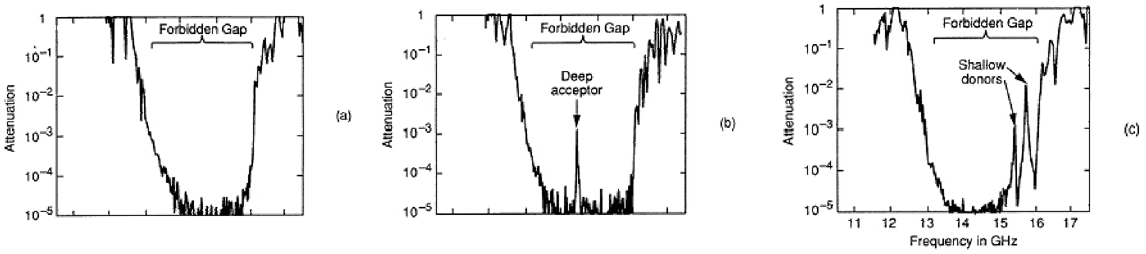

Fig. 1.9. Transmission spectra of Yablonovite crystal with (a) no defects, (b) acceptor defect, and (c) donor defect. Taken from [21].

(acceptor) defect was created by adding (removing) high-index material inside a single unit cell. The transmission measurements showed additional peaks attributed to the created defect states (Fig. 1.9).

The possibility of guiding of light by a line defect in a 2D PhC was discussed in [22]. The authors proposed to use a photonic band gap to confine light in the plane of periodicity and to use total internal reflection to confine light in the third direction. It was supposed that such waveguides will have "ideal properties for compact waveguide devices".

Excellent waveguiding properties of PhC waveguides were confirmed by FDTD calculations [23]. The transmittance through a 90° waveguide bend was found to be as high as 98%. Almost 100% transmission through a sharp 90 degree bend was confirmed also experimentally in the microwave regime [24].

A 2D photonic crystal waveguide with the operation wavelength of 1.55 μm was designed and fabricated on a silicon-on-insulator substrate in [25]. The SEM image of the fabricated structure is shown in Fig. 1.10. The guiding of light through 60° and 90° bends was confirmed by direct experimental measurements. 2D PhC where the thickness of the structure is less than or of the same order as the wavelength are commonly called "photonic crystal slabs".

It was shown in [26] that light propagating through a line defect in a 2D PhC can effectively couple to a point defect created in the vicinity. Experimental measurements showed that by a proper design of the point defect it can act as a cavity with a Q-factor as high as 100 000 and the mode volume as low as 0.71 $(\lambda_0/n)^3$, where λ_0 is free-space

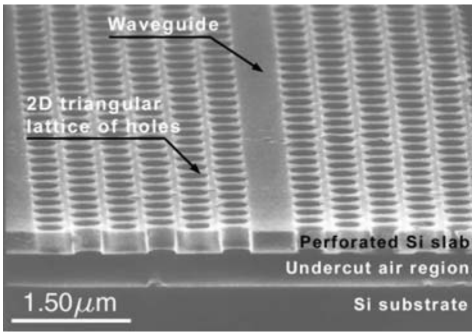

Fig. 1.10. SEM image of a 2D photonic crystal slab designed for operation at 1.55 μm. Taken from [25].

wavelength and *n* is the refractive index of the slab.

To conclude, line defects introduced in 2D photonic crystal opens new possibilities to guide and to control light signals on subwavelength scale and in planar geometry. The ability of point defects to act as effective optical nanocavities led to development of new type of lasers – photonic crystal lasers [27].

Photonic crystal fibers. The principal difference between 2D PhC waveguides and photonic crystal fibers (PCFs) is that in the latter case the light propagates perpendicularly to the plane of periodicity, i.e. along the pores or rods. In other words, a 2D PhC structure is a cladding surrounding the guiding core. Since the light confinement in such fibers is not due to total internal reflection but due to photonic band gap reflection, the core can have any refractive index or even be hollow. Hollow-core fibers are free from scattering, nonlinear and dispersion effects and can be used for high-power guiding. An example of a hollow-core silica-air PCF for operating at wavelengths between 1.4 μm and 1.6 μm is shown in Fig. 1.11 [28]. A number of other important applications of PCFs are proposed so far: sensors [29, 30, 31], terahertz guiding [32, 33], probes for optical microscopy [34, 35], lasers [36, 37].

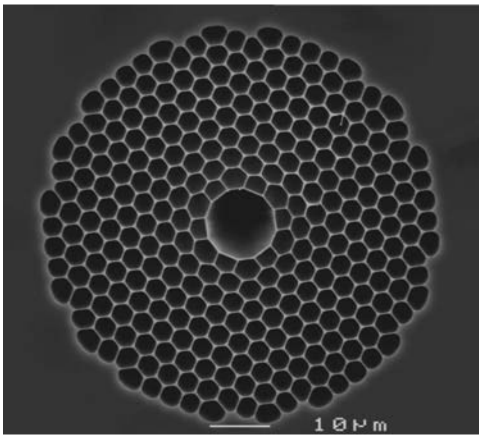

Fig. 1.11. Scanning electron micrograph of a hollow-core silica-air photonic crystal fiber. Taken from [28].

Tunable photonic crystals. Since the spectral positions of photonic bands and gaps depend on structural parameters of a PhC (such as refractive indices, lattice period) a dynamical change of these parameters by some external influence should lead to a dynamical change of PhC spectral characteristics. A PhC which allows to tune its optical properties by an external influence called tunable photonic crystal.

A possibility of tuning spectral characteristics of 2D PhCs by external magnetic or electric field was investigated theoretically in [38]. By analyzing a photonic band structure for different values of the dielectric constant of one of the constituents it was shown that a transition between transparency and opacity is in principle possible.

By filling a 2D macroporous silicon PhC with a liquid crystal a temperature-dependent tuning of the band gap position was shown experimentally and analyzed theoretically in [39].

Ultrafast tuning of the band edge of a 2D macroporous silicon PhC was demonstrated experimentally in [40]. The refractive index of silicon was changed by optically induced free carrier injection. The observed band gap edge shift was about 1.5 % (30 nm) on a picosecond timescale.

In [41] a nonlinear two-photon absorption process was utilized to modify the refractive index of AlGaAs 2D photonic crystals. The spectral shift of photonic band of 5 nm (~0.6 %) was achieved with a respond time below 10 ps.

Strain-tunable PhCs were investigated in [42]. It was shown that by applying a shear strain of 3 % the spectral position of the photonic band gap edges in air-silicon 2D PhC can be shifted up to 9 % with respect to non-strained structure.

Thus, tunable photonic crystals have a great potential to be used for fast control of optical signals, with an ultimate goal of creation of ultrafast all-optical logical elements.

Microwave antennas.

By using total reflection from a 3D PhC the gain and the directivity of a planar dipole antenna was substantially increased in [43].

A monopole antenna placed in a photonic crystal cavity was investigated in [44]. The existence of a 3D photonic band gap allowed to obtain very sharp directionality of the monopole antenna. The calculated (dotted) and measured (solid) radiation patterns of such antenna are shown in Fig. 1.12.

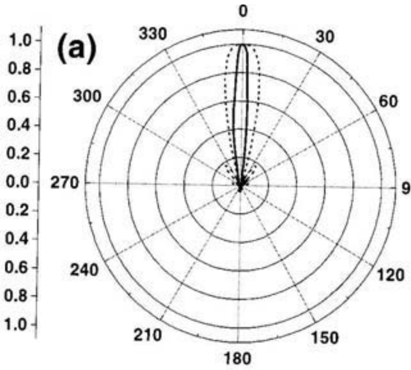

Fig. 1.12. Calculated (dotted) and measured (solid) H-field radiation patterns of the monopole antenna inside a photonic crystal cavity. Taken from [44].

Negative refraction and superlensing.

The effect of negative refraction of visible light in 3D photonic crystals was observed in [45]. It was shown experimentally that the refracted beam was swung from -90° to +90° for a slight change in the incident angle in the range of ±12°. This effect of very strong angular dispersion of light in photonic crystals was called a "superprism" effect.

A lens with subwavelength resolution was demonstrated in [46] by using a 2D PhC in the millimeter wave region. It was shown experimentally that a plane-parallel photonic crystal slab acts as a lens and allows to obtain images with the spot size as small as 0.21λ. Such lenses are commonly called "superlenses".

By combining a superprism with a superlens a compact wavelength demultiplexer was constructed in [47]. The spectral resolution of the proposed device was as small as 0.4 nm at the operating wavelength of 1.55 μm.

1.2. The Plane Wave Expansion Method (PWEM)

The PWEM was initially developed for calculation of an electronic band structure of a solid state. The method is based on the Bloch theorem stating that in infinite and periodic potential the electron wavefunctions are also periodic and can be expanded in a set of plane waves. The same statement can be applied to a photonic crystal: in an infinite structure with periodic refractive index the distribution of the electromagnetic field should be periodic and can be represented as a sum of plane waves. In this section we will show how to derive the basic equations of the PWEM for the case of a 2D photonic crystal as well as how to solve those equations numerically.

1.2.1. Analytical basis

Let us start from the very beginning – from the Maxwell's equations. We will follow the treatment described, for instance, in [16]. In a medium without current sources and charges the Maxwell's equations have a form (in SGS units):

$$\begin{aligned} \vec{\nabla} \times \vec{E} &= -\frac{1}{c}\frac{\partial \vec{B}}{\partial t} \\ \vec{\nabla} \times \vec{H} &= \frac{1}{c}\frac{\partial \vec{D}}{\partial t} \\ \vec{\nabla} \cdot \vec{E} &= 0 \\ \vec{\nabla} \cdot \vec{B} &= 0 \end{aligned} \tag{1.1}$$

If we assume that our electromagnetic field changes in time according to a harmonic law ($\sim e^{-i\omega t}$) and that we have an optically linear medium the first two equations from (1.1) can be rewritten as following:

$$\begin{aligned} \vec{\nabla} \times \vec{E} &= i\frac{\mu\omega}{c}\vec{H} \\ \vec{\nabla} \times \vec{H} &= -i\frac{\varepsilon(\vec{x})\omega}{c}\vec{E} \end{aligned} . \tag{1.2}$$

Please note that dielectric constant is assumed to be coordinate-dependent. By excluding the magnetic field we obtain a single second-order differential equation for the electric field:

$$\vec{\nabla} \times \vec{\nabla} \times \vec{E} = \frac{\omega^2}{c^2}\varepsilon(\vec{x})\mu\vec{E} \tag{1.3}$$

By applying a standard formula of vector analysis $\vec{\nabla} \times \vec{\nabla} \times \vec{E} = \vec{\nabla} \cdot (\vec{\nabla} \cdot \vec{E}) - \nabla^2 \vec{E}$ and splitting the vector equation (1.3) into three scalar component equations we obtain

$$\begin{aligned}
&\frac{1}{\varepsilon(\vec{x})}\left(-\frac{\partial^2 E_1}{\partial x_2^2} + \frac{\partial^2 E_1}{\partial x_3^2} + \frac{\partial^2 E_2}{\partial x_1 \partial x_2} + \frac{\partial^2 E_3}{\partial x_1 \partial x_3}\right) = \frac{\omega^2}{c^2}\mu E_1 \\
&\frac{1}{\varepsilon(\vec{x})}\left(\frac{\partial^2 E_1}{\partial x_1 \partial x_2} - \frac{\partial^2 E_2}{\partial x_1^2} + \frac{\partial^2 E_2}{\partial x_3^2} + \frac{\partial^2 E_3}{\partial x_2 \partial x_3}\right) = \frac{\omega^2}{c^2}\mu E_2 \; . \\
&\frac{1}{\varepsilon(\vec{x})}\left(\frac{\partial^2 E_1}{\partial x_1 \partial x_3} + \frac{\partial^2 E_2}{\partial x_2 \partial x_3} - \frac{\partial^2 E_3}{\partial x_1^2} - \frac{\partial^2 E_3}{\partial x_2^2}\right) = \frac{\omega^2}{c^2}\mu E_3
\end{aligned} \tag{1.4}$$

Equations (1.4) are just a representation of Maxwell's equations (1.2) for a time-harmonic wave in an optically linear medium with coordinate-dependent dielectric constant. We want to find a solution for a dielectric structure that consists of a periodic array of infinitely long, parallel rods of circular cross-section, characterized by the dielectric constant ε_a, embedded in a medium of dielectric constant ε_b (Fig. 1.13).

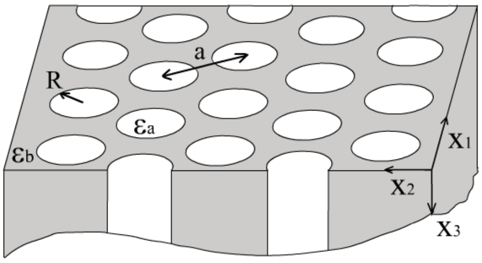

Fig. 1.13. The scheme of a two-dimensional photonic crystal.

The two-dimensional Bravais lattice formed by the intersection of the axes of the rods with the x_1x_2 plane is defined by the two primitive translation vectors $\vec{a}_1$ and $\vec{a}_2$, so that the lattice points are given by the vectors

$$\vec{X}_{II} = l_1\vec{a}_1 + l_2\vec{a}_2 \, ,$$

where l_1 and l_2 are any integers, positive, negative or zero.
The lattice points of the corresponding reciprocal lattice are given by the vectors

$$\vec{G}_{II} = h_1\vec{b}_1 + h_2\vec{b}_2 \, ,$$

where the primitive translation vectors $\vec{b}_1$ and $\vec{b}_2$ are defined by the equations

$$\vec{a}_i\vec{b}_j = 2\pi\delta_{ij} \, , \; i\,, j = 1,2.$$

while h_1 and h_2 are integers or zero.

The dielectric constant of the system we study here is independent of the x_3 coordinate, and we denote it by $\varepsilon(\vec{x}_{II})$. The vector $\vec{x}_{II} = \vec{e}_1 x_1 + \vec{e}_2 x_2$, where $\vec{e}_1$ and $\vec{e}_2$ are unit vectors along the x_1 and x_2 axes, respectively, is the projection of the vector $\vec{x}$ onto the x_1x_2 plane. We assume here that the dielectric constant satisfies the following periodicity relations:

$$\begin{aligned} &\varepsilon(\vec{x}_{II} + \vec{X}_{II}) = \varepsilon(\vec{x}_{II}) \\ &\varepsilon^{-1}(\vec{x}_{II} + \vec{X}_{II}) = \varepsilon^{-1}(\vec{x}_{II}) \end{aligned} \tag{1.5}$$

We will search for a solution for the electric field of the form

$$E_\alpha(\vec{x}) = E_\alpha(\vec{x}_{II}) \exp(ik_3 x_3) \exp(-i\omega t), \alpha = 1,2,3 \tag{1.6}$$

which represents the symmetry of the considered structure, namely the dependence of the electric field on x_3 coordinate is simply harmonic. Below we will omit the time-harmonic part $\exp(-i\omega t)$ of the fields for simplicity. After substitution (1.6) into (1.4) and assuming non-magnetic materials (μ=1) we obtain:

$$\begin{aligned} &\frac{1}{\varepsilon(\vec{x}_{II})}\left(-\frac{\partial^2 E_1}{\partial x_2^2} + k_3^2 E_1 + \frac{\partial^2 E_2}{\partial x_1 \partial x_2} + ik_3 \frac{\partial E_3}{\partial x_1}\right) = \frac{\omega^2}{c^2} E_1 \\ &\frac{1}{\varepsilon(\vec{x}_{II})}\left(\frac{\partial^2 E_1}{\partial x_1 \partial x_2} - \frac{\partial^2 E_2}{\partial x_1^2} + k_3^2 E_2 + ik_3 \frac{\partial E_3}{\partial x_2}\right) = \frac{\omega^2}{c^2} E_2 \quad , \\ &\frac{1}{\varepsilon(\vec{x}_{II})}\left(ik_3 \frac{\partial E_1}{\partial x_1} + ik_3 \frac{\partial E_2}{\partial x_2} - \frac{\partial^2 E_3}{\partial x_1^2} - \frac{\partial^2 E_3}{\partial x_2^2}\right) = \frac{\omega^2}{c^2} E_3 \end{aligned} \tag{1.7}$$

where the components of electric field E_1, E_2, and E_3 depend only on the in-plane position vector $\vec{x}_{II}$ .To solve these equations we expand the periodic function $\varepsilon^{-1}(\vec{x}_{II})$ in a Fourier series according to

$$\frac{1}{\varepsilon(\vec{x}_{II})} = \sum_{\vec{G}''_{II}} \eta(\vec{G}''_{II}) \exp(i\vec{G}''_{II}\vec{x}_{II}) \, . \tag{1.8}$$

The components of the electric field and $E_\alpha(\vec{x}_{II}, \omega)$ can be rewritten in a form that satisfies the Bloch-Flouqet theorem, required by the two-dimensional periodicity of the system,

$$E_\alpha(\vec{x}_{II}) = \sum_{\vec{G}'_{II}} a_\alpha(\vec{G}'_{II})\exp[i(\vec{k}_{II} + \vec{G}'_{II})\cdot\vec{x}_{II}], \qquad \alpha = 1,2,3 \tag{1.9}$$

where $\vec{k}_{II} = \vec{x}_1 k_1 + \vec{x}_2 k_2$ is the projection of the wave-vector of the wave on to the x_1x_2 plane.

If we substitute the expansions (1.8) and (1.9) into equations (1.7), multiply both sides of each equation by $exp[-i(\vec{k}_{II} + \vec{G}_{II})]$ and take an integral $\int_{-\infty}^{+\infty} d^2x$ from both sides of each equation we obtain the following set of equations for the coefficients $\{a_\alpha(\vec{G}'_{II})\}$:

$$\begin{aligned}
&\sum_{G'_{II}} \eta(\vec{G}_{II} - \vec{G}'_{II})\{((k_2 + G'_2)^2 + k_3^2)\cdot a_1(\vec{G}'_{II}) - (k_1 + G'_1)(k_2 + G'_2)\cdot a_2(\vec{G}'_{II}) - \\
&- (k_1 + G'_1)k_3 \cdot a_3(\vec{G}'_{II})\} = \frac{\omega^2}{c^2} a_1(\vec{G}_{II}) \\
&\sum_{G'_{II}} \eta(\vec{G}_{II} - \vec{G}'_{II})\{-(k_1 + G'_1)(k_2 + G'_2)\cdot a_1(\vec{G}'_{II}) + [(k_1 + G'_1)^2 + k_3^2]\cdot a_2(\vec{G}'_{II}) - \\
&- (k_2 + G'_2)k_3 \cdot a_3(\vec{G}'_{II})\} = \frac{\omega^2}{c^2} a_2(\vec{G}_{II}) \\
&\sum_{G'_{II}} \eta(\vec{G}_{II} - \vec{G}'_{II})\{-(k_1 + G'_1)k_3 \cdot a_1(\vec{G}'_{II}) - (k_2 + G'_2)k_3 \cdot a_2(\vec{G}'_{II}) + \\
&+ ((k_2 + G'_2)^2 + (k_1 + G'_1)^2)\cdot a_3(\vec{G}'_{II})\} = \frac{\omega^2}{c^2} a_3(\vec{G}_{II})
\end{aligned} \tag{1.10}$$

It is important to note that the set of equations (1.10) represents a general problem for non-polarized waves which propagate in an arbitrary direction ($k_3 \neq 0$). If the propagation of a wave is restricted to the x_1x_2 plane then one can put $k_3=0$ and split the equations into two sets for TE and TM polarization. However, here we will proceed with the most general case since such simplifications can be applied at the final steps.

Equations (1.10) contain the Fourier coefficients $\eta(\vec{G}_{II} - \vec{G}'_{II})$ of the reciprocal dielectric function which can be calculated by applying a general formula

$$\eta(\vec{G}_{II}) = \frac{1}{a_c}\int_{a_c} d^2x_{II}\,\exp(-\vec{G}_{II}\vec{x}_{II})\frac{1}{\varepsilon(\vec{x}_{II})}, \tag{1.11}$$

where a_c is the area of the elementary cell of a 2D lattice. For cylindrical pores or rods with circular cross-section (radius R) the Fourier coefficients are given by [16]

$$\eta(\vec{G}_{II}) = \begin{cases} f\dfrac{1}{\varepsilon_a} + (1-f)\dfrac{1}{\varepsilon_b}, \text{ if } \vec{G}_{II} = 0; \\ \left(\dfrac{1}{\varepsilon_a} - \dfrac{1}{\varepsilon_b}\right) f \dfrac{2\mathrm{J}_1(G_{II}R)}{G_{II}R}, \text{ if } \vec{G}_{II} \neq 0. \end{cases}, \tag{1.11a}$$

where $J_1(x)$ is a Bessel function, and f is the filling fraction, i. e. the fraction of the total volume occupied by the cylindrical rods (or pores). For a triangular lattice $f = \frac{2\pi}{\sqrt{3}} \frac{R^2}{a^2}$, for a square lattice $f = \frac{\pi R^2}{a^2}$, a is the period of the 2D lattice.

If the pores or rods have a square cross-section then the Fourier coefficients for non-zero $\vec{G}_{II}$ are given by

$$\eta(\vec{G}_{II}) = 4\frac{1}{\varepsilon_a}\frac{\sin(G_1 a)}{G_1 a}\frac{\sin(G_2 a)}{G_2 a} + 4\cdot\left(\frac{1}{\varepsilon_a} - \frac{1}{\varepsilon_b}\right)\frac{\sin(G_1 R)}{G_1 R}\frac{\sin(G_2 R)}{G_2 R}. \tag{1.11b}$$

For the details of the calculations see [2, 16].

The model can be easily extended to three-component structures where a third component is introduced as a ring-shaped interlayer between the rod and the background materials (Fig. 1.14). This third material is characterized by a dielectric constant ε_i and thickness d. Since the symmetry of the lattice does not change with such modification, one can still use the equations (1.10) but the Fourier coefficients of the reciprocal dielectric function will be given by [48]

$$\eta(\vec{G}_{II}) = \begin{cases} \left(\dfrac{f_1}{\varepsilon_a} + \dfrac{f_2}{\varepsilon_b} + \dfrac{f_i}{\varepsilon_i}\right), \quad \vec{G}_{II} = 0 \\ \dfrac{2\cdot\left(\dfrac{1}{\varepsilon_a} - \dfrac{1}{\varepsilon_b}\right)\cdot f_1 J_1(G_{II}\cdot R)}{G_{II}\cdot R} + \dfrac{2\cdot\left(\dfrac{1}{\varepsilon_i} - \dfrac{1}{\varepsilon_b}\right)\cdot f_3 J_1(G_{II}\cdot(R+d))}{G_{II}\cdot(R+d)}, \quad \vec{G}_{II} \neq 0 \end{cases}, \tag{1.11c}$$

where, $f_1 = \frac{2\pi}{\sqrt{3}}\frac{R^2}{a^2}$, $f_i = \frac{2\pi}{\sqrt{3}}\frac{((R+d)^2 - R^2)}{a^2}$, $f_3 = \frac{2\pi}{\sqrt{3}}\frac{(R+d)^2}{a^2}$, $f_2 = 1 - f_3$.

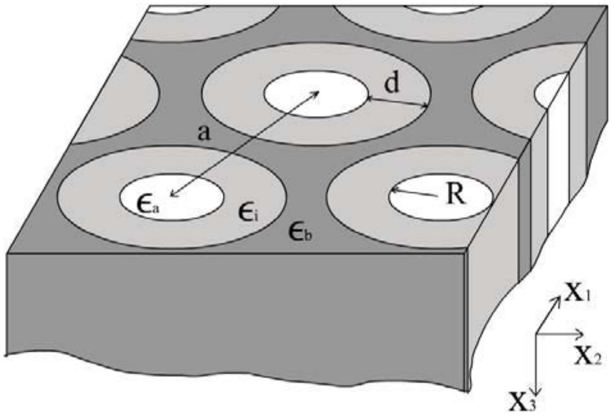

Fig. 1.14. A scheme of a three-component 2D PhC. The third component is introduced as a ring-shaped interlayer between the rod and background materials and is characterized by a dielectric constant ε_i and thickness *d*.

Such three-component model can be used, for instance, to include an oxide interlayer on the walls of the air pores in macroporous silicon 2D PhC [48].

1.2.2. Numerical scheme

Let us now consider the problem of numerical solving the system of equations (1.10). Generally speaking, the sum should be taken over infinite set of reciprocal lattice vectors. Obviously, we have to limit the number of the reciprocal lattice vectors to some finite value, lets call it *N*. This means that the system of 3*N* equations should be numerically solved. Due to the fact that $\lambda \equiv \omega^2/c^2$ appears only on the right side of the equations (1.10) we may represent the system as an eigenvalue problem:

$$\hat{M}\vec{A} = \lambda\vec{A}\ , \tag{1.12}$$

where the matrix *M* is given by

$$\begin{pmatrix}
\eta(\vec{G}^{(1)}{}_{II} - \vec{G}^{(1)'}{}_{II})\cdot[(k_2+G_2')^2+k_3^2] & \cdots & -\eta(\vec{G}_{II} - \vec{G}_{II}')\cdot(k_1+G_1')\cdot(k_2+G_2') & \cdots & -\eta(\vec{G}_{II} - \vec{G}_{II}')\cdot(k_1+G_1')\cdot k_3 & \cdots \\
\cdots & & \cdots & & \cdots & \\
-\eta(\vec{G}_{II} - \vec{G}_{II}')\cdot(k_1+G_1')\cdot(k_2+G_2') & \cdots & \eta(\vec{G}_{II} - \vec{G}_{II}')\cdot[(k_1+G_1')^2+k_3^2] & \cdots & -\eta(\vec{G}_{II} - \vec{G}_{II}')\cdot(k_2+G_2')\cdot k_3 & \cdots \\
\cdots & & \cdots & & \cdots & \\
-\eta(\vec{G}_{II} - \vec{G}_{II}')\cdot(k_1+G_1')\cdot k_3 & \cdots & \eta(\vec{G}_{II} - \vec{G}_{II}')\cdot(k_2+G_2')\cdot k_3 & \cdots & \eta(\vec{G}_{II} - \vec{G}_{II}')\cdot[(k_2+G_2')^2+(k_1+G_1')^2] & \cdots \\
\cdots & & \cdots & & \cdots &
\end{pmatrix}$$

(1.13)

In the horizontal direction the dots denote the additional *N-1* columns (for i = 2 … N), for each different $\vec{G}_{II}^{\prime(i)}$, in vertical direction the dots denote *N-1* rows corresponding to the rest of the different $\vec{G}_{II}^{(j)}$. So, if we use the basis of N reciprocal vectors then the $3N$ x $3N$ matrix needs to be solved.

Vector $\boldsymbol{A}$ in (1.12), the eigenvector of the matrix $\hat{M}$, has also $3N$ components and is given by

$$A = \begin{bmatrix} a_1^{(1)} \\ \dots \\ a_1^{(N)} \\ a_2^{(1)} \\ \dots \\ a_2^{(N)} \\ a_3^{(1)} \\ \dots \\ a_3^{(N)} \\ \end{bmatrix},$$

where a_1, a_2, a_3 are the Fourier coefficients of the field components E_1, E_2, E_3, correspondingly.

And finally λ_i, the eigenvalues of the matrix $\hat{M}$, have a form $\lambda_i = \frac{\omega_i^2}{c^2}$, $i=1,2... 3N$. Thus, by solving the eigenvalue problem (1.12) we can obtain the values of $\frac{\omega^2}{c^2}$ depending on the values of $\vec{k}$, or, in other words, the photonic band structure.

We have developed our own code realizing the PWEM using the MatLab programming language. The program code for triangular lattice three-component PhCs with short description of the variables is listed in Appendix I.

1.2.3. The range of validity and limitations of the PWEM.

It is important to remember that PWEM solves an *intrinsic* problem, namely it gives eigenfrequencies of eigenmodes of a structure which is infinite in all directions. Thus, such characteristics as transmittance and reflectance cannot be directly obtained from PWEM calculations. Experiments deal with finite structures, usually involving an external source and a far-field detector.

However, the PWEM appears to be very useful tool for the characterization of PhCs. For example, if a PhC has a high refractive index contrast then it is often enough to consider a structure with only 5-15 periods in the direction of the wave propagation: such a structure will already exhibit the properties (bands and gaps) of an "infinite" PhC. It is shown in this thesis (section 2.2) that the experimentally measured positions of the band gaps in a 1D PhC consisting of only 5 periods are in very good coincidence with the results of PWEM calculations. In the case of a PhC with a low refractive index contrast (see section 2.3) it is required to consider hundreds of periods in order to obtain an effectively "infinite" structure. Thus care must be taken when comparing the results of a PWEM calculation to real-space characteristics (such as transmittance and reflectance) of a finite PhC.

1.3. The Finite-Difference Time-Domain method (FDTD)

The FDTD method is a numerical method based on discretization of Maxwell's equations. Currently it is the one of the most widely-used simulation method in optics, photonics and microwave physics. The popularity of the FDTD is based on several advantages, namely:

1. FDTD is an explicit and intuitive method;
2. it allows to solve electromagnetic problems with complicated refractive index profiles;
3. it allows to include dispersive, absorbing and nonlinear materials;
4. since it is a time-domain method, nonequilibrium electrodynamics processes can be studied;
5. together with transmittance, reflectance and absorbance the amplitudes of electric and magnetic fields as well as Poynting vectors can be obtained for each point of the computational domain;
6. FDTD allows to visualize light-matter interaction processes in a natural and straightforward way;
7. FDTD is accurate and robust if the chosen discretization grid is fine enough.

The main limitation of the FDTD method is the high amount of computational resources needed for spatially large problems. However, rapid development of computers capability during last few decades makes the FDTD method suitable for broad spectrum of problems of electromagnetism.

1.3.1. The Yee algorithm

The basis of FDTD method was laid out in 1966 when Kane Yee proposed a finite-difference discretization scheme for the time-dependent Maxwell's equations [49]. The basic ideas proposed by Yee can be summarized as follows:

- the space is discretized into small cells having dimensions of $\Delta x*\Delta y*\Delta z$

- the time is discretized into the instants separated by time steps Δt

- the differential Maxwell's equations are discretized by replacing time and step derivatives of electric and magnetic fields by finite differences. The times for the electrical fields are interleaved between those of the magnetic fields.

- the components of both electric and magnetic field are calculated at each time step for all space grid points

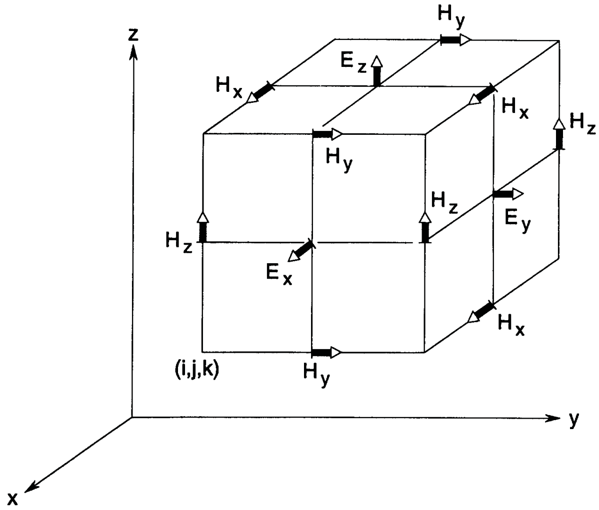

Fig. 1.15. Positions of electric and magnetic field components in a unit cell of Yee spatial grid. Taken from [50].

The positions of electric and magnetic field components in a unit cell of 3D discretization grid for a given time instant are shown in Fig. 1.15. Actually, Fig. 1.15 provides a direct visualization of the Maxwell's equations showing that 3D space is filled with arrays of Faraday's Law and Ampere's Law contours.

The Maxwell's curl equations in rectangular coordinate system can be rewritten in component form (SI units) [50]:

$$\begin{aligned}
-\frac{\partial B_x}{\partial t} &= \frac{\partial E_z}{\partial y} - \frac{\partial E_y}{\partial z} \\
-\frac{\partial B_y}{\partial t} &= \frac{\partial E_x}{\partial z} - \frac{\partial E_z}{\partial x} \\
\frac{\partial B_z}{\partial t} &= \frac{\partial E_x}{\partial y} - \frac{\partial E_y}{\partial x} \\
\frac{\partial D_x}{\partial t} &= \frac{\partial H_z}{\partial y} - \frac{\partial H_y}{\partial z} - J_x \\
\frac{\partial D_y}{\partial t} &= \frac{\partial H_x}{\partial z} - \frac{\partial H_z}{\partial x} - J_y \\
\frac{\partial D_z}{\partial t} &= \frac{\partial H_x}{\partial y} - \frac{\partial H_y}{\partial x} - J_z
\end{aligned} . \tag{1.14}$$

We denote a space grid point at $(i\Delta x, j\Delta y, k\Delta z)$ by the triple (i,j,k) and any discrete function of space and time $f(i\Delta x, j\Delta y, k\Delta z, n\Delta t)$ as $f^n(i,j,k)$, where n is the number of time steps elapsed.

In the Yee scheme the space and time derivatives are replaced by centered finite-differences. For instance, a partial space derivative of the function *f* in x-direction at a time moment *t= nΔt* is given by

$$\frac{\partial[f^n(i,j,k)]}{\partial x}=\frac{f^n(i+1/2,j,k)-f^n(i-1/2,j,k)}{\Delta x}. \tag{1.15}$$

The time derivatives are treated in a similar way. The partial time derivative of the function *f* at a space point *(i,j,k)* can be calculated by

$$\frac{\partial[f^n(i,j,k)]}{\partial t}=\frac{f^{n+1/2}(i,j,k)-f^{n-1/2}(i,j,k)}{\Delta t}. \tag{1.16}$$

By substituting (1.15) and (1.16) into (1.14) one can obtain the unknown values of the electric and magnetic field components in a given space point at a time step $t_{n+1/2}$ from the known values at previous time step in the same space point and from the known values at previous time step in adjacent space points. The detailed derivation of the discrete finite-difference equations as well as many other aspects of FDTD method can be found in the book of Allen Taflove [50].

1.3.2. Numerical stability

The FDTD method allows, in principle, to consider structures with any refractive index profile. In practice, however, consideration of spatially large problems encounters some difficulties. The limiting factor is the number of spatial grid points which should be included in a model which is restricted by the physical memory of a computer. The grid should be fine enough to resolve the finest features of a studied structure, besides, the variation of the fields' amplitudes between two adjacent grid points must be small. The latter fact means that the size of a grid cell should be much smaller than the wavelength. Usually it is assumed that the size of grid cell in one dimension must be at least 10 times smaller than the wavelength [50]:

$$\Delta x,\Delta y,\Delta z<\frac{\lambda}{10} \qquad (1.17).$$

However, even if the condition (1.17) is fulfilled, the results of such simulations will be only approximate. A convergence study should be performed for each model in order to prove that decreasing the grid cell size does not influence the results of simulation significantly.

Another, more fundamental, constraint called numerical stability condition or Courant condition is given by the following expression:

$$\Delta t \le \Delta t_{\max} = \frac{1}{c\sqrt{\frac{1}{(\Delta x)^2}+\frac{1}{(\Delta y)^2}+\frac{1}{(\Delta z)^2}}}, \tag{1.18}$$

where Δt is a time step, c is the velocity of the wave propagation, and Δx, Δy, Δz are the spacings of the spatial grid. Condition (1.18) defines the maximal time step for given choice of the spatial grid. It is shown in [50] that violation of the condition (1.18) can results in unphysical exponential growth of the electric and magnetic field amplitudes during the simulation.

Generally, care must be always taken during interpretation of the FDTD simulation results.

1.3.3. Boundary conditions

The difficulty of considering spatially large problems within the FDTD method can be partially overcame by putting appropriate for a given model boundary conditions. For instance, when considering a periodic structure (e.g. a photonic crystal) then it is enough to include in a model a single unit cell and put periodic boundary conditions in the directions of periodicity. Absorbing boundary conditions (ABC) are used when one needs to simulate waves escaping to infinity. Transmitted, reflected or scattered EM wave which encounters a boundary of the computational domain should be perfectly absorbed (zero reflection) if the ABC are applied. One of the most widely-used ABC in the FDTD method is so-called perfectly matched layer (PML). The PML acts as a virtual absorbing material surrounding the computational domain. This is analogous to simulation of the walls of an anechoic chamber.

The choice of boundary conditions is dictated by the objectives of a given problem. Periodic boundary conditions are usually used to decrease the dimensions of computational domain in order to save the time and physical memory. However, if one needs to record transmitted or reflected EM power than PML ABC should be used. It is also possible to combine periodic boundary conditions and PML ABC within one model by applying them to different boundaries of the computational domain. Some examples of simple FDTD calculations involving different boundary conditions are given in the next subsection.

1.3.4. Overview of the FullWAVE™ computer package

In this thesis a commercial package RSoft FullWAVE™ realizing the FDTD method is used [51]. In this subsection we review the main features of this package on the example of simple problems of optics.

Let us consider a problem of scattering of light by a dielectric sphere in two dimensions (Fig. 1.16a). The horizontal orange bar in the bottom is a plane wave source, the red circle is a dielectric sphere (in 2D – a circle). Two horizontal green bars are so-called "time monitors" – the numerical analogies of detectors – recording the EM power flux through themselves. A purple rectangle marks the boundary of the computational domain. In the current case the PML ABC are applied to all four edges of the domain. The refractive index of the background is 1, the dielectric sphere has a refractive index of 3.5. The diameter of the sphere is 5 µm. In Fig. 1.16b the distribution of electric field component E_y after time t=0.67 fs (ct=200 µm, where c is the speed of light in vacuum) is shown. The wavelength of the continuous plane wave is 1 µm. In Fig. 1.16c the transmittance and reflectance recorded by the top and the bottom time monitor, respectively, is shown. Both transmittance and reflectance are normalized to the total power radiated by the source. It is important to note that although absorption is not included in the model the sum of transmittance and reflectance do not give 1 since the scattered power impinged on the left and right boundaries and absorbed by the PML is not recorded by the monitors.

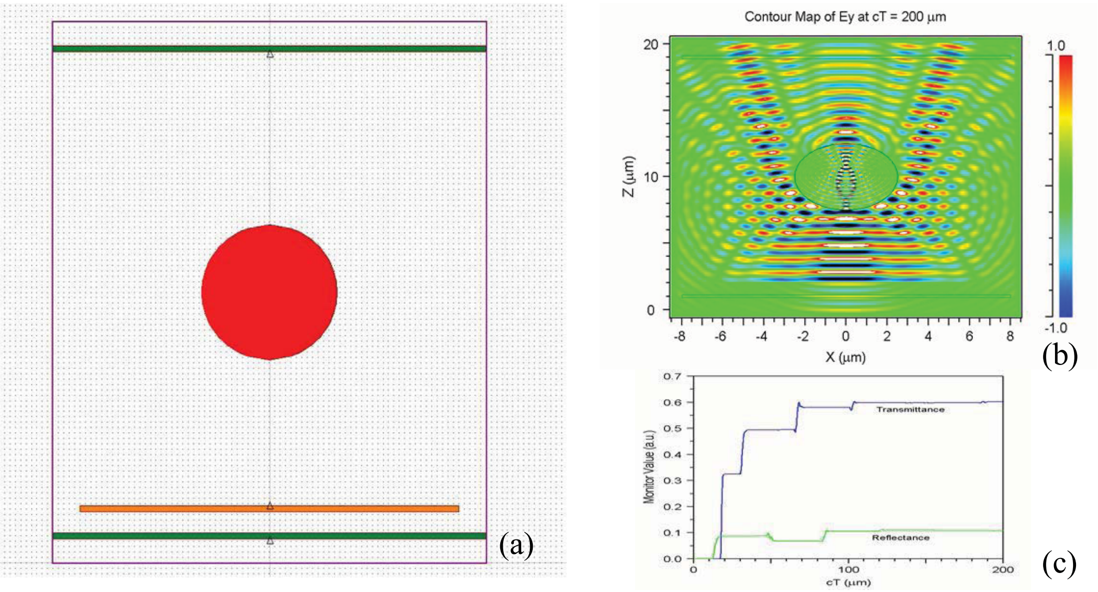

Fig. 1.16. Interaction of light with a dielectric sphere in two dimensions. (a): geometry of the problem, for detailed description see text. (b): the distribution of E_y component. (c): transmittance and reflectance recorded by the top and bottom time monitor, respectively. The time is multiplied by the vacuum speed of light and thus given in units of µm.

Let us now consider a plane-parallel dielectric plate as shown in Fig. 1.17a. Now, due to infinitesimal translation invariance of the system in horizontal direction, it is convenient to apply periodic boundary conditions to the left and right boundaries of the computational domain. The top and the bottom boundaries have PML ABC. Such a model represents an infinitely long (in the horizontal direction) plane-parallel plate. The thickness and the refractive index of the plate are 1 µm and 3.5, respectively; the background has a refractive index of 1. The wavelength of the plane wave source is chosen to be 3.5 µm. That corresponds to the second eigenmode of the plane-parallel plate according to the well-known formula for interference in thin films (normal incidence case):

$$\lambda m = 2dn, \tag{1.19}$$

where d is the thickness of the film (d=1 μm), n is the refractive index of the film (n=3.5) and m is the number of the eigenmode (m=2). Formula (1.19) is the condition for destructive interference between the reflected waves from the two sides of the plate.

The distribution of E_y field component and the time-dependent transmittance and reflectance are shown in Figs. 1.17b and 1.17c, respectively. Since the wavelength of the incident wave exactly fits the destructive interference condition for reflected waves (1.19) the plane-parallel plate exhibits almost 100% transmittance.

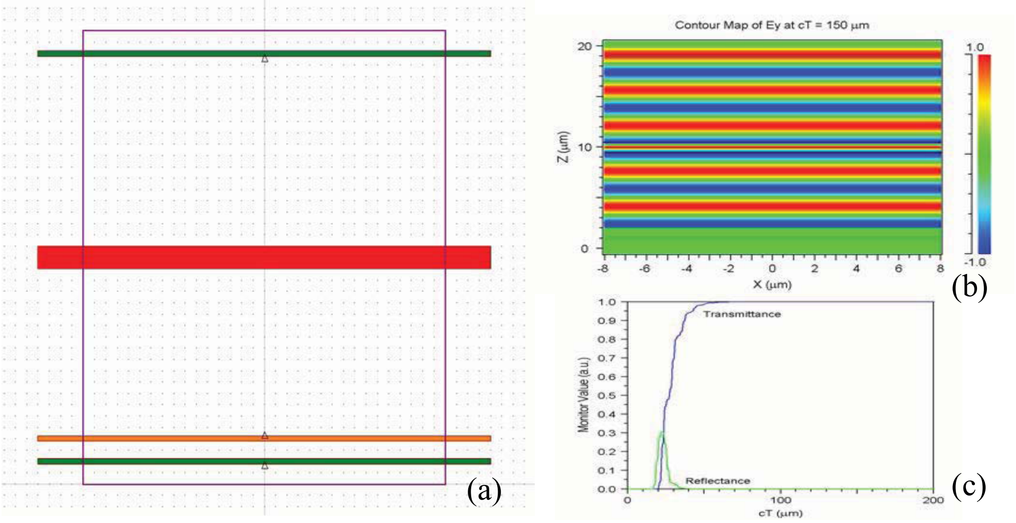

Fig. 1.17. A problem of interaction of light with a dielectric plane-parallel plate in two dimensions. (a): geometry of the problem, for detailed description see text. (b): the distribution of E_y component. (c): transmittance and reflectance recorded by the top and bottom time monitor, respectively.

It is also possible to perform frequency analysis in the frameworks of the FDTD scheme. This is realized in FullWAVE™ package by applying a fast Fourier transform (FFT) to the time response of a system recorded by a time monitor. In this case the system is excited by an impulse containing different frequencies in some, defined by the user, range. As an example, transmission and reflection spectra for a dielectric plane-parallel plate (the same as in Fig. 1.17a) are shown in Fig. 1.18. The blue and the green curves are the transmittance and reflectance, respectively. The red curve shows the frequency spectrum of the excitation pulse. The arrow indicates the frequency corresponding to the wavelength of 3.5 μm ($f/c=0.286$ μm^{-1}) which was used for the simulation shown in Fig. 1.17b. Figure 1.18 demonstrates typical Fabry-Perot oscillations where the spectral positions of the transmission maxima can be calculated by the formula (1.19). It is important to note, that due to the periodic boundary conditions all electromagnetic power irradiated in the system is now detected by either upper or lower (Fig. 1.17a) monitor, thus the transmittance and reflectance add up to unity.

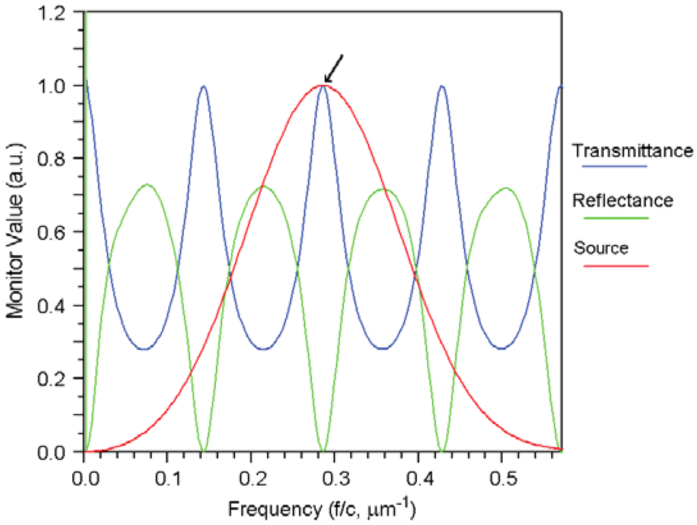

Fig. 1.18. Transmission (blue) and reflection (green) spectra for the same system as in Fig. 1.17a obtained by FFT analysis of the time response of the system. The red curve is the spectral width of the source. The arrow shows the frequency which was used in the simulation shown in Fig. 1.17b.

The FFT analysis allows to obtain the spectral characteristics of a system in a single FDTD simulation. Unfortunately, the use of FFT in three dimensions requires a huge amount of physical memory (tens of gigabytes). This limits the applicability of the FDTD method for frequency domain calculations.

Generally speaking, the RSoft FullWAVE™ package requires the following input information:

- the size of the computational grid cell;
- the size of the computational domain;
- the boundary conditions for the computational domain.;
- the refractive index profile;
- the size and the position of the source;
- the type of the excitation (constant wave, pulse);
- the profile of the excitation (Gaussian, rectangular, etc.);
- the sizes and the positions of the monitors.

The output information which can be obtained by RSoft FullWAVE™ includes:

- the time-dependent flux of electromagnetic power through a time monitor normalized to the power irradiated by the source;
- the strengths of electric and magnetic field components at any point of the computational domain at particular time instants;
- the amplitudes of electric and magnetic fields at any point of the computational domain;
- the frequency-dependent flux of electromagnetic power through a time monitor normalized to the power irradiated by the source.

Chapter 2. Investigations of surface roughness and disorder in photonic crystals

2.1. Disorder in photonic crystals (Review)

The purpose of this review is to order and to summarize the information concerning influence of disorder on photonic crystals properties. The major part of this review is devoted to the influence of disorder on photonic band gap width and position (first three subsections). Another part (subsection 2.1.4) deals with disorder in photonic crystal cavities and waveguides. A few papers touching negative refraction and superlens effect in 2D photonic crystals are also reviewed.

2.1.1. One-dimensional photonic crystals

An experimental investigation of surface roughness in 1D PhCs with a defect layer was done in [52]. 1D periodic structures consisting of alternating Si and SiO_2 layers with thickness d_{Si}=0.27 µm and d_{SiO_2}=0.9 µm were fabricated. A total of 10 layers were deposited on each sample. A central layer was the defect one with different thickness. AFM and STM measurements showed that the typical sizes of the surface roughness features were in the range 5-15 nm. The numerical calculations were performed utilizing effective the medium approach and the transfer matrix method (TMM). Figure 2.1 shows transmittance measurements (black curves) and calculations (blue dashed curve). The dotted curve is the calculated transmittance of the structure without roughness.

It was proposed to characterize the impact of disorder by means of three parameters: change in transmission amplitude of defect peak, change in transmission amplitude of the band gap edges and spectral shift of the defect peak position.

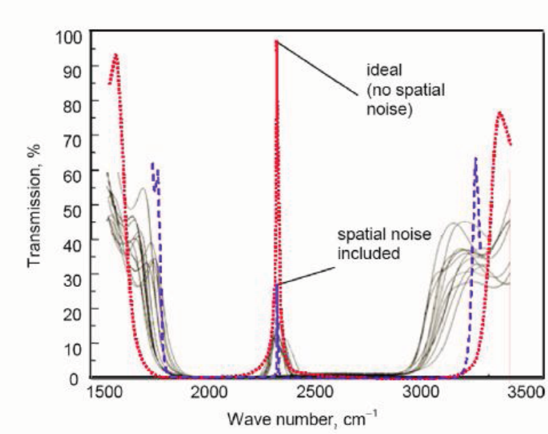

Fig. 2.1. Transmission spectra of a Si/SiO$_2$ 1D PhC with a defect layer. Solid: measured, different curves were taken at different spot positions; dotted: no roughness, calculated by TMM; dashed: roughness included, calculated by TMM. Taken from [52].

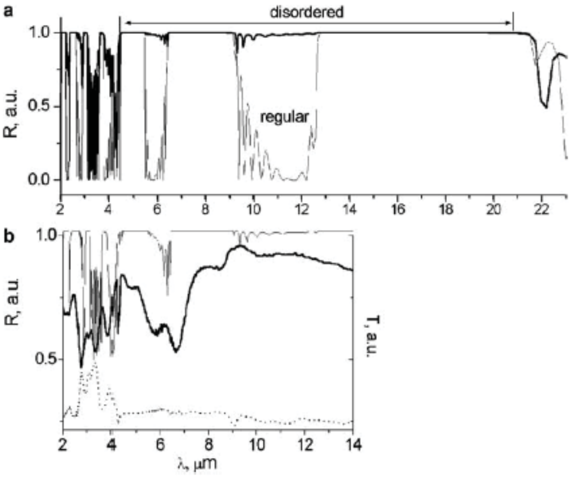

Fig. 2.2. (a) The calculated reflection spectra for the regular PhC (thin line) and a PhC with three defect layers (thick line). (b) The experimental (thick line) and fitting to the experiments (thin line) reflection spectra for disordered photonic crystal. Experimental transmission spectrum for the same sample is shown by the dotted line. Taken from [53].

The TMM calculations showed roughness-induced narrowing of the band gap and decreasing of both defect peak and band gap edges transmission amplitudes. The experiment confirmed the effects well with the exception of the shift of the high-frequency band gap edge being larger than predicted by theory. Quantitatively, the drop in transmission at the defect peak maximum was about 60 %, the drop in transmission at the band gap edges was about 20%, and the spectral narrowing of the band gap constituted about 40% with respect to the calculations made for ideal structure.

The reflectance spectra of a silicon/air one-dimensional photonic crystal with disorder in thickness were measured in [53]. A disorder was introduced by changing the thicknesses of three of 11 silicon layers. The thickness of regular silicon layers was 1.7 μm while the defect layers were 1, 1.1, and 1.4 μm thick. Both numerical calculations and experimental measurements of reflectance spectra for normal incidence were carried out. According to the TMM calculations, the authors claim that a number of band gaps related to the periodic (perfect) structure are joined together and form a new, wider band gap ranging from 4.5 to 20.5 μm. (Fig. 2.2a) Experimental measurements, however, show lower reflectance in the mentioned range (Fig. 2.2b). It is necessary to point out that both the measurement and the simulation were made only for one structure without averaging of the results. Besides, all the reflectance spectra are given in arbitrary units that make it impossible to obtain information about the absolute reflectance of the samples. Therefore, we believe that the statement about joining several band gaps due to insertion of three defect layers requires additional evidence.

In the theoretical work [54] authors also reported on band gap extension with increasing of disorder. Their TMM calculations showed that the transmission bands between the band gaps could be turned in a high reflection range (R>95 %). Dielectric constants were ε_1=10.24 and ε_2=1.32 and the structure had 24 periods. The disorder in this paper was defined as:

$$D = \frac{\sqrt{\sum_{i=1}^{m}\left(n_h^2(H(i)-H_0)^2 + n_1^2(L(i)-L_0)^2\right)}}{(n_h H_0 + n_1 L_0)m}, \tag{2.1}$$

where L_0, H_0 are non-perturbed thicknesses of the low- and high-index layers, respectively; $H(i)$, $L(i)$ are the real thicknesses of each layer; m is the number of the layers; n_h, n_l are the refractive indices. For simplicity the thickness of low index strata was kept constant ($L(i)= L_0$) while the thicknesses of the high index layers were randomly chosen from a Gaussian distribution around H_0. For disorder higher than 5 % three separate high-reflection regions corresponding to Bragg reflection maxima became coupled to one extended high reflection region (Fig. 2.3.). Thus, the main result of [54] is that the high-reflection region can be extended by introducing disorder to the thickness of the layers in a 1D photonic crystal.

A considerable statistical numerical analysis of disorder in 1D photonic crystals was carried out in [55, 56]. It was proposed to describe both disorder in thickness and disorder in refractive index in terms of disorder in optical length:

$$D_i = D(n_A + n_B)/2 = Dn_0(1+\delta P) = D_0(1+\delta P), \tag{2.2}$$

where D_i is the optical length of a unit cell; D is the period of the photonic lattice; P is a random value in the range (-1/2;1/2); δ is a constant specifying the amplitude of disorder. The refractive index of the structures was described by the formula $n_{A,B} = n_0 \pm g + n_0\delta P$, while layer thicknesses were given by $d_{A,B} = d + d\delta P$. Characteristic values used in the calculations were: n_0=2, g=0.025, 0.05, 0.1. The thickness of the structure was L=200D. The authors supposed that if disorders in refractive index and in thickness are described by the same optical lengths then they also have identical influence on transmission.

TMM calculations of density of states and transmission spectra showed substantial reduction of the band gap: transmission inside the gap increases and the width of the band

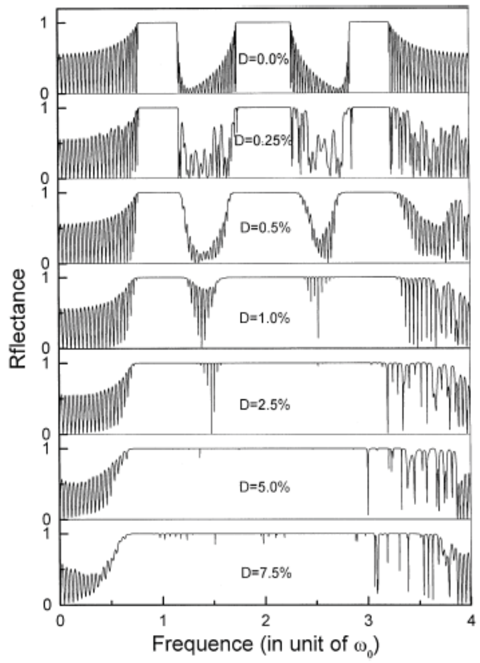

Fig. 2.3. Reflectance spectra at normal incidence for disordered 1D binary photonic crystals. *D* is the disorder parameter calculated by (2.1). ω_0 corresponds to λ_0=1.15 μm. Taken from [54].

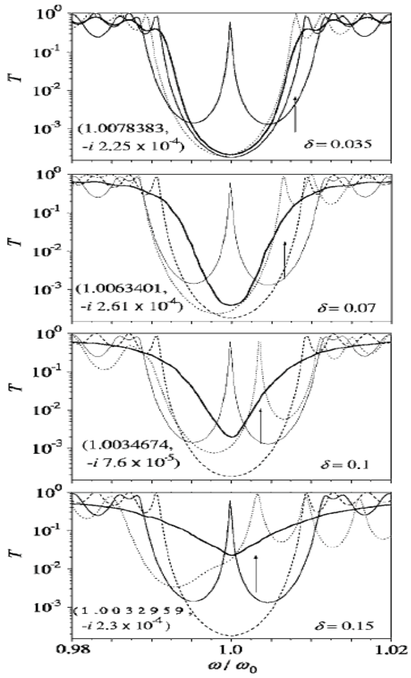

Fig. 2.4. Transmission spectra for a single PhC structure (dotted lines), and averaged over an ensemble of structures (thick solid lines). Dashed lines show the spectra for an ideal structure, and the thin solid lines shows the spectra for a microcavity with a half-wavelength core based on an ideal structure. Taken from [55].

gap decreases (Fig. 2.4). However, this result is related to an ensemble averaged over 10^3 disordered structures while individual transmission spectra demonstrate spiky appearance of narrow high- transmission regions within the band gap. Furthermore, the authors have shown that the higher the contrast in refractive index the higher is the amount of disorder required to close a band gap.

Further statistical analysis has shown that the dependence of transmission coefficient in the center of the band gap on disorder exhibits threshold-like behavior. When the disorder is smaller than some critical value δ_{th} (which is individual for each configuration) the transmission coefficient averaged over a large ensemble (10^6 structures) grows insignificantly with increasing disorder. For the $\delta>\delta_{th}$ the transmission in the center of band gap grows fast. For all cases the position of a threshold was well described by the formula: $\delta_{th} \approx \sqrt{(\Delta\omega/\omega_0)/3}$, where $\Delta\omega/\omega_0$ is the relative width of the band gap.

Calculations of band structure, density-of-states, transmission, and defect states in 1D photonic crystals utilizing supercell plane-wave expansion method (PWEM) and transfer matrix method were carried out in [57]. Disorder in thickness was introduced in highly contrast ($\varepsilon_a/\varepsilon_b$ = 13/1) quarter-wave periodical structure. The supercell PWEM showed vanishing of the first (lowest), second and third band gaps at disorder 0.55*d*, 0.18*d*, and 0.1*d*, respectively (*d* is the lattice constant). Transmission spectra, averaged over an ensemble of 100 random structures, demonstrate a smearing of the band gap edges with increasing of disorder. At the same time, transmission outside the band gaps decreases.

Thus, the reviewed papers could be divided in two groups: in the first one the papers are showing band gaps extension with increasing of disorder while in the second one authors claim that band gaps are reduced with increasing of disorder. It is necessary to note that all papers deal with normal incidence of light and all papers with the exception of [55] examined high-contrast structures. An evident distinction between these two groups of papers is that calculation and measurements of *reflection* showed band gap extension while *transmission* measurements show band gap narrowing. But anyway almost perfect reflection and average transmission at the same time is impossible. Thus, even for the simplest periodic structures – 1D photonic crystal – the problem of disorder influence on photonic band gaps is still actual.

2.1.2. Two-dimensional photonic crystals

A comprehensive theoretical analysis of transmission and reflection spectra for radial disorder [58] and positional disorder [59] was carried out for 2D triangular lattice "hole" photonic crystals (n_{air}=1, n_b=3.6, r=0.4a). In these papers an approach of distinguishing "straight" (or ballistic) transmitted light from scattered transmitted light is applied. It was shown that both size and positional disorder induce the increase of transmission within the band gap. Moreover, the intensity of the scattered light shows a strong dependence on disorder beginning from small values of δ~0.02 (relative to the lattice constant a), while ballistic transmission behaves in threshhold-like manner being insensitive to small disorder and starts to grow for δ>0.1. The resulting spectra were averaged over 10 configurations in [58] and over 20 configurations in [59] (Fig. 2.5). It is necessary to note, however, that in these papers an incomplete (only for ΓK direction) photonic band gap was examined.

The thin lines on the spectra show the individual (non-averaged) transmission/reflection. It is clearly seen that for high amounts of disorder the band gap and transmission bands become indistinguishable parts of a spiky spectrum with moderate transmission and reflection.

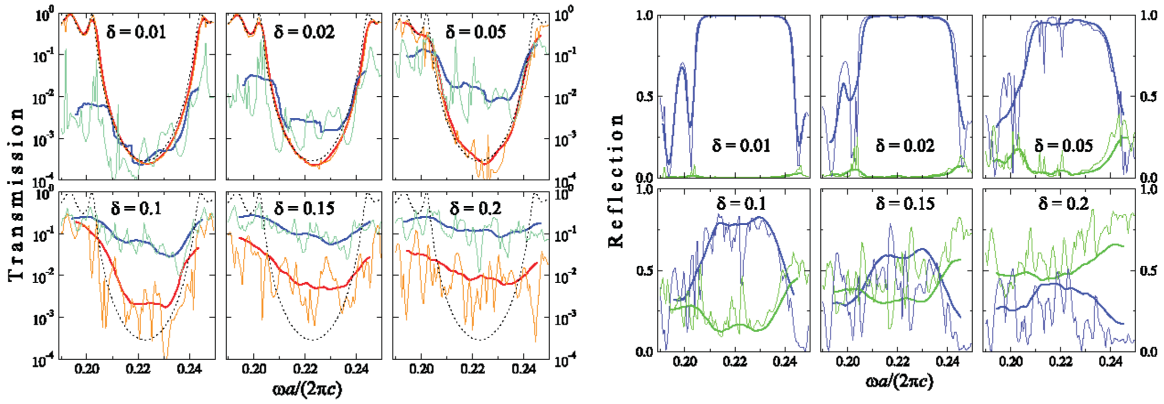

Fig. 2.5. (Left) Calculated transmission spectra for photonic crystal with positional disorder for different values of the disorder parameter: δ= 0.01, 0.02, 0.05, 0.1, 0.15, and 0.2. Red lines are the ballistic transmission, blue lines are the scattered transmission – the thin lines for an individual configuration of disorder, and the heavy lines for the mean averaged over 10 random configurations of disorder. The ballistic transmission spectrum of the ideal photonic crystal is also shown (black dotted line) for comparison. (Right) Calculated reflection spectra for the same structures. Indigo lines are the ballistic reflection and green lined are the scattered reflection. Taken from [59].

Sigalas et. al. [60] considered three types of disorder: size, radius and dielectric constant in a 2D square lattice "rod" photonic crystal. The dielectric constant and filling ratio of rods were ε=10 and f=0.29, respectively. The band gap narrowing with increasing disorder is clearly manifested on transmission spectra and DOS plots. The high-frequency gaps are more sensitive to disorder and vanish first. In addition, the calculation showed that the wider the gap of the periodic case, the larger is the amount of disorder needed to close it.

Lidorikis et. al. [61] considered disorder in both "hole" and "rod"-type 2D photonic crystals organized in square lattice ($\varepsilon_a/\varepsilon_b$=1:10). The FDTD method (DOS calculations) and the TMM (transmission calculations) were applied. Disorders in position, radii and dielectric constant were examined, and overlapping of the rods was allowed in several cases. For all types of disorder band gap reduction was clearly observed in spectral dependencies of transmission and DOS. However, in the case of "rod" type structure, the photonic band gaps for the E_z polarization (z-direction is parallel to the rod axes) survive very large amounts of positional disorder while the H_z band gaps vanish quickly. Averaging over 20 disorder configurations was used.

A model of "nearly-free" and "strongly localized" photon states was suggested in order to explain the response of optical properties of photonic crystal to disorder in [61]. In the "strongly localized" case the gap-forming mechanism is the short-range excitation of single-scattering Mie resonances. Thus, a long-range periodicity is not strictly necessary for existence of a band gap and positional disorder has no strong effect. This mechanism can explain why the E_z photonic band gap in the solid cylinder case, where sharp Mie resonances appear, sustains a high amount of positional disorder. In the "nearly-free" model the decisive gap-formation mechanism is Bragg-like reflection due to multiple scattering. Spatial periodicity is very important in this case since the incoherence of scattered waves will destroy strong interference effects and band gaps will smear out.

Asatryan et. al. investigated refractive index disorder [62], as well as positional and radius disorders [63] in a square lattice 2D photonic crystals consisting of 20 rows of cylinders with n_c=3.0 and f_c=0.283 surrounded by air. Transmission spectra were averaged over up to 100 different disorder realizations in each case. Disorder in refractive index was introduced by the formula [62]: $n_l = \bar{n} + \delta$, were δ takes random values in the range (-Q;Q). Transmission spectra for Q={0, 0.2, 0.4, 0.8} are presented on Figs. 2.6 and 2.7 for E_z and H_z polarizations, respectively. It is necessary to point out that the relative increase of the minimal transmission in the lowest band gap in the E_z polarization case (~1.5 times) is smaller than for the H_z polarization (~5 times) with increasing disorder.

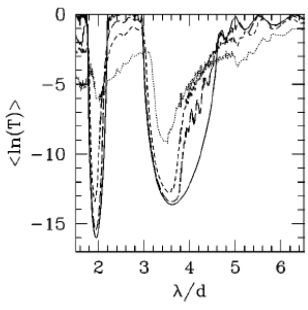

Fig. 2.6. Plot of $\langle \ln T \rangle$ vs wavelength for E_z polarization for Q=0 (solid), Q=0.2 (dashed), Q=0.8 (short dashed). Taken from [62].

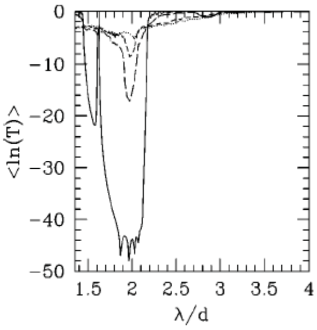

Fig. 2.7. Similar to Fig. 2.6. but for H_z polarization. Here Q=0 (solid), 0.2 (dashed), 0.6 (dotted), and 0.8 (dot-dashed). Taken from [62].

Radial disorder in [63] was defined with respect to the lattice constant d. Transmission spectra are given for Q=0.01d (~0.033 of radius) and Q=0.08d (~0.26 of radius). As in previous case, the lowest gap for E_z polarizations sustains much higher disorder than the one for H_z polarization (Figs. 2.8 and 2.9).

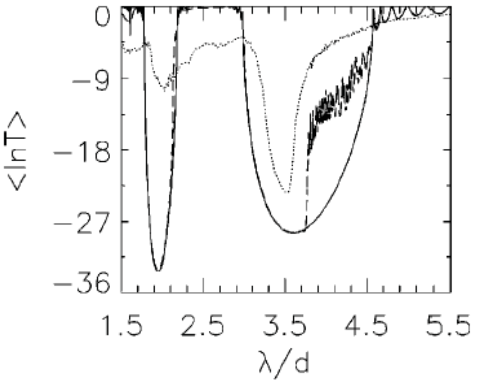

Fig. 2.8. Plot of $\langle \ln T \rangle$ vs wavelength for E_z polarization for Q_r=0 (solid), Q_r=0.01d (dashed), and Q_r=0.08d (dotted). Taken from [63].

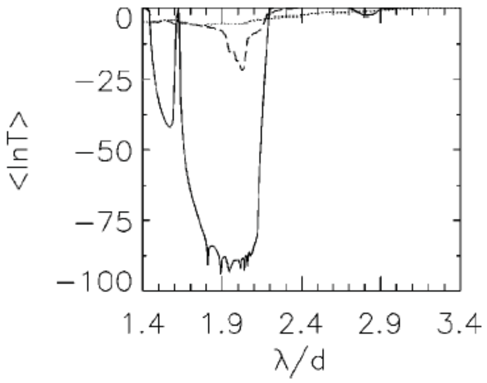

Fig. 2.9. Same as Fig. 2.8. but for H_z polarization. Taken from [63].

In the case of positional disorder, the band gaps for E_z polarization are affected insignificantly even for high amount of disorder Q=0.15d (Fig. 2.10). The main effect is the appearance of "resonances" in the long-wavelength part of the lowest (right on the picture) band gap. In the case of H_z polarization even a small amount of positional disorder significantly increases the transmission within the band gap (Fig. 2.11).

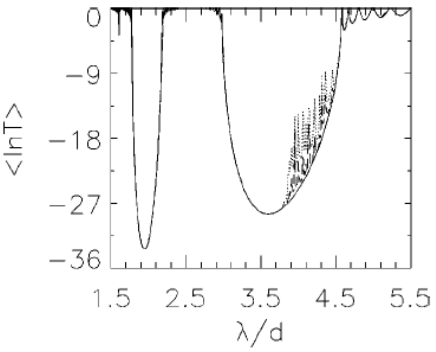

Fig. 2.10. Plot of $\langle \ln T \rangle$ vs wavelength for E_z polarization for Q_c=0 (solid), Q_c=0.05d (dashed), Q_c =0.15d (dotted). There are N_c=10 cylinders per unit cell and N_L=20 layers in the stack. Taken from [63].

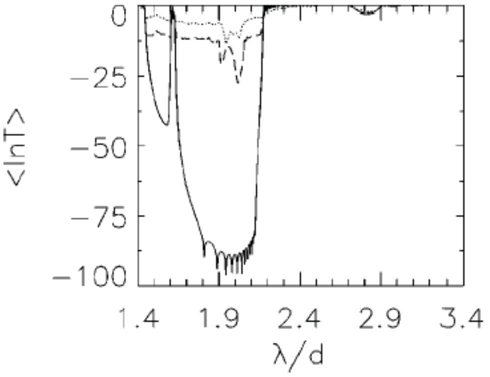

Fig. 2.11. The same as in Fig. 2.10, but for H_z polarization. Taken from [63].

Thus, for all three types of disorder in 2D photonic crystals consisting of high-index rods organized in a square lattice in air, the transmission of H_z polarized EM waves is essentially sensitive to any type of disorder, while E_z polarized waves demonstrate high stability of photonic band gaps, especially in the case of positional disorder.

Disorder in radius was examined for both "rod" and "hole" type 2D photonic crystals in [64] by the supercell PWEM. The contrast of the dielectric constants was 12:1; r=0.2a for the "rod" PhC and the r=0.4a in "hole" PhC. Only DOS calculations were performed utilizing 9x9 supercell. The authors reported a moderate reducing of the band gap width with increasing disorder up to δ=0.15r in all three investigated cases: TM(E_z) square lattice "rod"; TM triangular lattice "rod"; TE triangular lattice "hole". Band gap width reduction in all cases was due to the appearance of spike-shaped "localized" areas of non-zero DOS.

Li et. al. [65] considered radial and positional disorder in square and triangular lattice "rod" photonic crystals with dielectric constants contrast 13:1 and r=0.309a. DOS calculation by the supercell PWEM showed that only disorder in radius (up to δ=0.33r) has considerable effect on the band gap. Positional disorder up to δ_{xy}=0.45r does not impact band gap significantly. 5x5 and 7x7 supercells were used for positional and size disorder, respectively.

R. Meisels and F. Kuchar [66] gave a detailed analysis of disorder in two types of structures: square lattice "rod" photonic crystals with ε=13, r=0.329a and triangular lattice "hole" structures with ε=13, r=0.4a. DOS and field distributions were calculated by supercell PWEM. The lowest band gap of the "rod" type PhC demonstrated high stability:

only the high-frequency edge of the gap was shifted to lower frequencies with increasing of disorder up to $0.1a$. However, the same amount of disorder introduces numerous "localized" states inside the second gap. The triangular lattice is more sensitive to disorder as indicated by stronger narrowing of the band gap. The field distribution patterns calculated for highly disordered structures showed that the gap states are localized within few lattice constants in the supercell. FDTD propagation simulations showed increasing of scattering and destroying of beam-like propagation with increasing disorder. This effect is stronger for higher frequencies.

W. R. Frei and H. T. Johnson [67] found that in some cases of positional disorder in square lattice "rod" PhC (ε_c=11.4), the transmission within band gap can decrease with increasing of disorder. Actually, this effect was clearly observed only for the lowest E_z band gap and positional disorder. Disorder in radius in most cases increased the transmission. The effect was explained by a "point defect model" which represents disorder as a set of point defects. Each point defect increases the lateral and back-scattering of EM waves that may lead to a decrease of the overall transmission. The authors have not provided quantitative characterization of "apparent increase of the band gap strength" but it appears from the plots that the effect is very small and most likely experimentally undetectable.

Experimental investigations of disordered 2D photonic crystals were carried out by Bayindir et. al. [68]. Dielectric photonic crystals were made of cylindrical alumina rods with r=1.55 mm and n=3.1 and organized in a square lattice with lattice constant a=1.1 cm. Transmission spectra were measured for two cases of positional disorder (δ_{xy}=0.11r and δ_{xy}=0.25r) and each curve was averaged over 5 different random configurations (Fig. 2.12). Two main effects were observed with increasing disorder: the band gap became narrower and upper band gap edge decreased nearly by 15 dB. In spite of narrowing, the gap is still obvious even for δ_{xy}=0.25. Metallic photonic crystals were constructed from cylindrical copper rods with radius 1.55 mm and lattice constant a=1.1 cm. In addition to photonic band gaps, appearing due to a refractive index modulation, metallic photonic crystals also have a “metallicity gap” extending from 0 GHz to the plasma frequency (11.67 GHz in Fig. 2.13). The photonic band gap in metallic structure is strongly affected by disorder and vanishes quickly while the metallicity gap remains almost unchanged.

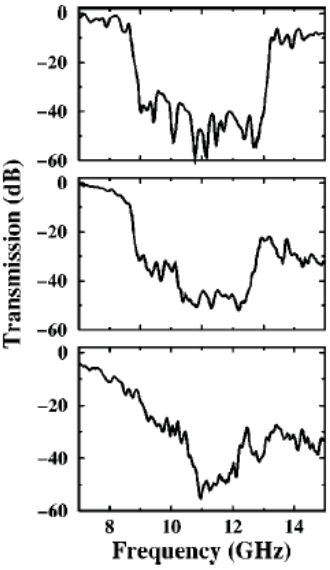

Fig. 2.12. The measured transmission spectra for (top) periodic (δ_r=0), and for disordered dielectric photonic crystals with (middle) δ_r=0.11r and (bottom) δ_r=0.25r. The photonic band gap shrank as the amount of disorder was increased. Taken from [68].

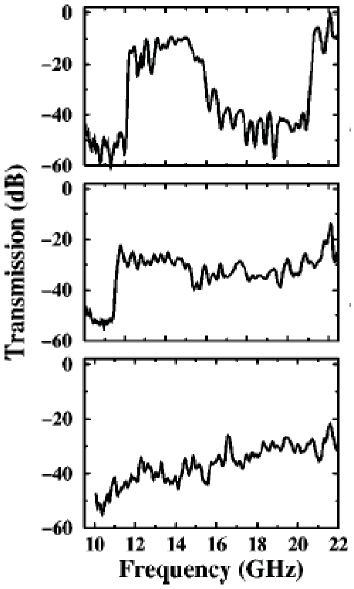

Fig. 2.13. . The measured transmission spectra for (top) periodic (r=0), and for disordered metallic photonic crystals with (middle) δ_r=0.11r and (bottom) δ_r=0.25r. As the amount of disorder increased the plasma frequency is shifted to lower frequencies and the photonic band gap closed quickly. Taken from [68].

Transmission experiments for a 2D array of Teflon cylinders were carried out by Li et. al. [69]. Square and rectangular lattices were examined and the structures had the following parameters: R=40±20 μm; a=170±20 μm; ε=2.2. A PhC with such parameters exhibits only unidirectional band gaps. By comparison of calculations and measurements the two main conclusions were made: (1) transmission dips corresponding to stop bands become shallow or can be washed out and (2) the transmittance obviously decreases with the frequency.

We conclude that the main effect of disorder is progressive blurring and as a result total vanishing of photonic band gap with increasing of disorder. At the same time, the areas of high transmission located between the band gaps, also smear out so a spectrum becomes "spiky" and formerly allowed and forbidden bands become undistinguishable. This general conclusion is confirmed mostly for square lattices of high-index circular rods in air [60-63, 67-69] fewer papers dealt with square-hole ([61, 65]), triangular-hole [58, 59], and triangular-rod [64, 65] photonic crystals. In [67] a decrease of transmission within the gap was detected. However, the authors have not provided a quantitative characterization of this "apparent increase of the band gap strength" but it appears from the plots that the effect is very small and most likely undetectable experimentally. Also, it is necessary to note, that results of [60, 61] and [62, 63] are correlated very well. Particularly, the high stability of the band gap with respect to E_z polarization in square-rod photonic crystals was confirmed.

2.1.3. Three-dimensional photonic crystals.

The TMM was used to study disordered 3D PhCs with a diamond lattice in [70]. The disorder was introduced by moving the lattice points from their ideal positions. The simulations showed that increasing disorder results in smearing of the band gap. For the case of a diamond lattice of spheres (both air spheres in a matrix and high-index spheres in air) the band gap disappeared at disorder amplitudes of $0.1a$, where a is the lattice constant. However, due to computational restrictions a supercell with the width of only 3 conventional lattice cells was used and no proper convergence study was done.

The supercell PWEM was applied to inverse-opal structure to examine the effects of positional and size disorder in [71]. The size of the band gap was estimated by calculation of the density of states. The dependence of the band gap width on the disorder parameter is shown in Fig. 2.14. As can be deduced from the figure the band gap is very sensitive to both types of disorder. In the case shown in Fig. 2.14a a positional disorder with an amplitude of $0.6r_0$ destroys the band gap completely. In the case of a structure with higher refractive index contrast (Fig. 2.14.b) the band gap sustains slightly higher disorder of $0.7r_0$.

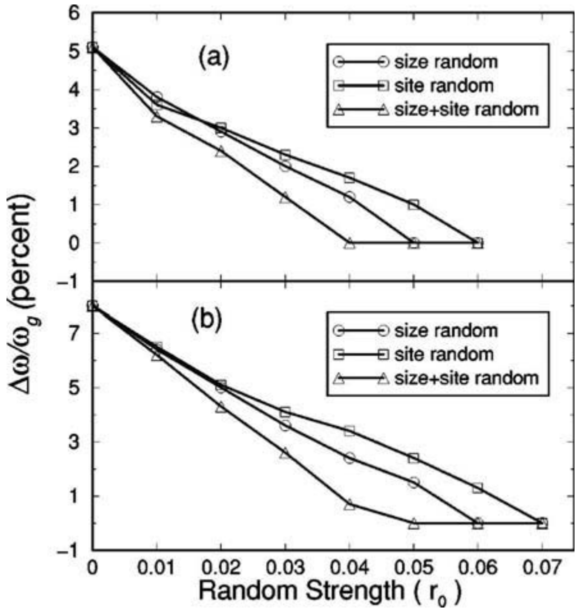

Fig. 2.14. Dependence of the band gap width on the disorder amplitude for size disorder (circles), positional disorder (squares) and both types of disorder simultaneously (triangles) for inverse opal PhCs. The random strength is given in units of the radius of the spheres (r_0). Case (a) corresponds to n=3.6 and f=0.78; (b): n=4 and f=0.78. f is the filling fraction of air spheres and n is the refractive index of the background. Taken from [71].

Both theoretical and experimental investigations of size disorder in opal photonic crystals working in visible part of EM spectrum were performed in [72]. The calculated transmission spectra for different amplitudes of size disorder as well as experimental transmittance are shown in Fig. 2.15. The curves 1-8 correspond to calculated transmittance with disorder varying from 0% to 10% with respect to the diameter of the spheres. The solid line 9 represents the experimental transmittance of the silica-air opal structure. All curves correspond to fcc [111] propagation direction. The inset shows the dependence of attenuation length on disorder amplitude at the midgap frequency. Although the results of simulations also show the effect of increased transmittance within the band gap with increasing disorder, it is important to note that even for the case of 10% disorder (curve 8) the transmittance within the band gap is still as low as 10^{-5}, so the band gap is still clearly defined. The experimental transmittance, however, shows a shallower band gap with a minimal transmittance of approximately 1%.

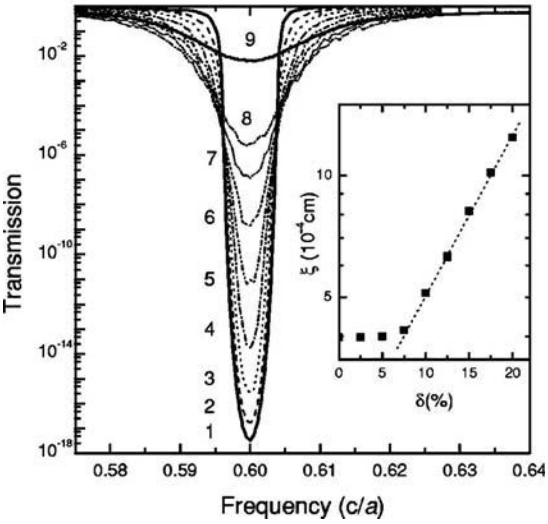

Fig. 2.15. Calculated transmission spectra of a 3D opal PhC with varying disorder. The standard deviation δ of the spheres diameter is 1–0 %, 2–0.5 %, 3–1 %, 4–2 %, 5–3 %, 6–4 %, 7–5 %, 8–10%. Thick solid line 9 is the experimental spectrum. The inset shows the dependence of the attenuation length on disorder parameter for the midgap frequency. Taken from [72].

The general effect of band gap shallowing and broadening with increasing disorder was confirmed in a number of other publications [73, 74, 75, 76, 77, 78]. One should mention, however, that it is very difficult to create a *controlled* disorder in 3D PhCs experimentally in order to directly compare a disordered with a non-disordered structure. Another difficulty in disorder characterization of 3D structures is the large number of possible irregularities. In addition to positional and size variations such effects as stacking faults, grain boundaries, differently oriented domains, point defects and dislocations can affect transmittance and reflectance of a 3D photonic crystal.

2.1.4. Influence of disorder on waveguiding and negative refraction in 2D photonic crystals.

Many real or potential applications of photonic crystals are connected with the possibility of effective light confinement by defects intentionally introduced in otherwise perfect superlattices. For instance, a single defect (e.g. a missing hole or rod) in a 2D photonic crystal acts as a cavity for modes with frequencies inside the gap of the surrounding lattice.

Such a cavity can confine light in the plane of periodicity with very high Q-factor and low modal volume. A line defect (missing column or row) is an effective waveguide where the guiding mechanism is not a total internal reflection but reflection due to a gap in the surrounding lattice. As a result, high transmission through such a waveguide is observed even at high bending angles up to 90 degrees. This subsection gives a review of disorder influence on defect guiding in photonic crystals as well as on negative refraction and superlensing imaging.

Gupta and Ye [79] considered the effect of disorder on superlensing in 2D photonic crystal. A superlens consisting of a square lattice of dielectric rods with ε=14 in air and only E_z polarization is examined. The authors have shown that the positional disorder of $\delta=0.08a$ does not impact the quality of an image significantly while $\delta=0.14a$ sufficiently smears out the image and there is no image at all for $\delta=0.2a$.

X. Wang and K. Kempa [80] investigated numerically the effect of positional and size disorder on subwavelength lensing in 2D photonic crystals. The structures studied consisted of a triangular-lattice array of circular air holes with $r=0.4a$ embedded in a background material with ε=12.96. By analyzing the band structure it was deduced that negative refraction effects will be observed at reduced frequency ω_0=0.31. Transmission calculations were carried out by FDTD. A perfect photonic crystal slab of thickness 7.8a acts as a superlens creating an image of a point source located at the distance 4a from the surface. Introduced disorder worsens the quality of the image. It was found that for disorder amplitudes $d\leq 0.03a$ (for positional disorder) and $d\leq 0.05a$ (for size disorder) the intensity of the image is still high. However, for higher disorders the image smears out very quickly and for $d\geq 0.07a$ an image is of bad quality for both types of disorder. This result was confirmed statistically by the calculation of 30 randomly generated configurations of positional disorder with $d=0.07a$.

The effect of disorder on light confinement in a photonic crystal cavity was investigated by Rodriguez et. al. [81]. The structure studied was a square lattice "rod" PhC with a rod radius 0.2a and a rod dielectric constant ε=12. The cavity was formed by

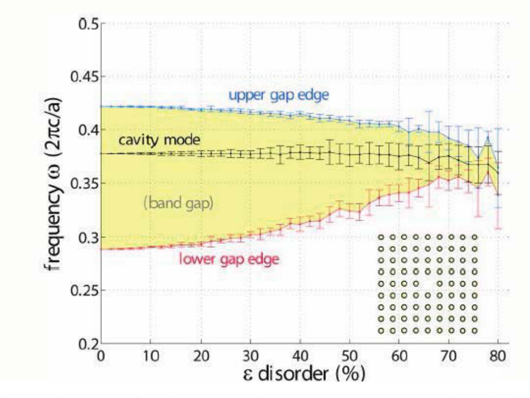

Fig. 2.16. 2D band gap and cavity mode frequencies versus strength of disorder in dielectric constant (maximum percent variation of rod ε). The inset shows the cavity structure. Taken from [81].

removing a single rod. The Q factor of the cavity was derived from FDTD calculations being averaged over 15 random configurations. Three types of disorder were examined: positional with δ_{xy}=0.15*a*; dielectric constant with δ_{ε}=0.15; and size disorder was introduced by adding/removing 20 cylinders with random radii in the range (0; 0.0625*a*) on the surface of each rod. It was shown that Q factor of the cavity almost does not affected by even high amount of any type of disorder. Moreover, in case of positional disorder the Q factor is even higher than that one of the ideal structure. Supercell PWEM calculations showed that a band gap still exists even for such a high amount of disorder of the dielectric constant as 80% (Fig. 2.16). All calculations were carried out only for E_z polarization.

Kuramochi et. al. [82] considered a four-point defect cavity with smaller and shifted holes (radius: 50%, shift: 0.25*a*) in a silicon-air 2D photonic crystal. In this paper the main emphasize was put on the characterization of losses. The authors claim that disorder makes a main contribution to the photonic crystal cavity performance leading to decreasing Q-factor. In order to estimate the modification of Q-factor with increasing disorder the FDTD method was used for a silicon photonic crystal with the following parameters: *a*=420 nm, *r*=0.25*a*. The calculations showed high sensitivity of the cavity Q-factor to disorder in radius (Fig. 2.17). For instance, a radius uncertainty of 3 nm decreases the Q-factor of the cavity to a half the value without disorder which is close to the experimentally measured Q. Such a behavior of cavity Q-factor is strictly opposite to the behavior reported in [81].

Kwan et. al. [83] investigated the influence of disorder on a 90° bend in a W1 waveguide formed in square lattice "rod" type PhC ("W1" means that one row of holes or rods is missing). The dielectric constant and the radius of cylinders were 11.56 and 0.18*a*,

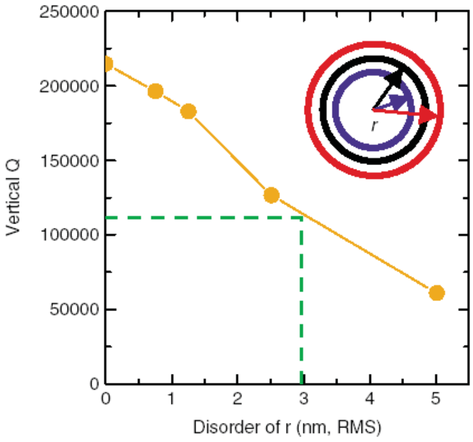

Fig. 2.17. Disorder dependence of the cavity Q-factor as a function of the RMS hole radius obtained by FDTD calculations. Taken from [82].

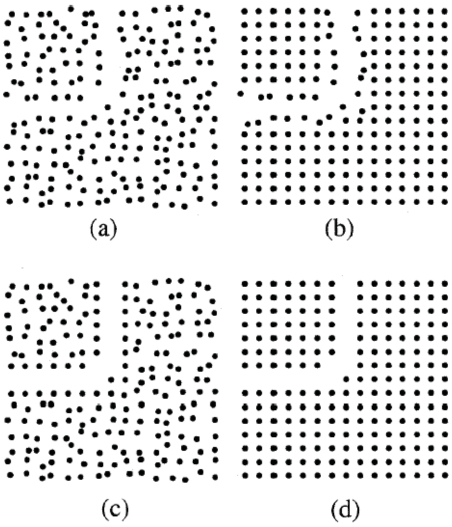

Fig. 2.18. Several particular configurations of disorder introduced in 90° bend in a photonic crystal waveguide: (a) all cylinders are disordered; (b) only those cylinders in the boundary layer are disordered; (c) all cylinders except those in the boundary layer are disordered; (d) no disorder. Taken from [83].

respectively. Three different configurations were considered: (a) all cylinders are disordered; (b) only the cylinders in the boundary layer surrounding the waveguide are disordered; (c) all cylinders except those in the boundary layer surrounding the waveguide are disordered (Fig. 2.18). For each configuration two types of disorder were applied: positional disorder with amplitudes δ_{xy}= 0 - 0.3a and size disorder with random parameter δ_r= 0 - 0.1a. The transmission through the 90° bend was calculated by the multiple scattering method. For configurations (a) and (b) both types of disorder induced a significant decrease of transmission coefficient. However, it appears that for configuration (c) both positional and size disorder have almost no effect on the transmission through the waveguide.

Langtry et. al. [84] considered the transmission through a straight W1 waveguide in a square lattice "rod" type photonic crystal. All cylinders had the same radius r = 0.3a but the refractive index of each one was randomized with amplitudes of δ_n = 0.1n_0; 0.2n_0; and 0.3n_0 around the mean value of n_0=3. Little degradation of waveguiding was observed for δ_n=0.1n_0; noticeable degradation for δ_n=0.2n_0; and for δ_n=0.3n_0 the EM energy was effectively scattered by the structure and consequently transmission through the waveguide was almost zero.

Poulton et. al. [85] considered the effect of sidewall roughness on transmission through a strip waveguide as well as through a photonic crystal W1 waveguide.

In the first case a silicon strip on a glass substrate has the same width and height, h=w=0.365 μm; the sidewall root mean square roughness was ranged from σ=5 to σ=50 nm; and the operating wavelength was λ=1.55 μm. The simulations were done by a vectorial wavelet-based time domain collocation method. It was found that the attenuation grows significantly (> 0.2 dB/μm) for rms values of more than 20 nm. Furthermore, the TE-mode (E field is parallel to substrate plane) attenuates much faster than TM-mode.

The W1 photonic crystal waveguide was represented by a missing row of holes in a periodic structure with a=484 nm and r=186 nm in InP (n=3.1). The rms magnitude of the sidewall perturbation was σ=10 nm. Calculations of the transmission over an ensemble of 194 sidewall-perturbation realizations showed that the structure is tolerant to sidewall perturbations of the magnitude given above. About 92 % of calculated structures retain at least 90 % of the transmission of the unperturbed waveguide. The sidewall perturbations can even improve the transmission – this was observed in 59% of cases.

Gerache and Andriani [86] investigated theoretically the effect of disorder in radius on losses in a W1 waveguide made in triangular lattice "hole" type photonic crystal. Two types of structures were considered: silicon-air PhC membranes and SOI (silicon-on-insulator) waveguides. Disorder was characterized by the root mean square deviation Δr. The structures investigated had the following parameters: a=400 nm, r=0.275a, slab thickness d= 220 nm. Calculated out-of-plane losses are compared to the experimental results obtained by Notomi et al. [87]. It was found out that for disorder parameters of

Δr=3.2 nm and Δr=2.2 nm the experimentally measured values of propagation losses were very well reproduced for silicon-air and SOI structures, respectively. A new design of low-loss high-bandwidth photonic crystal waveguides was proposed. For membrane-type structures, it was shown that increasing the waveguide channel width to W=1.5W_0 should allow to achieve a large propagation bandwidth with predicted losses well below 0.1 dB/mm.

Thus, in general the effect of disorder could be defined as worsening the cavity or guiding characteristics. However, there are some papers apart from this conclusion. In [81] simulations show practical independence of Q-factor from disorder. It is necessary to note that rods-in-air disordered square-lattice structures are well investigated and most of the papers reported band gap reduction even for smaller amount of disorder [60, 61, 62, 63, 66]. An interesting result is obtained in [82]: line defect guiding requires only the boundary layer surrounding the defect to be ordered, disorder in rest of the photonic crystal has very weak influence on transmission through the waveguide. In [85] sidewall roughness even increased transmission through the waveguide in 59% of the cases studied.

We suppose that the different results, discussed above, resulted from the high sensitivity of guiding and cavity effects to particular system properties such as geometry, refractive indices, band gap width, frequency of defect mode, etc. For instance, we can surmise that if the frequency of guided mode is located in the center of the lowest band gap, which usually sustains the highest amount of disorder, the perturbing effect of disorder is minimal.

Conclusions

Intuitively one can suppose that since the existence of band gaps in a photonic crystal is a consequence of refractive index periodicity, the destruction of that periodicity should result in disappearance of the band gaps. The major part of the reviewed papers confirms this general trend. There are some reports, however, which show an increase of the band gap width and/or depth with increasing disorder [53, 54, 67] or very weak dependence of the band gap width on disorder [81].

It should be mentioned that we have found very few experimental papers where the disorder was created intentionally and where the optical properties of the *same* structure with different amounts of disorder were directly compared experimentally.

Another point which makes a comparison between different papers difficult is the large number of photonic crystal parameters which can influence the results. Lattice symmetry, shape of the "atoms", refractive index contrast, filling fractions – all these parameters can influence the dependence of the photonic crystal properties on disorder.

Thus, the problem of disorder in photonic crystals is still a topical problem. In section 2.2 we examine both numerically and experimentally the influence of surface roughness on the properties of 1D PhC. We have developed a 2D FDTD model for calculation of transmission, reflection, and EM field distribution in 1D PhC with surface roughness. Experimentally, we have fabricated 1D PhCs with controllable roughness and transmission spectra of the same structure with and without surface roughness were compared [88].

In section 2.3 we present 3D FDTD simulations of specific colloidal 3D PhCs with non-close-packed arrangement of silica spheres in aqueous medium [89].The main aim of this section is to investigate theoretically the wave propagation and the influence of disorder on the optical properties of the 3D PhCs.

2.2. Surface roughness in one-dimensional photonic crystals: simulations and experiments

In this section we present numerical and experimental investigations of the influence of surface roughness on the optical properties of 1D PhC. The problem of surface roughness is of particular interest since surface imperfections inevitably appear during fabrication of nanometer and micrometer-sized photonic structures. Our aim is to create *controlled* roughness and to compare the optical properties of the *same* structure with and without surface roughness. The main points of interest in our opinion are the mechanism of the band gap smearing, estimation of the amount of disorder under which a PhC still exhibits band gaps and the determination of the relation between transmission, reflection and scattering. Transmission experiments were performed in the microwave region on a mm-sized structure with a roughness of the order of 10 percent. Due to the scalability of Maxwell's equations the main conclusions are valid for down-sized structures like submicron-sized photonic crystals for the near infrared and visible regions.

2.2.1. Description of the model

It is important to define the surface roughness in a clear and reproducible way consistent with the sample used in the experiment. In our 2D model we consider each high-index layer of a PhC as being composed of thin bars with the same width (Fig. 2.19). In the case of a structurally perfect photonic crystal with zero-roughness all these bars have the same length. The surface roughness is created by a random change of the length of each bar.

Mathematically the roughness is introduced in the following way: the lengths of the bars (l_{bar}) are varied randomly around the length in the perfect structure (l_h) according to

$$l_{bar} = l_h(1 + \delta \cdot P_{-1;1}) . \tag{2.3}$$

$P_{-1;1}$ is a uniformly distributed random value in the range **[-1;1]**, and δ is the roughness amplitude. As an example, for δ=0.1 the value of l_{bar} varies between 0.9l_h and 1.1l_h. The position of the center of each bar is the same as in the perfect PhC. Thus, the top and the bottom sides of each individual layer have the same roughness profile. The roughness profiles are different for the different layers. This corresponds to five different realizations of roughness within one PhC. Therefore, we suppose that the roughness being the same on both sides of a layer does not disturb generality of the model. The scheme of a part of a layer with roughness is depicted in Fig. 2.19.

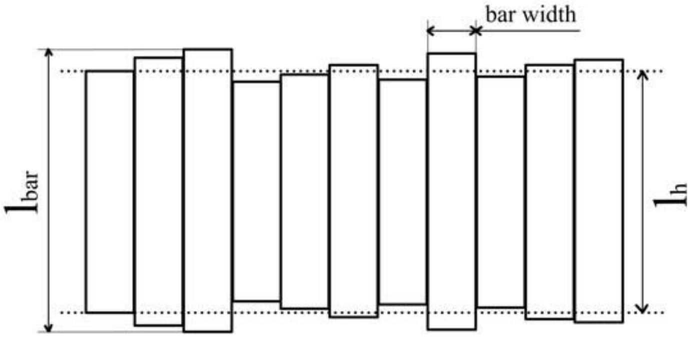

Fig. 2.19. The scheme of a part of a layer with roughness used in our model.

The simulations (in accordance with the PhCs used in the experiments) were carried out for a five-layer dielectric-air structure with the following parameters: the thickness of the dielectric layers is 1.11 mm, the air spacings between the plates are 1.21 mm which corresponds to a period of the structure a=2.32 mm. The total number of bars in each layer (N_R) defines the "roughness resolution". Table 2.1 shows the correspondence between the resolution and the width of a single bar. The total width of the layers in the model is 15a or approximately 35 mm; in the experiment the lateral dimensions of the plates are 24x39 mm. The dielectric constant is assumed to be 9.86 since ultra-pure alumina is used as the dielectric material in the experiment and this value gave the best fit to the experimental spectrum of the structurally perfect PhC.

Table 2.1

Resolution (number of the bars in each layer)	The width of a single bar, mm
N_R=150	0.232
N_R =300	0.116
N_R =600	0.058

The transmission spectra were calculated by means of Rsoft FullWAVE™ [51] commercial package. In Fig. 2.20 the general view of the problem is shown. The horizontal bar 1 represents the source which emits a plane wave only in the direction of the PhC. The horizontal bars 2 are transparent time monitors which record the EM energy flux as a function of time. The purple frame shows the edge of the computational domain with perfectly matched layers, i.e. totally absorbing boundaries. An additional MatLab program was written to introduce random values into the FullWAVE input files. This program is listed in Appendix II.

Two simulation techniques were used: direct finite-difference-time-domain (FDTD) calculations (subsection 2.2.5) and FDTD calculations followed by a fast Fourier transform (subsections 2.2.3 and 2.2.4). In the latter case a Gaussian-pulse excitation is used. A monitor records the energy flux as a function of time and then the fast Fourier transform (FFT) is applied to this function. As a result we obtain a transmission spectrum normalized to the power emitted by the source.

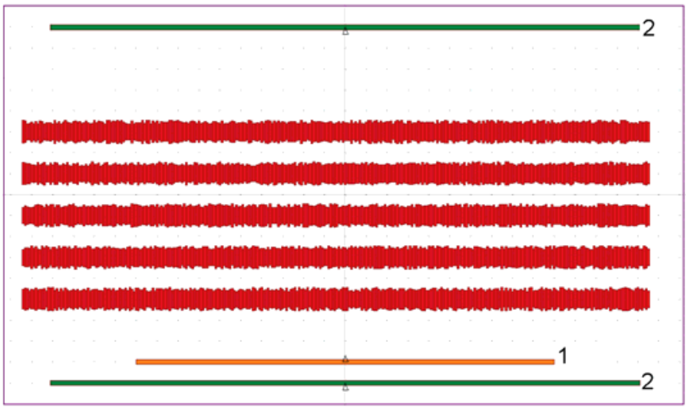

Fig. 2.20. General view of the problem. The horizontal bar 1 is the source. The bars 2 are the monitors. The purple frame is the edge of the computational domain with PML absorbing boundary conditions.

The size of the FDTD computational cell is 1/128 with respect to the period of the PhC. We have tested the problem also on a 1/256 grid but no difference in the results was observed. Using the FFT to calculate transmission spectra can result in some numerical artifacts for low frequencies, since a time limit is set for the calculations time. In order to check the range of validity, the transmission of the structurally perfect PhC was also simulated by the MULTEM2 [90, 91] program utilizing the multiple scattering method. The very good coincidence observed for the perfect structure between FullWAVE™ and MULTEM2 spectra for frequencies above 5 GHz confirms that we have chosen a sufficiently fine grid and a sufficiently long calculation time in our FDTD simulations. This is also valid for the simulations of PhCs with roughness where MULTEM2 is not applicable.

The model described above is a two-dimensional model. Nevertheless, we expect that deviations from results of a three-dimensional model are small. The reasons are: (a) The transmission is averaged over 10 different realizations of the roughness. This can be considered as being equivalent to 10 layers on top of each other in the third direction. That way the roughness varying in the third dimension is taken into account to some extent. (b) However, from the edges of a PhC extended in the third direction some light would be scattered which is not detected by the monitors of the two-dimensional calculation. This will not affect the general spectral features, it can only cause a lower transmission or reflection than calculated in the two-dimensional model.

2.2.2. Experimental: sample characterization and measuring setup.

Experimentally fabricated 1D PhCs consist of five 1.11 mm thick alumina plates separated by air spacings of 1.21 mm. With these dimensions the lowest transmission bands are in the microwave range of the electromagnetic spectrum. The photos of a single plate and the 1D PhC in a holder are shown in Figs. 2.21a and 2.21b, respectively.

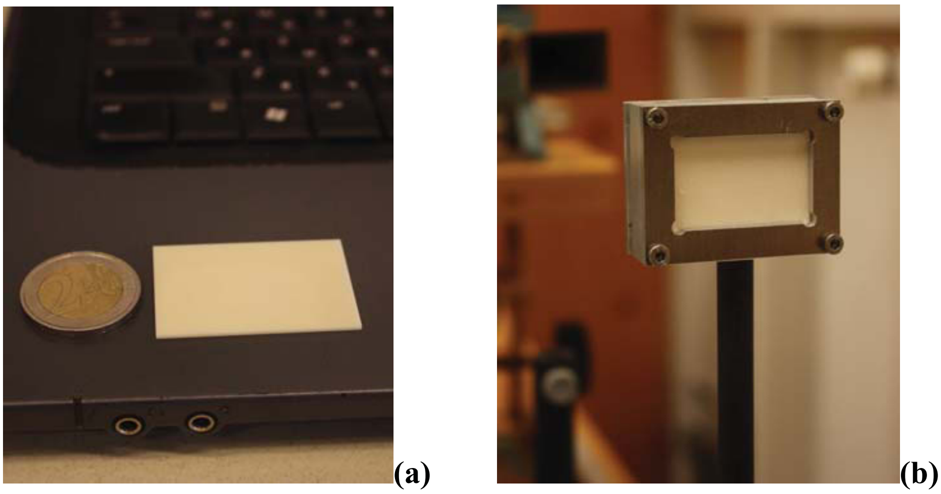

Fig. 2.21. (a) A single alumina plate with a 2 euro coin on a laptop. (b) One-dimensional alumina-air PhC in a holder.

The surface roughness was created by gluing alumina powder to both surfaces of each plate. For the determination of the roughness we used optical microscopy and profilometry. Additionally, atomic force microscopy was used for the surface of the uncovered alumina plates whose rms roughness was found to be 0.7 μm. This is considered to be negligible in the present context.

The grains of the alumina powder have irregular shape with the dimensions varying from 30 to 140 μm. About 75% of the grains have sizes in the range 60-90 μm. In Fig. 2.22 a photo of powder grains to be glued to the plates is shown.

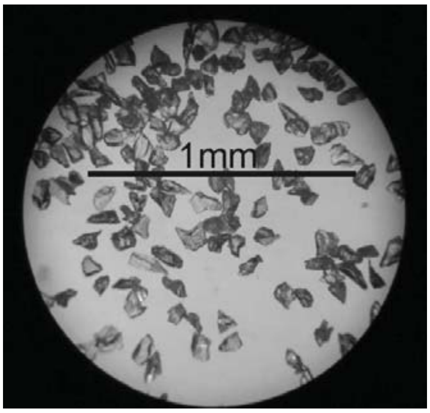

Fig. 2.22. The photo of the alumina powder grains to be glued to alumina plates.

Optical confocal microscopy was used for the measurements of the surface roughness profiles. The measurements taken over the edge between a covered and an uncovered parts of a plate (the edge is located approximately at x=150 μm) are shown in Fig. 2.23. The thickness of the glued layer is estimated to vary from 70 to 140 μm.

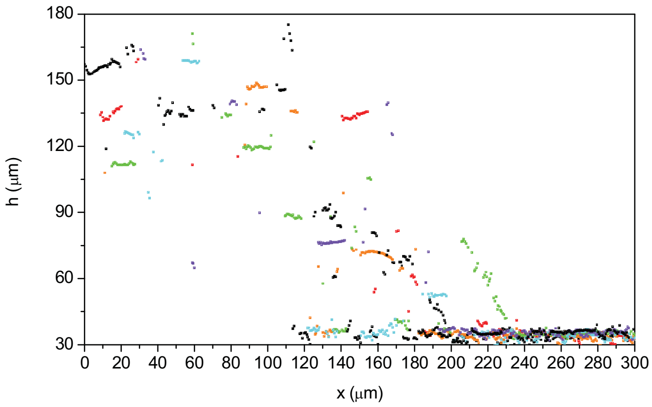

Fig. 2.23. The profiles of the alumina plate with glued alumina powder measured by confocal optical microscopy. The measurements were taken over the edge between the covered and uncovered parts (the edge is located approx. at x=150 μm). Different colors correspond to 7 different profile measurements.

In addition to optical methods we have also performed profilometry measurements. A typical roughness profile is shown in Fig. 2.24. The maximum peaks obtained from profilometry were around 70 μm (in Fig. 2.24: 68.6 μm) which is consistent with the results obtained from confocal microscopy. Thus, although some of the grains have larger dimensions, up to 140 μm, the typical height variation of the surface covered with the powder is 30-60 μm. We explain this fact by the existence of the layer of glue with the thickness 30-40 μm on the surface. The grains are partially submerged in this glue layer, so, the resulting roughness profiles have the peak heights which are on average lower than the sizes of the grains. Moreover, many powder grains are large in one dimension only, thus, if such grains are "standing" on the surface their sharp and thin ends are hardly detectable both by the confocal microscopy and by the profilometry.

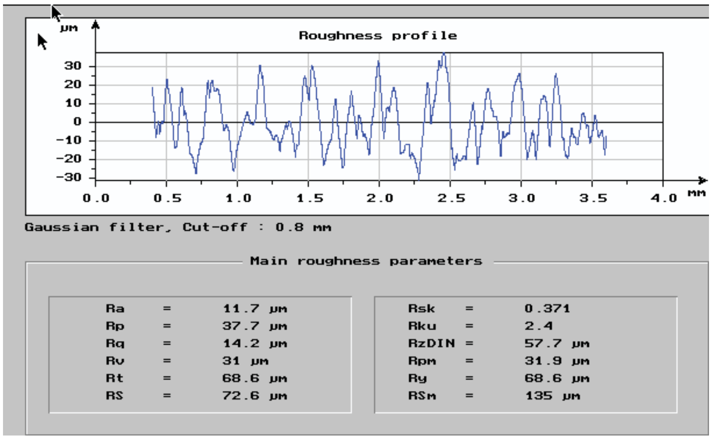

```
Gaussian filter, Cut-off : 0.8 mm
```

```
Ra     =    11.7 μm        Rsk    =    0.371
Rp     =    37.7 μm        Rku    =    2.4
Rq     =    14.2 μm        RzDIN  =    57.7 μm
Rv     =    31 μm          Rpm    =    31.9 μm
Rt     =    68.6 μm        Ry     =    68.6 μm
RS     =    72.6 μm        RSm    =    135 μm
```

Fig. 2.24. The profilometry measurement of the surface roughness.

Transmission through the samples with and without roughness was measured in the microwave Q-band (33-50 GHz), V-band (50-75 GHz), and W-band (75-110 GHz) using backward wave oscillator sources Siemens RWO-50S, RWO-75S, and RWO-110S respectively.

The scheme of the experimental setup is presented in Fig. 2.25. The thick connecting lines depict the waveguides while the thin ones correspond to signal cables. The "microwave source" denotes one of the mentioned backward wave oscillators; the "isolator" absorbs the reflected irradiation propagating back to the source; the "variable attenuator" is needed for better control of the irradiated power. After interaction with the sample the microwaves are collected by the receiving horn antenna and guided to the "thermistor mount". The absorption of the microwaves by the thermistor results in a change of its resistance proportional to the absorbed power. The signal obtained from the themistor is transformed by the "power meter" into a voltage signal which is recorded in a computer after analog-to-digital conversion ("ADC"). Simultaneously the computer obtains the current value of the frequency of the source, thus a dependence of transmission signal on the frequency is obtained. In a single measurement run we record the transmission for the entire working range of a source.

Due to the use of the horn antennas the direction of EM wave propagation is essentially normal to the surface of the PhC. The sample was surrounded by a sheet of absorbing material to block possible in-direct waves (e.g. reflected by the table or optical bench). Thus, all the energy absorbed by a detector comes from the microwaves which passed through the sample.

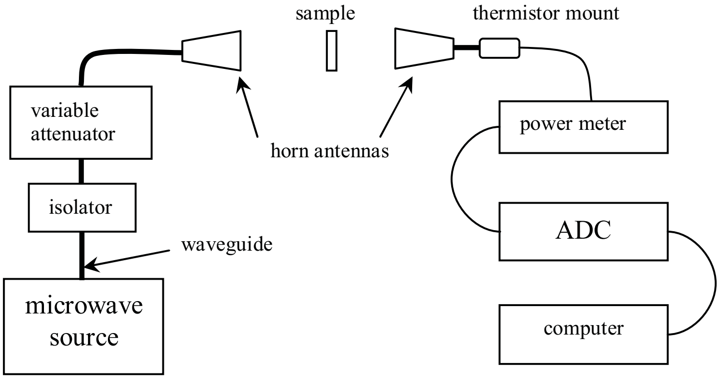

Fig. 2.25. Schematic description of the experimental setup. More detailed information is in text.

In order to exclude the influence of the metal holder on the measurements we took the transmittance through the empty holder as a reference transmittance. Additionally, the distance from the sample to horn antennas was much larger than the wavelength, so the waves diffracted on the edges of the metal holder should not contribute to the measured transmittance.

Due to the very low signal within the band gap regions the transmission was measured there with increased sensitivity of the power meter in order to obtain a better signal-to-noise ratio.

2.2.3 Simulations results.

The calculated transmission spectra for the cases δ=0.2, N_R=300 and δ=0.4, N_R =300 are presented in Figs. 2.26a and 2.26b, respectively. The solid black curve shows the transmission of the zero-roughness structure with the thickness of the high-index layers l_h=1.11 mm. Each of the thin gray curves (10 in each spectrum) is the transmittance of sample with an individual realization of the roughness configuration. The dashed blue curve shows the transmission averaged over an ensemble of 10 structures with the same δ (thin gray curves). The frequency 100 GHz corresponds to a reduced frequency ωa/2πc=0.77.

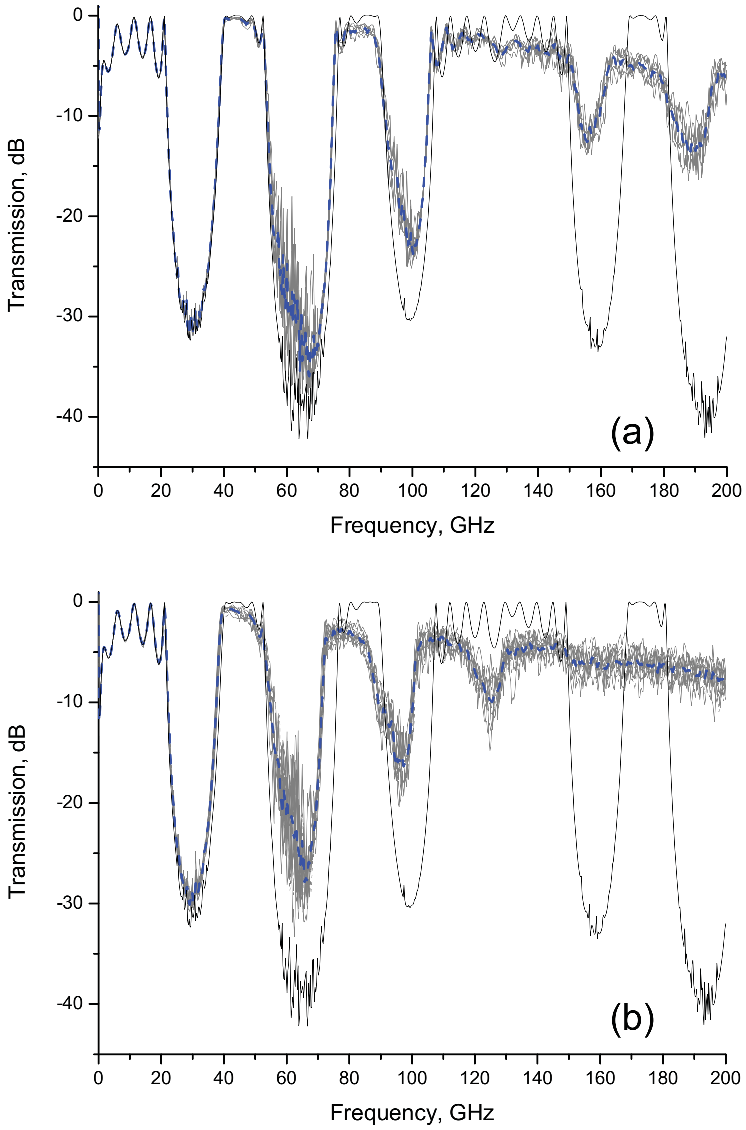

Fig. 2.26. Calculated normal-incidence transmission spectra of the 1D PhC with surface roughness: $\delta=0.2$, $N_R=300$ (a); $\delta=0.4$, $N_R=300$ (b). Solid black curve: zero-roughness structure; gray curves: 10 different realizations of surface roughness with the same δ; dashed blue curve: the transmission averaged over the ensemble of the 10 realizations. 100 GHz corresponds to a reduced frequency ωa/2πc=0.77.

It is clearly seen from Fig. 2.26 that the surface roughness practically does not affect the lowest band gap even for δ=0.4 (Fig. 2.26b). However, the higher the frequency the higher is the effect of the surface roughness. The gaps shrink, the interference structure within the transmission bands is smeared out, and the fine structure of the spectra depends on the details of the realization of the roughness. This is easily understandable since the frequency of the center of the first band gap (34 GHz) corresponds to a wavelength λ/n=2.8 mm that is more than 10 times larger than the size of the roughness features. The center of the third band gap (100 GHz) corresponds to a wavelength of λ/n=0.96 mm that closely approaches the order of the dimensions of the roughness features.

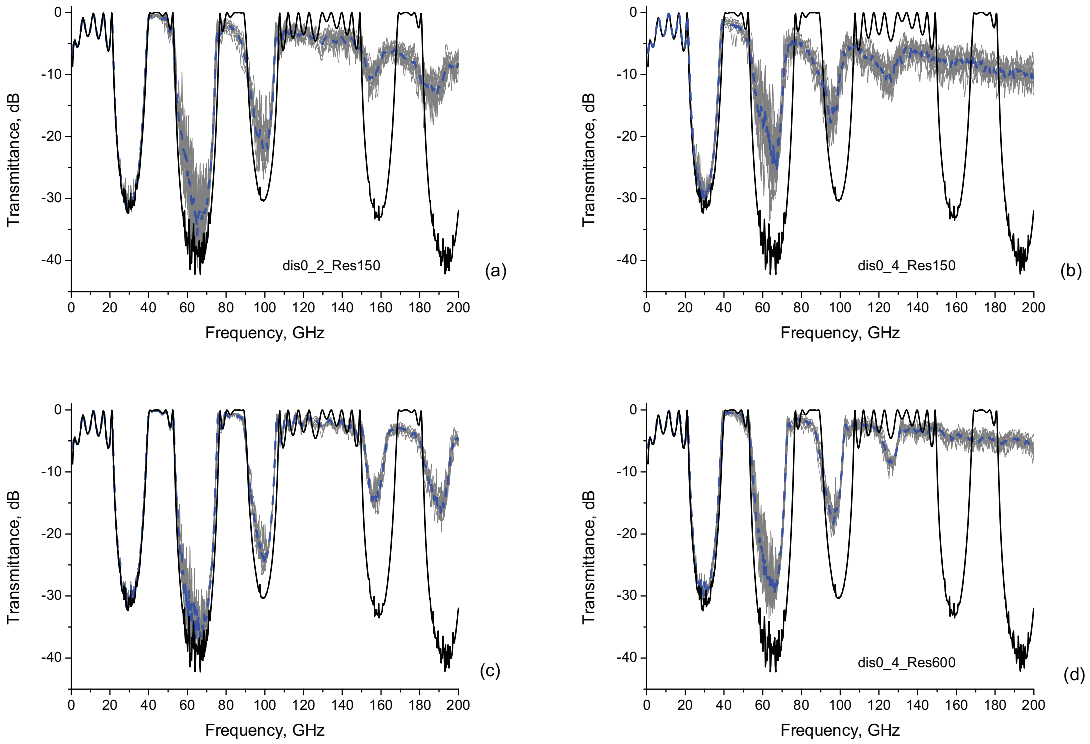

Fig. 2.27. The same as in Fig. 2.26 but for N_R=150, δ=0.2 (a); N_R=150, δ=0.4 (b); N_R=600, δ=0.2 (c); N_R=600, δ=0.4 (d).

The results of similar calculations but for N_R=150, δ=0.2; N_R=150, δ=0.4; N_R=600, δ=0.2; N_R=600, δ=0.4 are shown in Fig. 2.27a, 2.27b, 2.27c, and 2.27d, respectively. The effect of surface roughness for these cases is very similar to that shown in Fig. 2.26. The low-frequency part of the spectra including the first band gap sustains even disorder with δ=0.4. With increasing roughness the transmittance inside the second and third band gap is increased while the transmittance between the band gaps decreases; for δ=0.4 above a certain frequency the spectra do not exhibit any bands or gaps. However, one should point out, that structures with higher roughness resolution (Figs. 2.27c and 2.27d) are less sensitive to roughness than the structures with lower roughness resolution (Figs. 2.27a and 2.27b).

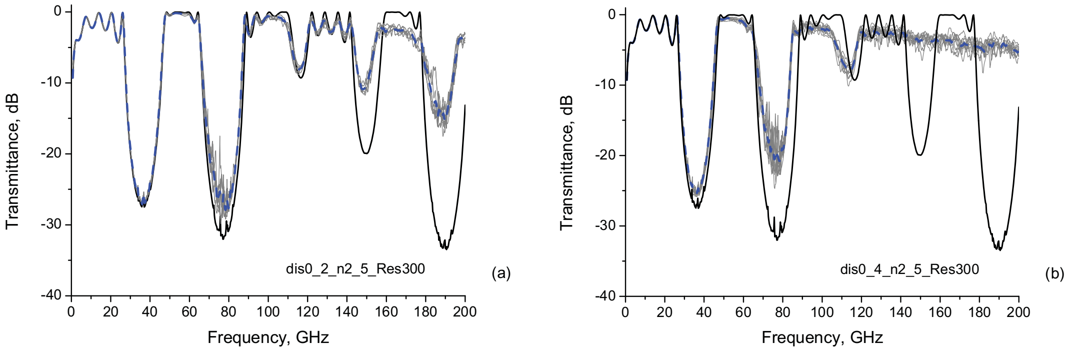

Fig. 2.28. The same as Fig. 2.26 but for the lower refractive index of the plates: n=2.5.

For further comparison we have performed the same calculations as shown in Fig. 2.26 but for a refractive index of the plates of 2.5 instead of 3.14 (Fig. 2.28). Again, the similar effect of roughness is observed.

We therefore conclude that the main effect of surface roughness – scattering of a plane wave on the surface features – becomes significant if $\lambda / n \sim l_h \cdot \delta$, where n is the refractive index of the high-index layers. More precisely we can state that if the condition $\lambda / n > 10 \cdot l_h \cdot \delta$ is satisfied then the effect of surface roughness is small, while if $\lambda / n < 4 \cdot l_h \cdot \delta$ then the scattering is too high and the concept of gaps separated by transmission bands is no more applicable.

We have also simulated a 10-layer structure with the same parameters. These additional results show that the conclusions are generally valid for a variety of 1D PhC.

Experiment-oriented simulations.

In the experiment the surface roughness is realized by gluing alumina powder to both sides of each plate. Obviously, in order to simulate such a structure we have to take into account the fact that the average thickness of each plate is now higher compared to the case without the powder. In other words, since we always keep the lattice constant unchanged, the air filling fraction in the experimental structure with roughness will be lower compare to the zero-roughness case. According to the experimental roughness parameters, we have used the following parameters for "experiment-oriented" simulation (Fig. 2.29, gray curves): l_h=1.19 mm, δ=0.12, N_R=600. Please note, that δ=0.12 corresponds to the roughness with amplitude 6% on the *each side* of a plate. From the microscopic inspection we conclude that a thin layer of glue on the surface of the plates has also to be taken into account. In the simulation its thickness is 35 μm and its dielectric constant 2.25. With these values the overall agreement is very good, particularly for the band width and the positions of the band edges.

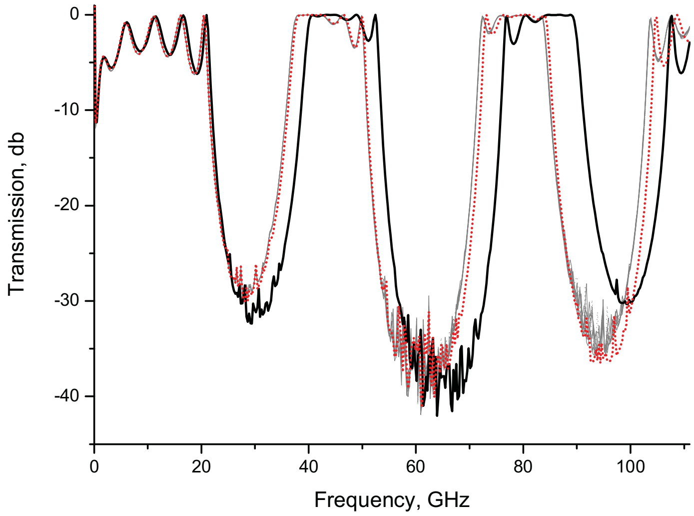

Fig. 2.29. The "experiment-oriented" simulation. Solid black curve: perfect structure with $l_h=1.11$ *mm*; dotted red curve: perfect structure with increased thickness $l_h=1.19$ *mm*; gray curves: 10 different realizations of surface roughness with the same δ: $l_h=1.19$ mm, $\delta=0.12$, $N_R=600$.

The increased average thickness of the high-index layers results in a significant shift of the entire spectrum to lower frequencies compare to initial structure with l_h=1.11 mm. At the same time, δ is small and the effect of the details of the disorder is nearly negligible since the 10 different realizations represented by the gray curves give practically the same spectra.

In order to elucidate the shifts of the characteristic features in the transmission curves of Fig. 2.29 we plot the dependence of the three lowest gaps on layer thickness for a perfect 1D PhC (Fig. 2.30). This gap map was calculated by the plane-wave expansion method using BandSOLVE™ [51] commercial package. A cross-section made at the left vertical line shows the positions and widths of the gaps that correspond to the solid black transmission curve in Fig. 2.29. i.e. a zero-roughness PhC with l_h=1.11 mm. The right vertical line indicates the situation for the red dotted curve in Fig. 2.29 calculated for a zero-roughness structure with increased layers thickness of l_h=1.19 mm. By considering this gap map one can conclude that the increase of the thickness of the layers from 1.11 mm to 1.19 mm results in the redshift of the all three band gaps, the two lowest band gaps become also slightly narrower, while the third band gap becomes wider. All these effects are clearly visible in the transmittance spectra shown in Fig. 2.29.

Thus, for the experiment-oriented simulation two separate effects contribute: (i) a red-shift of the photonic band structure due to the increase of the average thickness of the high-index plates and (ii) the scattering of EM waves at the surface features which are introduced by formula (2.3).

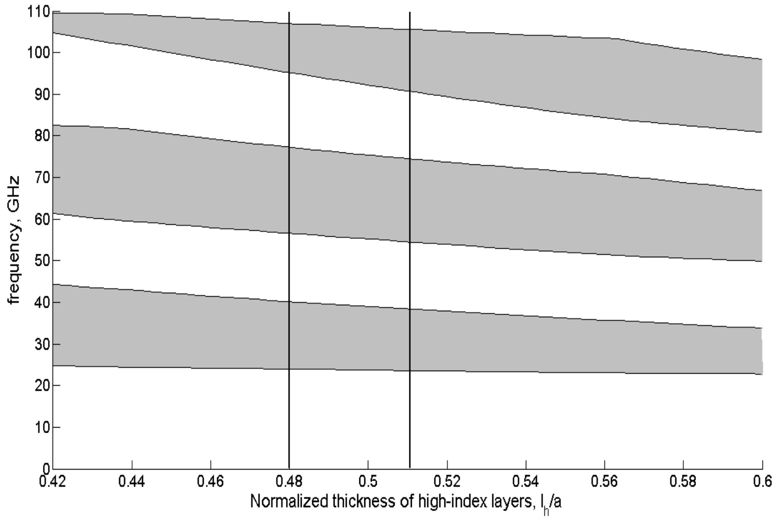

Fig. 2.30. The gap map of a perfect 1D PhC. The x-axis is the thickness of high-index layers in units of the lattice constant. The band gaps are the shaded regions. The left and the right vertical lines correspond to the values of l_h used for calculations of the black solid and black dotted lines in Fig. 2.29, respectively. The lattice constant is a=2.32 mm.

2.2.4 Experimental transmission spectra.

The experimental and simulated transmission spectra in the range 33-115 GHz are joined in Fig. 2.31. In the upper plot (Fig. 2.31a) the experimental (blue curve) and theoretical (black curve) transmission for zero-roughness PhC are presented. The lower plot (Fig. 2.31b) shows two experimental transmission curves (blue and red) for two different samples with the same kind of powder and theoretical transmission of PhC with roughness (black) taken from Fig. 2.29, viz. for the following simulation parameters: l_h=1.19 mm, δ=0.12, N_R=600. Due to a proper choice of the reference transmission and sensitivity regimes of the power meter we were able to measure the transmission spectra in dB units including the band gaps regions where the transmittance is up to 4 orders of magnitude lower than then within transmission bands. The overall agreement is considered as very good, especially taking into account the fact that calculated spectra are *normalized to the power irradiated by the source* while the experimental ones are *normalized to the reference transmission spectrum* (empty metal frame). Of course there are some discrepancies which are, in principle, inevitable when comparing an idealized 2D model with 3D experimental measurements.

The redshift of the experimental transmission curves due to the glued powder is clearly seen in Fig. 2.31b. The third band gap (around 95 GHz) of PhCs with disorder is slightly narrower in the measurements than in the calculations. In addition, the measured transmission at the upper edges of the second and third gaps (~73 GHz and ~105 GHz, respectively) is lower than calculated. These discrepancies might be due to the fact that the calculations are performed for a 2D model, so scattering in the third dimension is not taken into account.

Thus, our experimental measurements show that main effect of the alumina powder glued on the both sides of each alumina plate is the redshift of the transmittance curve. The effect of surface roughness itself, which is about 6% of the thickness of the plates, on the depths and widths of the band gaps is considered to be hardly detectable.

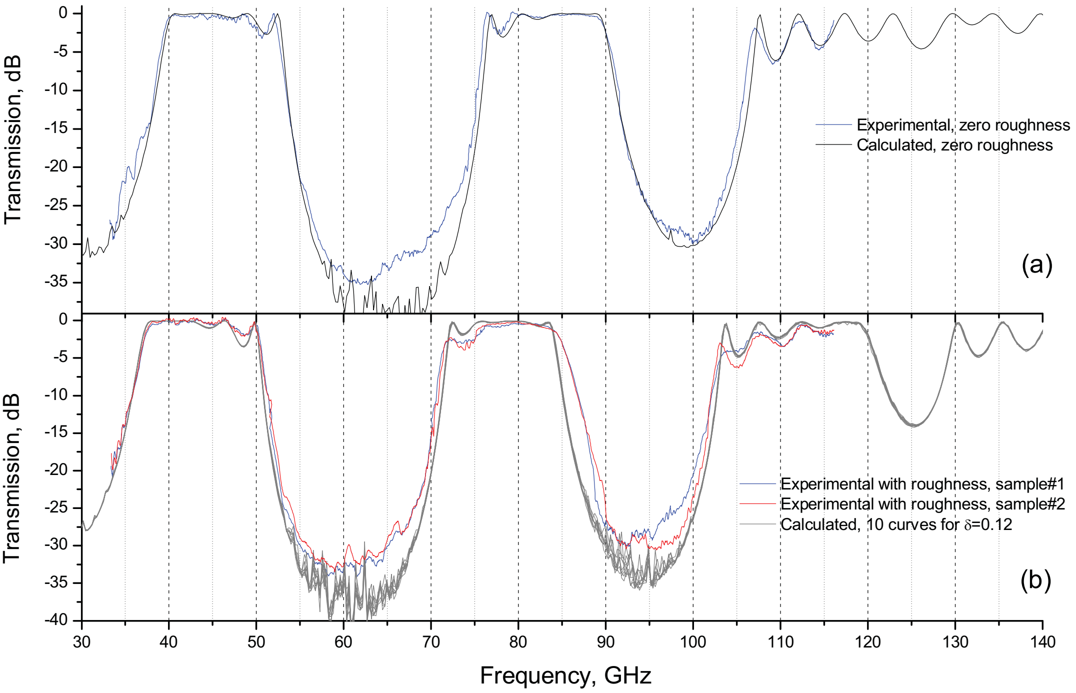

Fig. 2.31. The transmission spectra in the range 33-115 GHz. (a): transmission of a PhC with zero roughness, the blue curve is experimental, the black curve is calculated. (b): transmission of a structure with roughness, blue and red curves represent two experimental transmission curves for two different samples with the same kind of powder; gray curves are simulated transmission of a PhC with roughness taken from Fig. 2.29

2.2.5 Simulation of wave propagation: exploring scattering effects

In order to get a deeper insight into the processes of the scattering of electromagnetic waves in roughened 1D photonic crystals the field distribution patterns obtained by FDTD calculations are investigated. Since in this case the PhC is irradiated by a monochromatic wave there are two important cases: the frequency lies (i) in a band gap or (ii) in a transmission band.

It is also very interesting to investigate the dependence of transmission spectra on the geometry of the problem. Due to the scattering the detected transmission may depend on the positions of the monitors and their dimensions with respect to the period of the structure and the wavelength. For this purpose an extended model was used (Fig. 2.32). Two pairs of monitors are used now, one pair is located near the sample and records "near-field" transmission and reflection. The other pair records the "far-field" transmission and reflection.

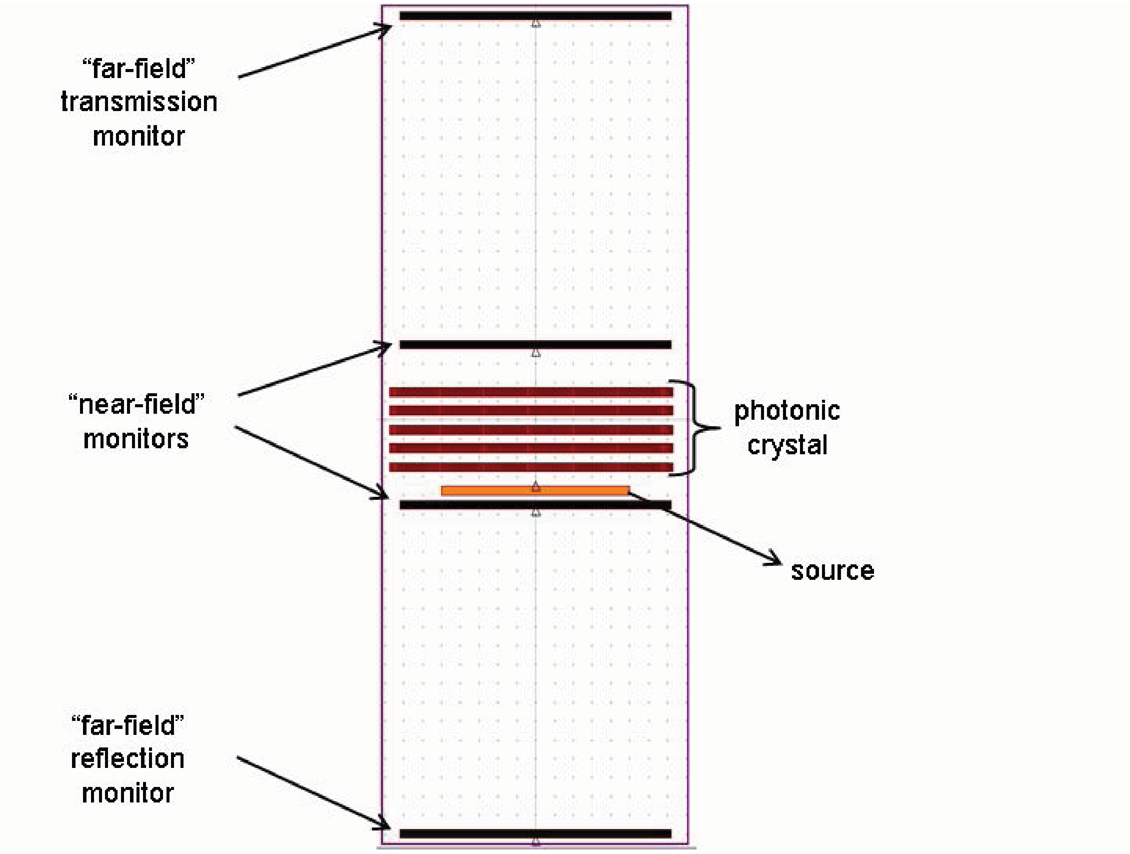

Fig. 2.32. The model for comparison of near- and far-field transmission and reflection.

Since the model does not include lossy materials and we use the PML absorbing boundary conditions at all edges of the computational domain, the scattered power can be treated as that part of the power which is not recorded either by a transmission or reflection monitor and can be calculated by a simple formula S=1-T-R, where T and R are the transmittance and reflectance, respectively.

In Fig. 2.33 the EM field distribution patterns are shown for a frequency of the source situated in the center of the second gap (64 GHz) for a perfect structure (a) and for a PhC with roughness amplitude δ=0.4 (b). It should be outlined that surface roughness with δ=0.4 is too high to simulate any actually observed fabrication imperfections. We explore the case here in order to obtain more pronounced scattering effects and to observe their influence on the band gaps. In the case of the perfect PhC the near-field transmission and reflection are 0.03% and 99.7%, respectively, whereas in far-field the transmission is 0.01% and the reflection is 98.7%. Ideally, in the absence of absorption and scattering the sum of transmission and reflection must be 100%. However, in our calculations we have small deviations due to the diffraction effects at the edges of the beam and due to the finite lateral size of the PhC. The roughened photonic crystal (Fig. 2.33b) still exhibits low transmission. Quantitatively, the near-field transmission and reflection now are 0.6% and

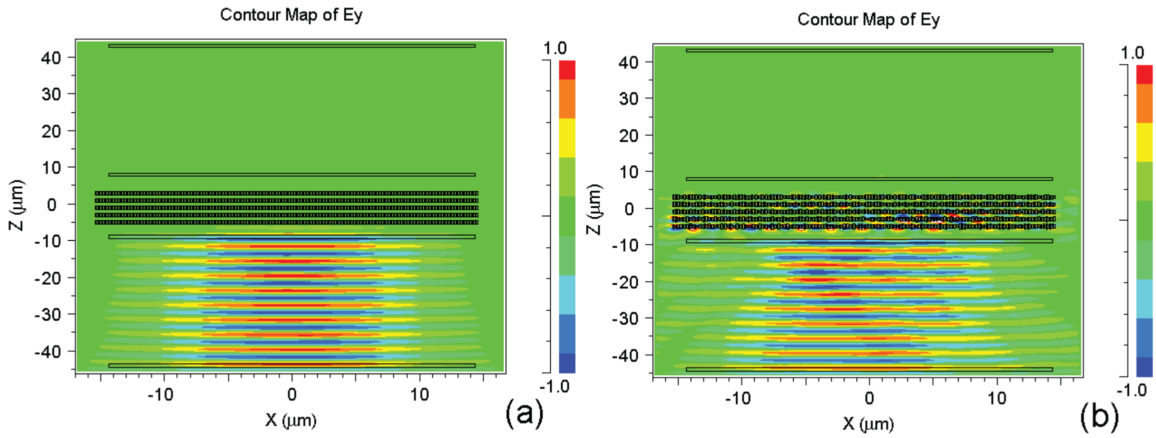

Figure 2.33. The field distribution patterns for a perfect PhC (a) and for a PhC with roughness amplitude $\delta=0.4$ (b). There are two pairs of monitors on each plot, one pair is located near the sample and records "near-field" transmission and reflection, the other pair records "far-field" transmission and refection. In all the cases a plane wave is generated by the source located at $z=-8\ \mu m$ and propagates only toward the PhC. The frequency of the wave is *64 GHz* (vacuum wavelength $\lambda=4.69\ mm$). It corresponds to the center of the second gap.

90%, respectively. The far-field transmission is 0.35% and the reflection is 89%. The values of transmittance and reflectance measured at near- and far-fields are summarized in Table 2.2. As we see from these values the reflection from the roughened structure is almost 10% lower. It can be also seen in Fig. 2.33b that the light "localizes" on the roughness features (red and blue spots inside the PhC), in addition, a part of the EM energy is scattered at the angles close to 90 degrees. Thus, although the transmittance within the second band gap of the PhC with roughness is still low, about 10% of the emitted power is lost due to scattering. This is already very significant if a PhC suppose to work as a reflecting part of some device.

Table 2.2. Transmission, reflection and scattering recorded at near- and far-field at *f*=64 GHz for the 1D PhC with and without disorder. Subscript "perfect" means the values (T, R, S) calculated for the structure without disorder, Fig. 2.33a. Subscript "roughened" is for the structure with roughness, Fig. 2.33b.

	$\mathbf{T_{perfect}}$	$\mathbf{R_{perfect}}$	$\mathbf{S_{perfect}}$	$\mathbf{T_{roughened}}$	$\mathbf{R_{roughened}}$	$\mathbf{S_{roughened}}$
near-field	0.03 %	99.7 %	0.027 %	0.6 %	90 %	9.4 %
far-field	0.01 %	98.7 %	1.29 %	0.35 %	89 %	10.65 %

The field pattern for the same structure but for the frequency between the first two band gaps (40 GHz) is shown in Fig. 2.34. In the case of zero roughness the transmission and reflection are 98% and 1.5% for near field and 94% and 1.3% for far-field, respectively, whereas in the roughened PhC they are 70% and 29% for near-field and 53.9% and 15.4% for far-field (see Table 2.3). Although the wavelength is larger than in the previous case the effect of the surface roughness is much more pronounced. We believe that the reason is that in the center of a band gap the wave penetrates only for the first few layers and thus encounters less scattering than the transmitted wave. Note, that the reflected wave is not a plane wave since the mechanism of reflection now is backscattering

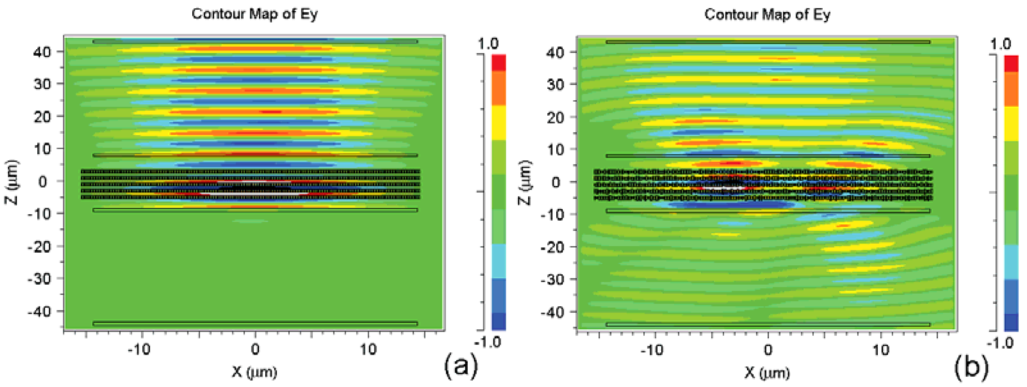

Figure 2.34. The same as in Fig.2.33 but for a frequency of *40 GHz* (*λ=7.5 mm*) which is between the first two band gaps.

from surface features but not interferential suppression as in the case of a gap. This fact explains the striking difference in scattering detected in near- and far-field. In the former case the scattering is S =100% - 29% - 70% =1%. In the far-field the scattering is about 30%.

Thus, in the presence of scattering, for an appropriate comparison of the experimental and theoretical data, the distance from the sample to the monitor has to be taken into account since the farther the detector is away from the sample the less scattered waves will be detected. These “lost” scattered waves are the reason for transmission and reflection not adding up to 100%.

Table 2.3. The same as Table 2.2. but for f = 40 GHz, Fig. 2.34.

	$T_{perfect}$	$R_{perfect}$	$S_{perfect}$	$T_{roughened}$	$R_{roughened}$	$S_{roughened}$
near-field	98 %	1.5 %	0.5 %	70 %	29 %	1 %
far-field	94 %	1.3 %	4.7 %	53.9 %	15.4 %	30.7 %

2.2.6 Conclusions

We have investigated the effect of surface roughness on transmission and reflection in 1D PhC in simulations and experiment. The calculated transmission spectra showed high robustness of the lowest band gap to surface roughness. Even for the roughness with the amplitude as high as 40% of the thickness of high-index layers, the increase of the transmittance within the lowest band gap is negligible in comparison to zero-roughness case.

With increasing frequency (decreasing wavelength) the effect of surface roughness on transmittance becomes more pronounced: the gaps become shallower and narrower; between the gaps the interference fringes smear out and the average transmittance decreases. For the disorder amplitude δ=0.4 the band gaps disappear totally for the frequencies higher than 120 GHz. Empirically, we can formulate two approximate conditions defining the effect of surface roughness:

if $\lambda / n > 10 \cdot l_h \cdot \delta$ then the effect of surface roughness on transmission is small,

if $\lambda / n < 4 \cdot l_h \cdot \delta$ then the scattering of the waves on the surface features becomes very significant and the "reflected" and "transmitted" waves should be rather treated as back-scattered and forward-scattered, respectively.

We have examined the scattering processes in more details by considering an extended model where the transmission and reflection were detected in near-field (subwavelength distance from the PhC) and in far-field. These additional simulations showed that when detection is performed in the near-field the major part of scattered power appears either in transmittance or in reflectance and the sum of the transmittance and reflectance is almost 100%. In the far-field a part of the scattered waves passes by the detectors so that transmittance and reflectance do not add up to 100%. In addition, we have shown that although the transmittance of a PhC with disorder within the second band gap is still very low (0.6%) the reflectance is also sufficiently lower (90% instead of 99.7% for zero-roughness) due to the scattering. In other words, for a rigorous characterization of the effect of surface roughness the reflection and the scattering should be considered in addition to the transmission.

1D PhCs were designed and fabricated for the microwave range. They consisted of five 1.11 mm thick alumina plates separated by air spacings of 1.21 mm. The roughness was created by gluing alumina powder to the both surfaces of each plate. The typical size of a roughness feature was around 6% with respect to the thickness of alumina plates. Such roughness corresponds to typical size of imperfections during the fabrication of 1D PhCs operating at wavelengths in the visible spectral range. Special experiment-oriented simulations were performed in order to account for the decrease of air filling factor after gluing powder. The experimental transmission spectra are found to be in a very good agreement with the calculations. We have shown that the main effect of the glued powder is the redshift of the band gaps due to the decrease of the air filling fraction of the PhC. We did not observe any significant smearing of the first three band gaps due to the roughness.

Due to the scalability of Maxwell's equations one can extend our results to submicron-sized 1D photonic crystals. We believe that the results presented, in particular the empirical formulas discussed above, provide a fast and convenient way to estimate whether imperfections during the fabrication of a submicron 1D PhC will affect its transmission and reflection properties.

2.3. Wave propagation and disorder in 3D colloidal PhC with low refractive index contrast.

2.3.1. Introduction.

Currently, one of the most wide-spread methods for the fabrication of 3D photonic crystals (PhC) for near-infrared and visible light is the self-organization of spherical colloidal microparticles [92, 93, 94, 95, 96, 97, 98, 99, 100, 101, 102, 103, 104, 105]. Due to the process of sedimentation of submicron-sized spheres from a colloidal solution on a flat surface it is possible to fabricate ordered arrays of these spheres with 3D periodicity. Normally, this self-organized sedimentation process leads to the formation of close-packed layers of spheres on top of each other that corresponds to the growth of a fcc structure in [111] direction [92-98]. Such arrangements are commonly called artificial opals. However, there is another, a bit lesser-known, possibility to create 3D periodical colloidal structures. If the colloidal particles are statically charged then due to the long-range repulsive interaction between each other they can form a dilute (i.e. not close-packed) structure with a bcc or fcc lattice, depending on the concentration of the particles [99-103]. Such PhCs exhibit optical properties which are similar to close-packed structures. Iridescence observed in a 3D colloidal PhC with bcc lattice consisting of silica spheres dispersed in ethylene glycol-water mixture is shown in Fig. 2.35. An advantage of PhCs based on charged colloids is, for example, a possibility to change their structure (and consequently their optical properties) by an external influence [103].

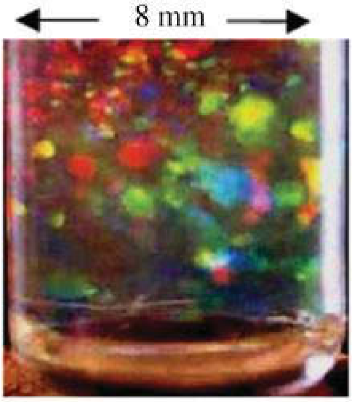

Fig. 2.35. Iridescence from a 3D colloidal PhC with bcc lattice consisting of silica spheres dispersed in ethylene glycol-water mixture under white light illumination. The color spots correspond to single-crystalline domains. Taken from [102]

The main aim of section 2.3 is to investigate theoretically the wave propagation and the influence of disorder on the optical properties of non-close-packed colloidal PhCs with bcc lattice.

In subsection 2.3.2 the models and the calculation methods are described.

In subsection 2.3.3 we illuminate the basic optical properties of non-close-packed colloidal PhCs by examining the band structure and reflection spectra for a bcc lattice of silica spheres in an aqueous medium. Finite size effects and correspondence between the Bragg model, band structure and reflection spectra are discussed. The calculations of the reflectance presented in this chapter are made using the multiple-scattering method since this method allows examining spatially large structures under low consumption of computational resources. The band structure calculations are performed by the PWEM.

In subsection 2.3.4 we present FDTD calculations of reflection spectra of PhCs with disorder. Three types of disorder are examined: disorder in radii, positional disorder and missing-sphere disorder.

By comparison of simulations with the experimental reflection spectra [100,101] we show in section 2.3.5 that the experimental results can be well reproduced by the simulations under the assumption that the fabricated PhCs do not have a perfect bcc lattice but are slightly compressed in [110] direction. This compression is most probably due to the effect of gravity during growth.

2.3.2. Description of the model and calculation methods.

There are two numerical methods which were applied for the calculations of the reflection of a dilute 3D PhC with bcc lattice: the multiple-scattering method (MSM) and the finite-difference time-domain method (FDTD). A big advantage of the MSM is that it allows to calculate transmittance and reflectance for large structures consuming low amount of computational resources. However, MSM is only applicable for perfectly periodic structures. The FDTD method, in contrast, allows consideration of disordered structures being, however, very computationally expensive.

Here we will explore some peculiarities of the application of these methods in the particular case of 3D colloidal PhCs.

a) Input parameters for the MULTEM2 program (MSM)

Our aim is to calculate transmission and reflection for a 3D photonic crystal with bcc lattice for [110] propagation direction.

Fig. 2.36 shows the problem in terms of MULTEM2 [90, 91] parameters. The x and z axes are defined according to the MULTEM2 program geometry. Larger black circles are the spheres lying in the plane of the sketch, smaller black circles denote the spheres lying in the plane located at a distance $a/\sqrt{2}$ behind the plane of the sketch, where a is the lattice constant of the bcc lattice.

The plane wave that propagates in [110] direction (the red arrow in Fig. 2.36) in bcc lattice encounters two "types" of planes of spheres which have the same primitive vectors of their 2D lattice but are shifted with respect to each other. These two planes should be included into the unit slice and the bcc structure is then formed by repeating the unit slice.

The unit cell of 2D lattice of spheres in our case is a rhomb made by two body-centered "atoms" (acute angle vertices of a rhomb) and two atoms from the vertices of a cubic cell of bcc lattice. From simple geometrical calculations we obtain the lengths of primitive vectors of 2D lattices to be equal to $a'_{1,2} = a \cdot \sqrt{3}/2$ and the angle between them is 70.5288°, where a is the lattice constant of the bcc lattice.

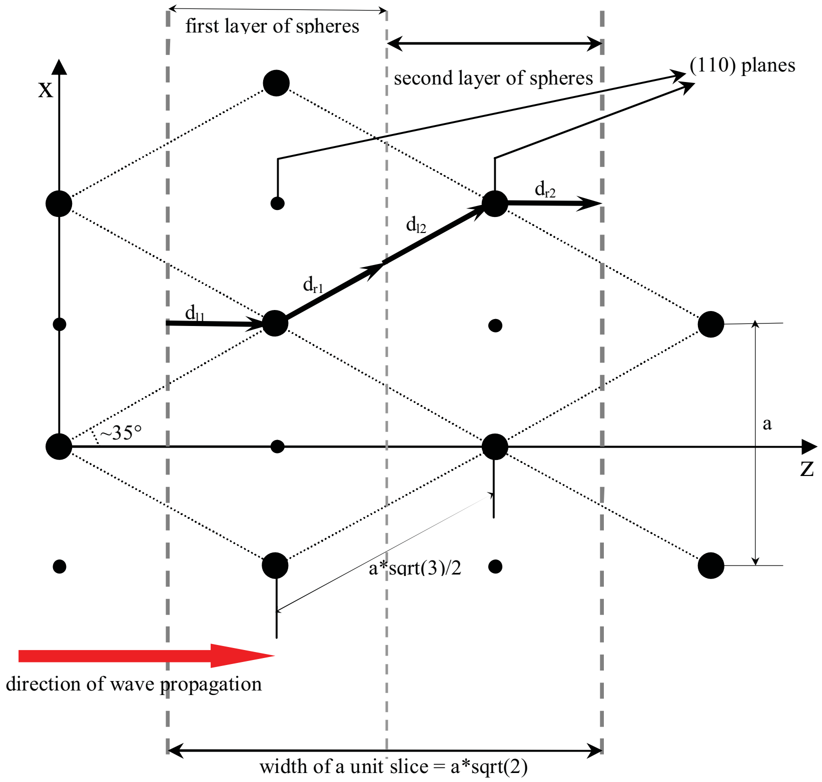

Fig. 2.36. Schematic description of the geometry of the problem in the MULTEM2 program. The direction of the wave propagation which is [110] direction in the bcc lattice is shown by the red arrow. The large black circles depict the spheres lying in the plane of the sketch, the smaller circles denote the spheres lying further behind. The two thicker dashed lines show the unit slice consisting of two layers. The bcc structure is made by repeating the unit slice in the direction of propagation.

Our unit slice consists of two layers of spherical particles as shown in Fig. 2.36. According to the description of MULTEM2 program, the choice of vectors d_l and d_r which define the relative position of the spheres are "to some degree arbitrary" [90]. We have chosen them to have the following coordinates:

$d_{1l}=(0,\ 0,\ \frac{1}{\sqrt{6}})a'$

$d_{1r}=(0, \frac{1}{2\sqrt{3}}, \frac{1}{\sqrt{6}})\ a'$

$d_{2l}=(0, \frac{1}{2\sqrt{3}}, \frac{1}{\sqrt{6}})\ a'$

$d_{2r}=(0,\ 0,\ \frac{1}{\sqrt{6}})a'$

It is important to remember, that all distances in program are given in units of the primitive vectors of 2D lattice of spheres but not in units of the bcc lattice constant, i.e. in units of a' but not *a*.

The input file "fort.10" which was used in the calculations is given in the APPENDIX III.

b) Using FDTD method for 3D colloidal photonic crystals.

The FDTD method solves the Maxwell's equations directly in real space by replacing spatial and time derivatives of the field by finite differences, in other words *dx*, *dy*, *dz*, and *dt* are replaced by Δx, Δy, Δz, and Δt, respectively. Thus, the spatial computational area is divided into small cells of size $\Delta x*\Delta y*\Delta z$. The main requirement to this cell is that it should be at least 10 times smaller than the characteristic features size (in our case the spheres) and the wavelength. This requirement is the main limitation of the FDTD since spatially large problems (especially in 3D) consume a very large amount of computational resources. Due to this limitation in the calculations presented below the PhC structures consist of 70 (110) planes.

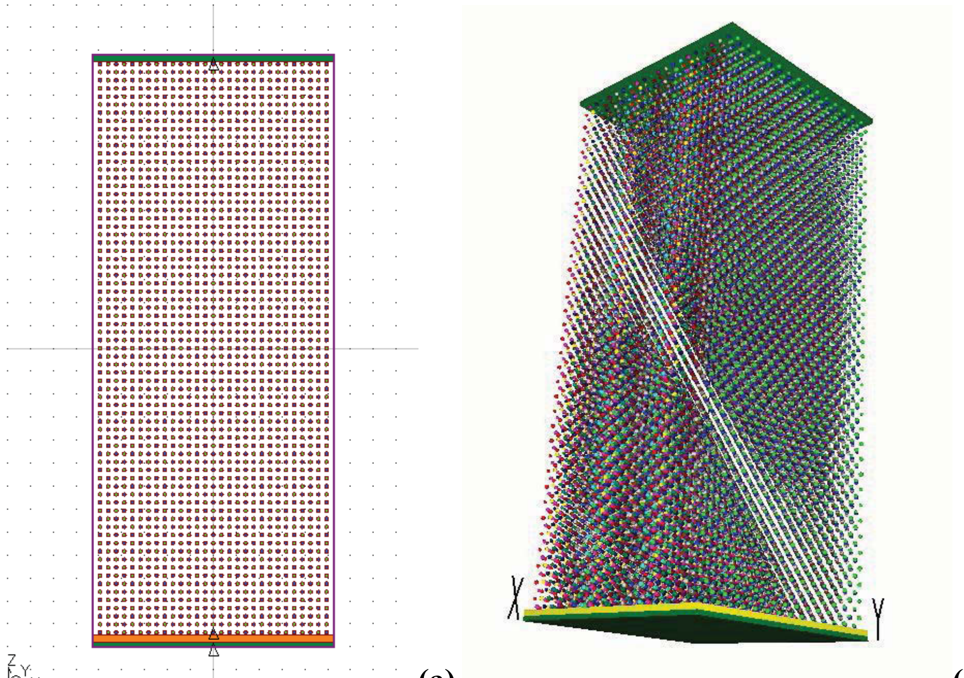

(a) **(b)**

Fig. 2.37. General view of the problem (without disorder) in (a) 2D, xz cross-section and (b) 3D. The structure consists of 70 (110) planes in z direction.

In Fig. 2.37 the general view of the problem (without disorder) is depicted for *xz* cross-section (a) and full 3D view (b). The horizontal green bars in Fig. 2.37a are the monitors which record the flux of electromagnetic (EM) energy through them. The monitor at the top records the transmitted power, the one at the bottom the reflected power. The horizontal orange bar is the source radiating only towards the PhC. The electric field in incident wave is polarized along the y-direction ([001] crystallographic direction). The effect of different polarization (x-direction, [-100]) on the results presented below is insignificant. The propagation direction (*z*) corresponds to the [110] direction in the bcc lattice. The purple frame shows the edge of the computational domain with perfectly matched layer (PML) absorbing boundary conditions (ABC). There are two main points which force us to choose PML ABC instead of periodic boundary conditions: (i) since we will introduce random disorder below, the translational symmetry of the structure is broken that can result in some non-physical effects on the edges of the computational domain if using the periodic boundary conditions; (ii) PML ABC allow to account for scattering processes since the scattered (in x- and y- directions) electromagnetic energy will be absorbed by the PML and thus will not appear either in transmission or in reflection.

2.3.3. Basic properties of diluted colloidal photonic crystals with bcc lattice

Let us consider a 3D photonic crystal with the following parameters: n_b=1.33, n_{sph}=1.46, r=0.18a, lattice type is bcc, where r is the radius of the spheres, a is the lattice constant of the bcc lattice, n_b and n_{sph} are the refractive indices of the background (aqueous medium) and of the spheres, respectively.

In Fig. 2.38 the photonic band structure calculated by the plane-wave expansion method (PWEM) for the 8 lowest bands is shown. Due to the very low refractive index contrast the structure does not exhibit a full photonic band gap. However, there is a narrow gap at the N point ([110] direction), shown enlarged in the inset. This unidirectional gap corresponds to the first-order Bragg reflection from the system of (110) planes.

Actually, in the case of [110] incidence, the 3D structure considered can be treated as an array of parallel partially reflecting planes or, in photonic crystal terms, as a 1D structure. Let us check the correspondence between full 3D consideration and simplified Bragg reflection model. The wavelength of the first-order Bragg reflection peak is given by

$$\lambda_B = 2d \cdot n_{eff} \cdot \cos\theta \tag{2.4}$$

where $d = a/\sqrt{2}$ is the distance between two adjacent planes, n_{eff} is an effective refractive index and θ is the angle of incidence. The effective refractive index can be calculated by using the well-known Maxwell-Garnett approximation:

$$n_{eff}^2 = \varepsilon_{eff} = \varepsilon_b \frac{(1+2f)\varepsilon_{sph} + 2(1-f)\varepsilon_b}{(1-f)\varepsilon_{sph} + (2+f)\varepsilon_b}, \tag{2.5}$$

where f is the volume filling fraction of the spheres. By substituting f=0.0488, that corresponds to r=0.18a (see subsection 2.3.5 for details of calculation), we obtain the value of n_{eff}=1.336. The frequency of the first-order Bragg reflection peak calculated by Eq. (2.4) for normal incidence (θ=0) is then a/λ_B=0.5293. The center frequency of the band gap calculated by the PWEM and shown in the inset of Fig. 2.38 is a/λ_B=0.5291. Thus, the agreement with the center frequency of the reflection peak is very good.

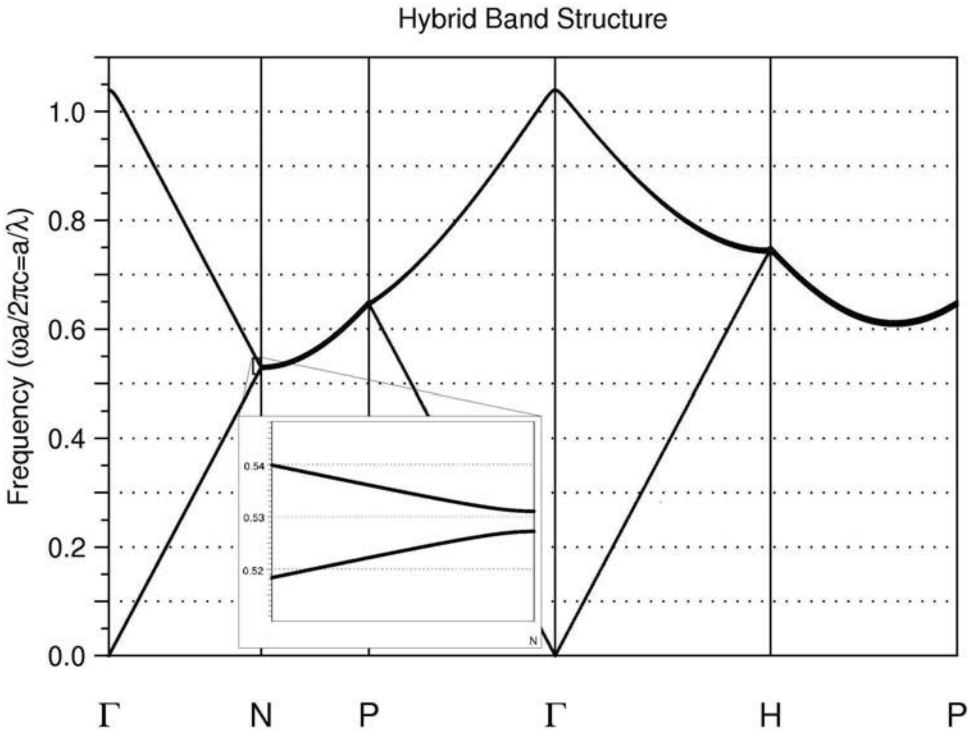

Fig. 2.38. Band structure of a 3D photonic crystal with the following parameters: bcc lattice, ε_b=1.33, ε_{sph}=1.46, r=0.18a. Inset shows the pseudogap at the N-point

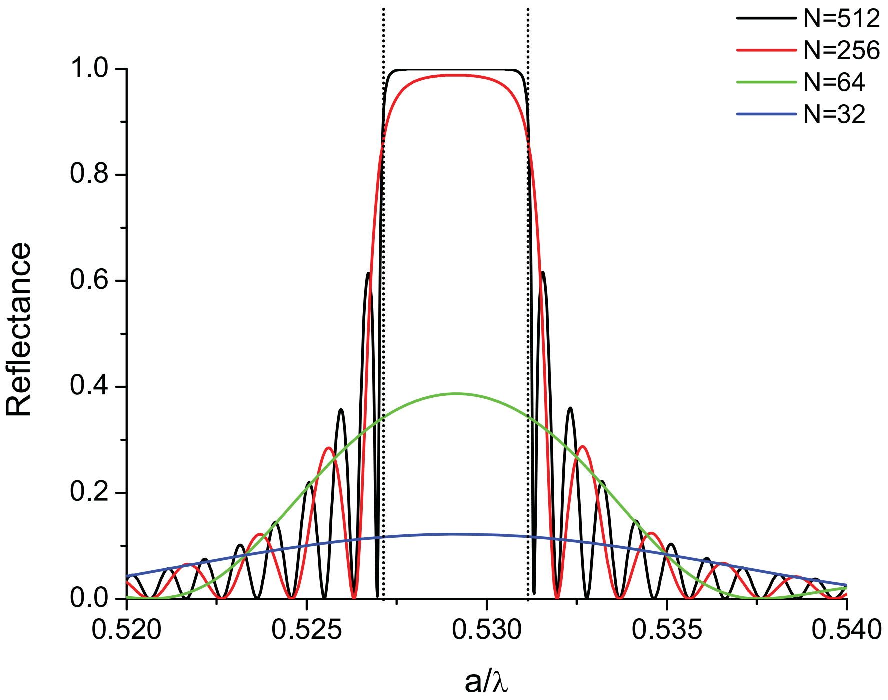

Fig. 2.39. Reflection peak calculated by MSM for [110] propagation direction in bcc lattice for a PhC with n_b=1.33, n_{sph}=1.46, r=0.18a. N is the number of (110) planes. Vertical dotted lines show the edges of the band gap calculated by the PWEM. The side oscillations are Fabry-Perot interference fringes.

The reflection calculated by using the MULTEM2 program [90, 91] is presented in Fig. 2.39. Different line colors correspond to different thicknesses of the PhC in [110] direction. *N* is the number of the (110) planes; vertical dotted lines show the edges of the pseudogap calculated by PWEM (Fig. 2.38). One can see a pronounced effect of the finite size of the PhC: if the number of (110) planes is small the reflection peak is broad and the value of the peak maximum is small; with the increase of the thickness of the structure the peak maximum increases and reaches unity. This is easily understandable: since the contrast in refractive index between spheres and background is very weak, a large number of layers are required to suppress the incident wave, thus the wave penetrates deeply into the PhC before all of it is reflected. Fig. 2.39 also shows that the reflection peak coincides with the gap at the N-point of the photonic band structure is the number of (110) planes is large enough. Since the band structure calculations made by PWEM assume a PhC that is infinite in all directions we can state that for the current parameters in the MSM calculation 500 layers of spheres represent the reflectance of an infinite structure. Of course, PhCs with higher optical contrast and close-packed structure require fewer layers to fully develop the reflected wave [13, 14]. An interesting point is that the simplest Eq. (2.4) gives already a sufficiently exact value of the center of the reflection peak; band structure calculations allow to derive also the width of the reflection peak of an infinite structure; however, the shape of the reflection peak and the actual value of its maximum can be obtained only by real-space calculations (e.g. MSM, FDTD).

It is necessary to note that experimentally fabricated bulk colloidal PhC usually have multi-domain structure [96-103]. This means that they contain monocrystalline domains which are differently oriented with respect to each other. According to our estimations of the finite-size effects we can state that these domains should be large enough (several hundreds of (110) planes) in order to exhibit strong reflection peaks.

We consider now the behavior of the reflection peak when the parameters of the calculations are varying slightly from that used in Fig. 2.39. The positions of the reflectance peak for different refractive indices of the background are shown in Fig. 2.40. The black curve is for the same parameters as the black curve in Fig. 2.39. Typical PhC effects are observed in Fig. 2.40.: the reflection peak shifts to higher frequencies as the effective refractive index decreases; at the same time, the width of the peak depends on the refractive index contrast being lower for lower contrast (see, for example, the green curve). The spectral positions of the central frequencies of the peaks are in very good coincidence with the Bragg peaks calculated by the formula (2.4).

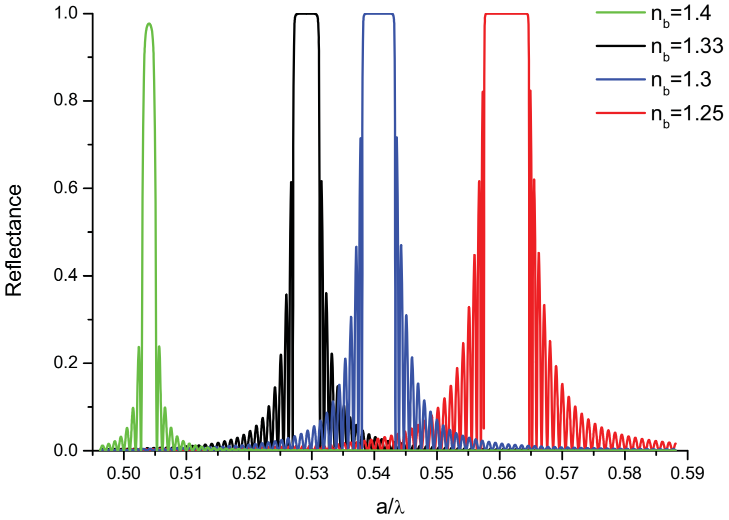

Fig. 2.40. Normal-incidence reflectance spectra for different refractive indices of the background material: n_b=1.4 (green), n_b=1.33 (black), n_b=1.3 (black), n_b=1.4 (red). The fixed parameters of the PhC are n_{sph}=1.46, r=0.18a.

Let us now consider the dependence of the reflectance spectra on the radii of the spheres. The fixed parameters are the refractive indices of the background n_b=1.33 and of the spheres n_{sph}=1.46. In Fig. 2.41 the spectra for r=0.14a (green), r=0.16a (red), r=0.18a (black), r=0.22a (blue) are shown. We observe an increase of the reflection peak width as well as small redshift of the spectral position of the peak with increasing radius. The spectral positions of the peaks are again very well described by the Bragg model (2.4).

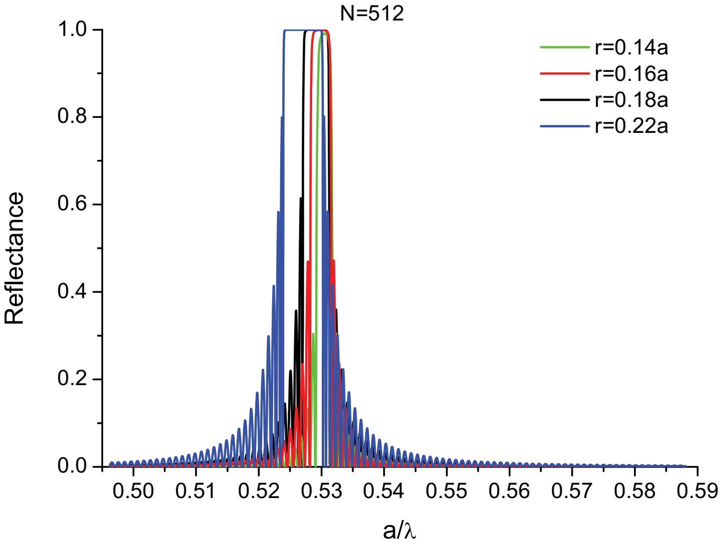

Fig. 2.41. Normal-incidence reflectance spectra for different refractive indices of the background material: n_b=1.4 (green), n_b=1.33 (black), n_b=1.3 (black), n_b=1.4 (red). The fixed parameters of the PhC are n_{sph}=1.46, r=0.18a.

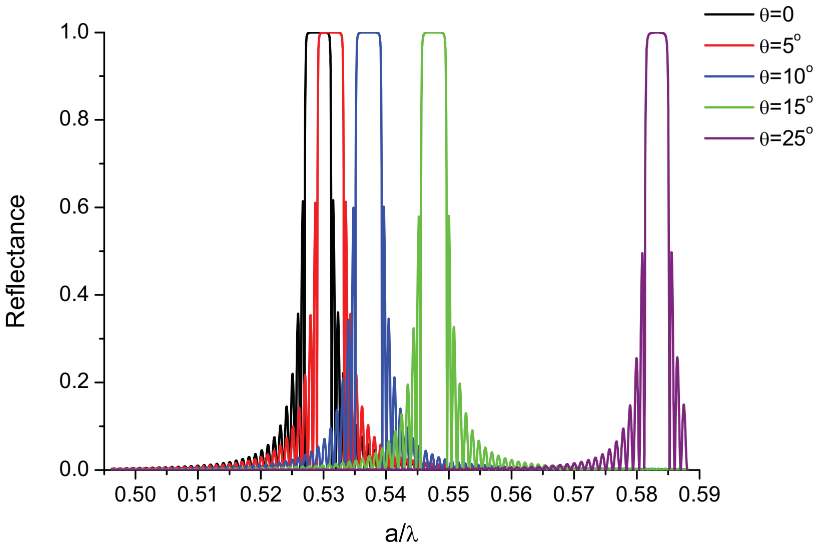

Fig. 2.42. Reflectance spectra for various angles of incidence. The fixed parameters are n_b=1.33, n_{sph}=1.46, r=0.18a and the angles of incidence are θ=0° (black), θ=5 ° (red), θ=10° (blue), θ=15° (green), and θ=25° (purple).

The spectra for different angles of incidence θ are shown in Fig. 2.42. The fixed parameters now are n_b=1.33, n_{sph}=1.46, r=0.18a (the same as in Fig. 2.39) and the incidence angle is varied from zero to 25 degrees according to the figure caption. The dependence of the peak position on the incident angle is responsible for the well-known iridescence (see Fig. 2.36) effect which is observed in colloidal PhC as well as in some natural materials like the wings of some insects or minerals. It is worth to note that the positions of the centers of the peaks are again described very well by the Bragg condition (2.4). The width of the reflection peaks are practically the same for all curves.

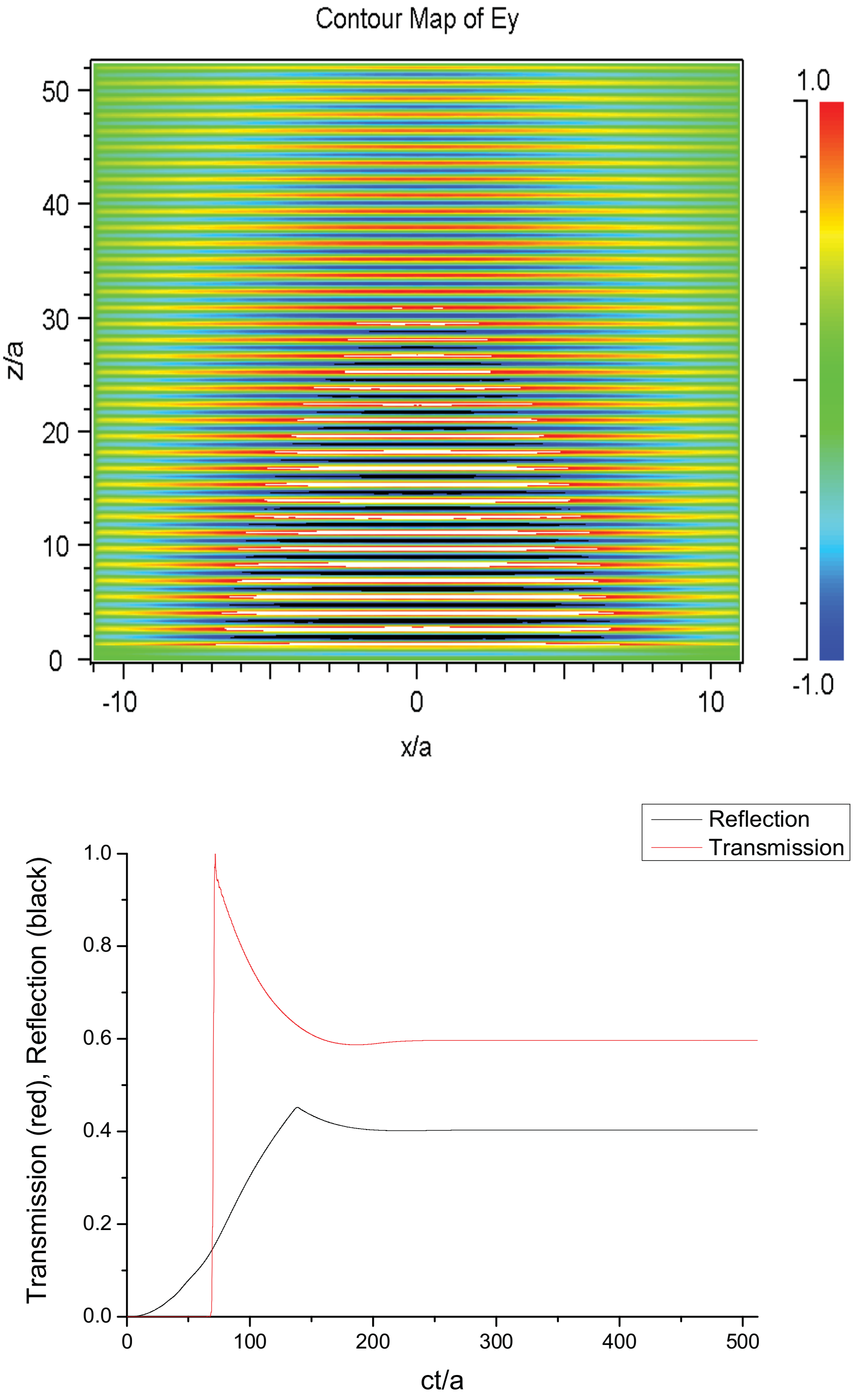

(a)

(b)

Fig. 2.43. FDTD simulation of the EM wave propagation in [110] direction of a 3D PhC with bcc lattice. (a) The distribution of E_y field component inside a 3D photonic crystal with the same parameters as in Fig. 2.39 (spheres are not shown). The color scale is normalized to the field amplitudes of the wave generated by the source. The white and the black colors correspond to the field amplitudes which are above 1 and below -1, respectively. The scales of z- and x-axes are given in units of bcc lattice constant. b) The time-dependent transmittance and reflectance. The time is given in units of *a/c*.

As it is said above, the reflected wave develops over a large number of periods in propagation direction. This is illustrated in Fig. 2.43a showing the xz cross-section of the computational domain with the distribution of the E_y component of the electric field for the wavelength corresponding to the maximum of the reflection peak. The plane wave source is located at z/a=0.5. The PhC is located between z/a=1 and z/a=50.5. As a result of interference between the reflected waves with the waves propagating forward, the amplitudes of the field in the bottom part (between z/a=0.5 and z/a~30) are higher than in the generated wave.

In Fig. 2.43b the time-dependent transmission and reflection calculated at the wavelength of the reflection maximum are shown. As one can see, the system reaches a steady state after $ct=250a$.

Since there are no absorptive materials and we are using PML ABC in our calculations we can estimate the scattering by the simple formula $S=1-T-R$, where T is the transmittance and R is the reflectance and S is scattered power. The latter is therefore defined as the power impinging the absorptive side walls (in x- and y-directions) of the computational domain. For the case of the photonic crystal without disorder (Fig. 2.43b) S is 0.0007 relative to the incident power.

2.3.4. Simulation of the influence of disorder

Three types of disorder are considered: disorder in radii, positional disorder and missing-spheres disorder. Disorder in radii is introduced by a random change of the radius of each sphere. In Fig. 2.44a the solid black curve corresponds to the reflection of the perfect structure (without disorder), blue and red dotted curves are for disorder with maximum change in radii of 20% and 40% with respect to initial radii, respectively. We can state that for the given parameters of the PhC the disorder in radii has no effect on the reflection peak for 20% disorder and causes a peak reduction of only about 10% for 40% disorder.

Positional disorder is simulated by introducing random variations in the x, y and z coordinates of the center of each sphere. In Fig. 2.44b the black solid curve is for the case without disorder, blue dotted line for disorder with amplitude $0.2a$ but only in x and y directions, and red dotted line is for disorder with amplitude $0.2a$ in all three directions. As one can see, the amplitude and FWHM of the peak are practically not affected if the spheres are displaced in the xy plane only. This is easy to understand considering that in this case all the spheres still stay within (110) planes. The situation changes when the spheres are displaced out of (110) planes (red dotted line). Then, the peak maximum value is more than two times lower now.

In order to simulate possible vacancies (missing spheres) we have randomly removed 20% of the spheres. In Fig. 2.44c the dotted curve shows the reflection peak for this type of disorder. A clearly visible decrease of the reflection peak maximum is observed in this case. It is necessary to note, that the model for the missing-spheres disorder is idealized. In a real structure, the spheres adjacent to a vacancy would be shifted due to missing repulsive force.

The scattering (S, as defined above) is considerable only for red dotted curves in Figs. 2.44a and 2.44b: 0.063 and 0.061, respectively. In all other cases with disorder it was less than *0.01*. However, one should take into account that the transmittance and reflectance are calculated in near-field. In far-field the amount of scattered energy should be higher.

Interestingly, in all the cases we did not observe any broadening of the reflection peak due to the disorder but only the maximal value was affected.

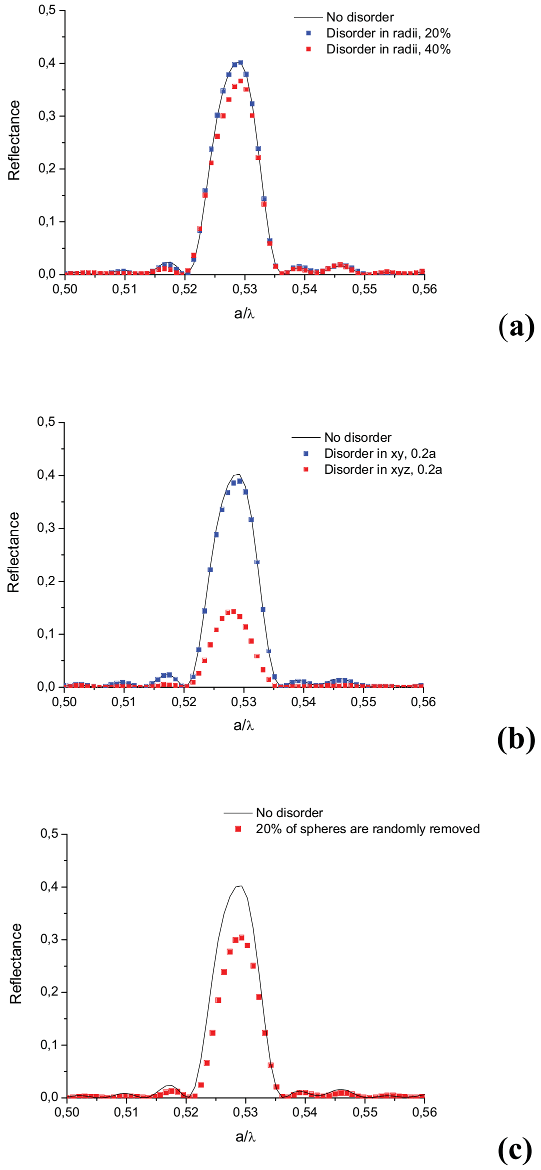

Fig. 2.44. Reflectance curves calculated by 3D FDTD method for disorder in radii (a), positional disorder (b), and missing-spheres disorder (c). More detailed description is in text.

2.3.5 Comparison with experimental data

In the experimental works [100, 101] PhCs with the following nominal parameters were fabricated: n_b=1.35, n_{sph}=1.42, f=0.035, r=55 nm, where f is the fraction of the volume occupied by the spheres and r is the radius of the spheres. Taking into account that there are two atoms per unit cell in the bcc lattice we can extract the lattice constant as

$$a = r \cdot \sqrt[3]{\frac{8\pi}{3 \cdot f}}. \tag{2.6}$$

For f=0.035 we obtain a=341.5 nm (the distance between two (110) planes is d=241.5 nm), so r=0.161a. The reflectance spectra for these new parameters are shown in Fig. 2.45. We should note that in comparison to Fig. 2.39 the reflection peak is sufficiently narrower now. Additionally the number of (110) planes of N=512 is not sufficient to reach an "infinitely large structure" limit. In order to achieve 100% reflection on the maximum of the peak at least 1000 (110) planes should be considered.

By inserting the values of dielectric constants and spheres filling fraction into Eq. (2.5) we obtain the effective refractive index of n_{eff}=1.352. Thus, from the Eq. (2.4) the wavelength of the reflection peak is λ_B=652.9 nm. The wavelength of the reflectance peak shown in Fig. 2.45 is 653.0 nm which is again in very good agreement with the Bragg model, Eq. (2.4). However, this value does not coincide with that one obtained experimentally. In the experiments [100, 101] the reflection peak was detected at the wavelength λ_B=616 nm. We assume that the reason of this discrepancy is that the lattice in the charged colloidal PhC is not perfectly bcc, but slightly compressed in z-direction, so the distance between (110) planes is smaller than should be in a perfect bcc. It is easy to calculate that the reflection peak at λ=616 nm corresponds to a plane-to-plane distance of 227.7 nm (instead of the nominal value of 241.5 nm). This reduction of the plane-to-plane distance can be attributed to the effect of gravity during the growth.

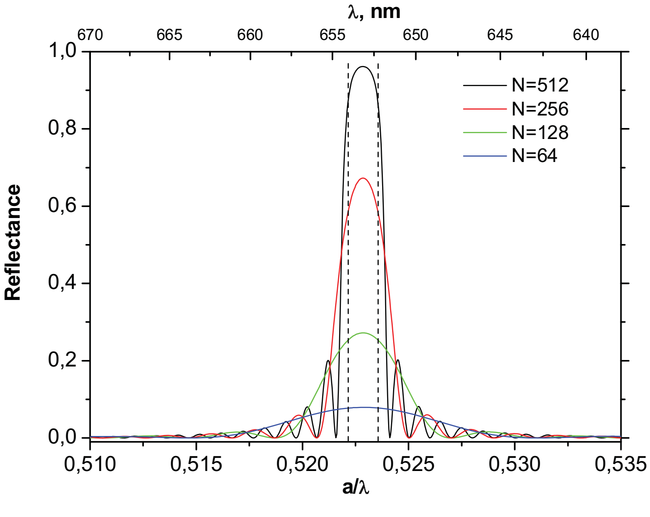

Fig. 2.45. Reflectance peak calculated by MSM for [110] propagation direction in bcc lattice for a PhC with n_b=1.35, n_{sph}=1.42, r=0.16a. N is the number of (110) planes. Vertical dotted lines show the edges of the band gap calculated by the PWEM.

2.3.6. Conclusions

In section 2.3 we have investigated the wave propagation as well as the effects of disorder in 3D colloidal PhC with a bcc lattice. The PhCs considered here have low refractive index contrast (silica spheres in aqueous medium) and low filling factors of the spheres (f~4%).

We have shown that the simple Bragg formula (2.4) can be used to define the spectral position of the lowest reflection peak. However, the shape of the peak as well as the maximum value depend on the thickness of the structure in the propagation direction. From the experimental point of view our results show that fabricated structures should contain sufficiently large monocrystalline domains in order to exhibit strong reflection peaks.

The effect of disorder on the reflection peak was investigated theoretically for normal incidence (propagation direction is [110]). In the case of disorder in radii only a high amount (40% and more) has a visible effect on the reflection peak. Positional disorder decreases the maximal value of the peak only if the spheres are randomly shifted out of the (110) planes. Random removal of 20% of silica spheres from the structure results in a clearly visible decrease of the maximum of the reflection peak. We did not observe any broadening of the reflection peak as effect of disorder but only the maximal value is reduced. The experimentally obtained spectral position of the reflection peak deviates from the calculated one by 6%. We interpret this discrepancy by a deviation from a perfect bcc lattice, viz. that a compression in [110] direction occurs during the growth of the colloidal PhC.

Chapter 3. Extraordinary optical transmission and resonant polarization conversion in photonic crystal slabs covered with metal

3.1. Background

3.1.1. Introduction to EOT

The past two decades gave birth to several new branches of optics expanding the understanding of light-matter interaction processes. Photonic crystals, materials with negative refraction, cavities with extremely high Q-factors and subwavelength mode volume – these are only few cases of experimentally realized novel optical systems. Another example which demanded new theories to explain an experimentally observed effect is the so-called extraordinary optical transmission [106-122]. In the pioneer work of Ebessen et. al. [106] an unexpectedly high transmittance through holes in a metal plate was observed at wavelengths about 10 times larger than the diameter of the holes. A typical transmission spectrum reported in [106] is shown in Fig. 3.1. The transmittance through sub-wavelength holes in an opaque film can be characterized by the so-called *transmission efficiency* which is defined as

$$\eta = \frac{T}{f_p}, \tag{3.1}$$

where T is the transmittance and f_p is the fraction of the surface which is covered by pores. It is implied here that the rest of the surface is covered by an opaque material. The absolute transmittance at the peak located at λ=1370 nm (Fig. 3.1) is approximately 4.4 %. The fraction of the surface which is covered by the pores is $f_p = 100\% * \pi d^2 / 4a_0^2 = 2.2$ %. That means that the transmission efficiency of the peak is η=2. In other words, twice as much light is transmitted as is incident directly on the area covered by the holes. Phenomena which result in transmission efficiencies higher than 1 are called extraordinary optical transmission (EOT).

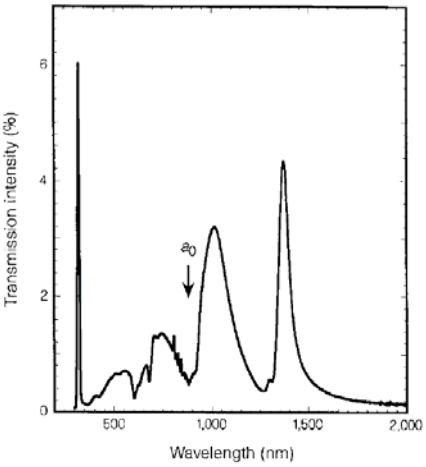

Fig. 3.1. Zero-order experimental transmission spectrum through Ag plate with square lattice of holes on a SiO_2 substrate. The period of the lattice a_0=900 nm, the diameter of the pores d=150 nm, the thickness of the plate t=200 nm. Taken from [106].

The EOT effect was confirmed by a large number of theoretical and experimental papers for the metal hole arrays with various periods, shapes and sizes of the holes, metallic materials as well as for different spectral regions ranging from microwaves to near-IR [107-122].

Initially the EOT was attributed to the excitation of the surface plasmons (SP) [106, 107, 108]. It was supposed that an incident wave couples to surface plasmons on the top surface, tunnels through the hole, couples to the SPs on the other interface and then couples to an outgoing radiative mode [108].

However, it was shown later that the EOT effect appears also in systems which cannot support SPs. In particular, in [109] similar transmission spectra were obtained using the perfect conductor approximation (conductivity is infinitely large). In [110] the EOT was observed in non-metallic structures that is in direct contradiction with the SP-based model. It is worth to note that the EOT was also observed experimentally for non-periodic hole arrays in the microwave region where the metals are almost perfect conductors [111, 112, 113] and cannot support SPs.

Currently (end of 2010) the physical explanation of the EOT effect is still under discussion. Part of the scientific community keeps arguing for the SP nature of the EOT [114, 115, 116, 117, 118]. In contrast, a number of different theories were presented to explain the effect without SPs, including "dynamic diffraction" [119], "composite diffracted evanescent wave" [110], "surface charge resonance" [111], and "impedance matching" [112] models. Recent reviews on extraordinary transmission through metallic holes and slits arrays can be found in [120, 121, 122].

All papers mentioned above consider a metal plate with holes which is located between two homogeneous media. In [123, 124] a metal layer was deposited on top of a GaAs/AlGaAs quantum well infrared photodetector (QWIP) structure. Then a triangular lattice of air holes was etched through the metal and the quantum well stack. The structure was illuminated from above at different angles of incidence. It was shown that photocurrent peaks appear at the wavelengths corresponding to the eigenmodes of the photonic crystal formed by the air holes and the GaAs/AlGaAs layers. It is necessary to note that in QWIPs the electrons can be excited only if the electric field is polarized perpendicularly to the interfaces of the quantum wells. Thus, the authors of [123, 124] were able to map a TM band structure (electric field is polarized parallel to the axes of the pores) of the 2D PhC formed by the quantum well stack and air holes assuming that a photocurrent peaks appear when the lateral component of the wavevector and the frequency of the wave match the wavevector and the frequency of a photonic band. However, the transmittance/reflectance properties of such structures as well as physical mechanisms of coupling of light to PhC remained unexplored. In addition, there was no explanation given why the amplitudes of some photocurrent peaks are orders of magnitude larger than the amplitude of others.

In this Chapter we investigate structures which could be roughly described as a 2D PhC slab covered with a metal layer with corresponding holes. By means of three-dimensional FDTD simulations we were able to record, in addition to transmittance and reflectance, full information about the EM field including: instantaneous 3D distributions of the electric field components, 2D distributions of the electric field amplitudes, vector distributions of electric field and Poynting vectors, as well as average density of the electric field. We will show that PhCs covered with metal exhibit a couple of unusual optical properties, particularly, extraordinary transmission, polarization conversion and localization of light.

3.1.2. Eigenmodes of a 2D PhC with triangular lattice.

As was already mentioned in Chapter 1 the intrinsic properties of a 2D PhC are characterized by the photonic band structure. The photonic band structure shows the eigenfrequencies of the PhC eigenmodes for different values of the quasi-wavevector. The

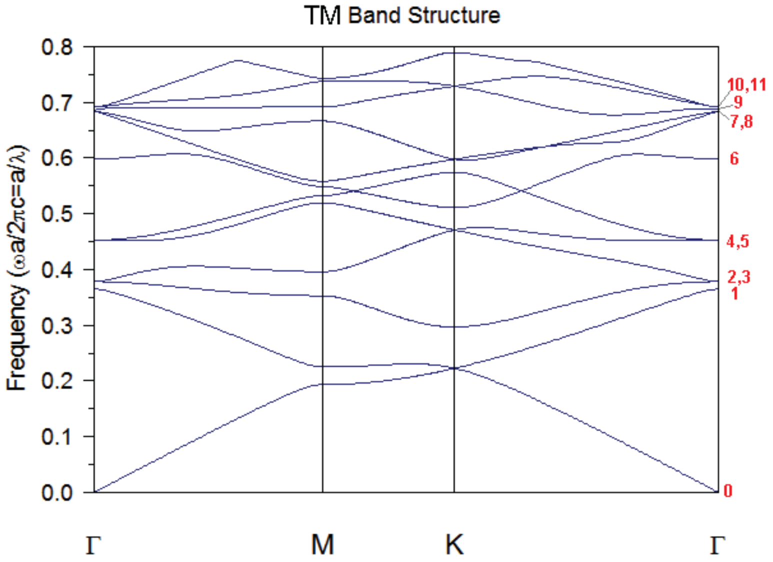

Fig. 3.2. The TM photonic band structure of a 2D PhC consisting of triangular lattice of air pores with r=0.3a in a background material with n_b =3.2. The red numbers on the right side enumerate the modes an the Γ-point: single values are non-degenerate modes, double values – doubly degenerate.

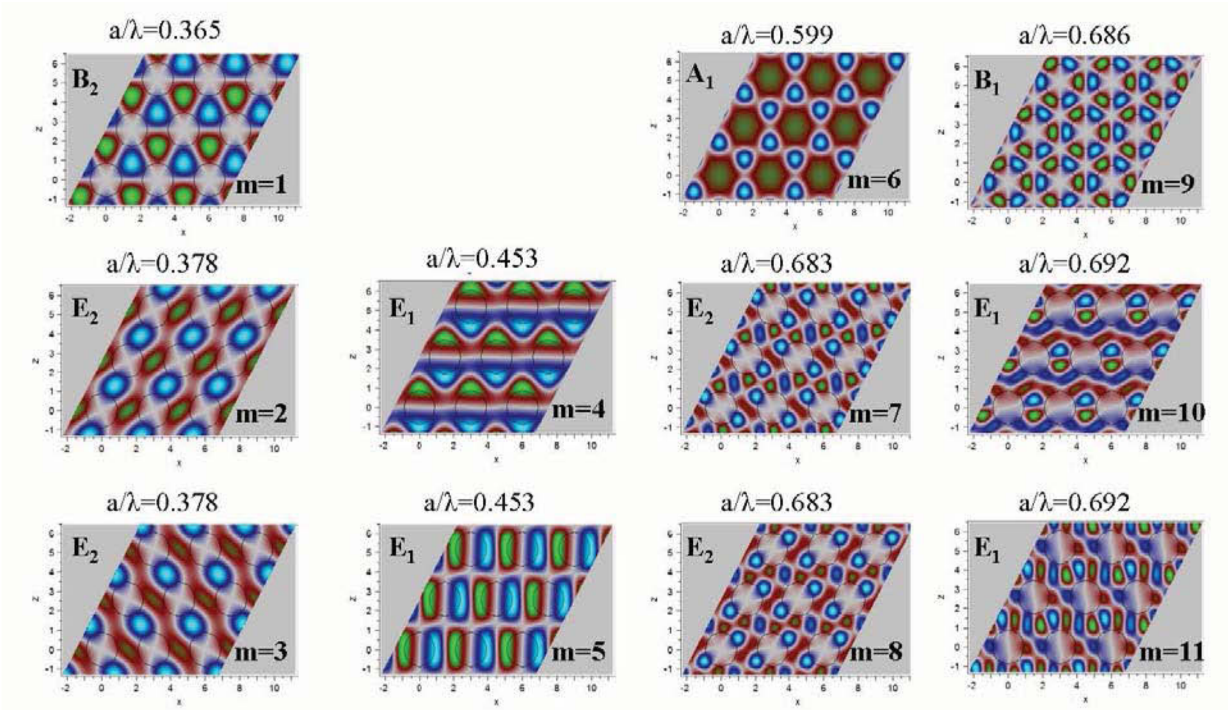

Fig. 3.3. The distribution of the electric field for the eigenmodes at the Γ-point of the band structure shown in Fig. 3.2. The reduced frequency (a/λ), the number (m) and the irreducible representations (A_1, B_1, B_2, E_1, E_2) of each mode are shown. The parameters of the 2D PhC: r=0.3a, n_b=3.2.

TM band structure (E_y, H_x and H_z are non-zero) of a 2D PhC consisting of a triangular lattice of air pores with r=0.3a in a background with n_b=3.2 is shown in Fig. 3.2. The red numbers on the right side enumerate the eigenmodes at the Γ-point; the single values correspond to non-degenerate modes while the values separated by a comma depict doubly degenerate modes. Each eigenmode is characterized by its frequency (which is not unique for degenerate modes) and by the distribution of an EM field (which is unique for each mode). To illustrate this the distributions of E_y component are shown in Fig. 3.3 for the modes from the 1st to the 11th.

The symmetry of the eigenmodes could be estimated from the group theory considerations. The triangular lattice is invariant with respect to the following symmetry operations [2]:

- rotations by the angles of 60 (C_6) , 120 (C_3) , 180 (C_2), 240 (C_3^{-1}), 300 (C_6^{-1}), and 360 degrees
- mirror reflections around x-axis (σ_x, σ_x', σ_x'')
- mirror reflections around y-axis (σ_y, σ_y', σ_y''),

which are shown in Fig. 3.4. Altogether these twelve symmetry operations constitute the so-called C_{6v} point group:

$C_{6v}=\{E, C_6, C_6^{-1}, C_3^{-1}, C_3, C_2, \sigma_x, \sigma_x', \sigma_x'', \sigma_y, \sigma_y', \sigma_y''\}$.

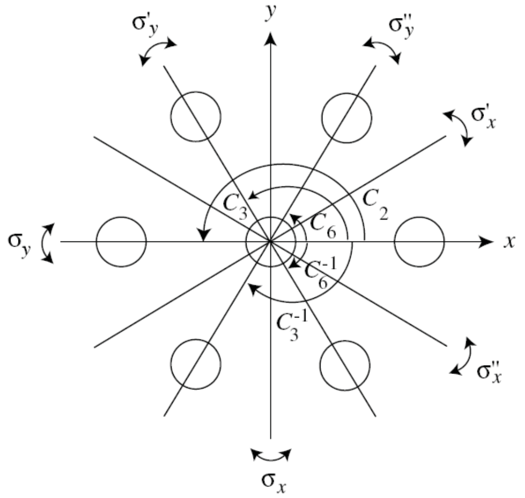

Fig. 3.4. Symmetry operations of the C_{6v} point group. Taken from [2].

According to the group theory, the C_{6v} point group has six irreducible representations which are usually denoted by means of Mulliken symbols: A_1, A_2, B_1, B_2, E_1, E_2. Each irreducible representation has its own spatial symmetry. Symbols A and B denote non-degenerate irreducible representations which are symmetric or antisymmetric with respect to rotation by 60 degrees, respectively. Subscripts "1" and "2" are usually attached to A's and B's which are symmetric or antisymmetric with respect to the horizontal plane of symmetry (in Fig. 3.3: z=0). E corresponds to doubly degenerate representations; the subscripts 1 and 2 of E can be regarded as arbitrary [125].

It can be deduced from the group theory consideration [2] that each eigenmode of a 2D PhC correspond to one of the irreducible representation of the corresponding point group. The irreducible representations for the first three Γ-points (in terms of extended Brillouin zones) are shown in Table 3.1. In extended zone scheme there are six identical $\Gamma^{(2)}$ points and six identical $\Gamma^{(3)}$ which appear as higher-order modes in the reduced zone scheme [2]. As we see from the table, the lowest mode in the Γ-point of the first Brillouin zone (which corresponds to the $\Gamma^{(1)}$) is associated with the A_1 irreducible representation. The next six modes are attributed to two non-degenerate representations (A_1 and B_2) and two doubly degenerate ones (E_1 and E_2).

With the help of group theory we can now designate the modes shown in Fig. 3.3 by corresponding irreducible representations. So, the first mode (m=1) is apparently a B_2 representation since it is non-degenerate and antisymmetric with respect to a 60 degree rotation. In the same way we can conclude that m=6 mode corresponds to A_1 irreducible representation. The pairs m=2,3 and m=7,8 we attribute to the E_2 representation while m=4,5 and m=10,11 to E_1 representation [2]. In this way we have designated the modes from 1 to 11 by corresponding irreducible representations (Fig. 3.3). Of particular interest are the modes corresponding to the E_1 irreducible representation. These modes have a dipole-like spatial symmetry and we will see in section 3.2 that an incident wave couples strongly to these modes if a PhC is covered with a metal layer.

Table 3.1 Irreducible representations for the electromagnetic waves for the Γ-point of the first Brillouin zone of the hexagonal lattice. (After [2])

Symmetry	Point	Irreducible Representations
C_{6v}	$\Gamma^{(1)}$ $\Gamma^{(2)}$ $\Gamma^{(3)}$	A_1 $A_1+B_2+E_1+E_2$ $A_1+B_1+E_1+E_2$

3.1.3. Description of the model.

The tool which is used for the simulations is a commercial software package realizing a full 3D FDTD method (RSoft FullWAVE). By means of this tool it is possible to design directly a structure with actual parameters taken from the experiment.

The simulated structure consists of (from the top to the bottom): a gold layer, a layer of GaAs, a "spacer" layer of $Al_{0.18}Ga_{0.82}As$, an "active region" layer, one more layer of $Al_{0.18}Ga_{0.82}As$, and GaAs substrate. In Table 3.2 the compositions, thicknesses and optical constants of the layers are presented. Such a structure simulates the experimentally fabricated quantum well infrared photodetectors investigated in [123, 124]. In these papers the active region of the QWIPs were consisted of 50 periods of GaAs/AlGaAs quantum wells. In our simulations we treat the active layer as a homogeneous one and we do not take into account the absorption of the photons by electronic transitions in the active layer, thus, the imaginary part of the refractive index of the active layer is assumed to be zero.

The 2D photonic crystal is created by "drilling" pores through the entire structure in the direction perpendicular to the interfaces between the layers. Fig. 3.5a shows the scheme of the investigated structure. A cross-section of the 3D FDTD model taken from FullWAVE CAD window is shown in Fig. 3.5b. A *xz* cross-section of the refractive index profile in the middle of the "active layer" (y=0) is shown in Fig. 3.5c. A xy cross-section of the refractive index profile at *z*=0 is shown in Fig. 3.5d. The 2D photonic lattice has hexagonal (triangular) symmetry in all calculations presented below. The perfectly matched layer (PML) absorbing boundary conditions are used for upper and lower facets (parallel to the *xz* plane) of the computational domain. The other four facets (parallel to *xy* and to *yz* planes) have the periodic boundary conditions. This is a natural choice of boundary conditions for such structure because it allows to simulate both large periodic structure in *xz* plane and transmitted and reflected waves escaping to infinity in y-direction.

As one can see from the Fig. 3.5b the transmission and reflection are detected in the near-field. Unfortunately, it is difficult to perform far-field simulations using the FDTD method since the consumption of the computation resources increases rapidly with an increase of the dimensions of the computational domain.

The plane wave is incident onto the top gold layer normally to the surface, e.g. parallel to the pores axes. For the given geometry this means that the component of the electric E_y is absent in the incident wave.

The described model allows to obtain the following output information: (i) the absolute (normalized to the source) transmitted and reflected power recorded in the near field; (ii) two-dimensional cross-section of the *amplitudes* of the electromagnetic field components (E_x, E_y, E_z, H_x, H_y, H_z); (iii) the instantaneous 3D distribution ("snapshots") of the strength of electromagnetic field components; (iv) the average energy density of the field components within the active region (also excluding the area occupied by the pores); (v) in the present model the absorbance (*A*) can be calculated as $A=1-T-R$. This is possible because the energy dissipated on the computational domain facets with PML (the top and the bottom one) is recorded by either transmission or reflection monitor. The other four facets of the computational domain have periodic boundary conditions, thus the only remaining dissipation source is the absorption by the constituents of the simulated structure.

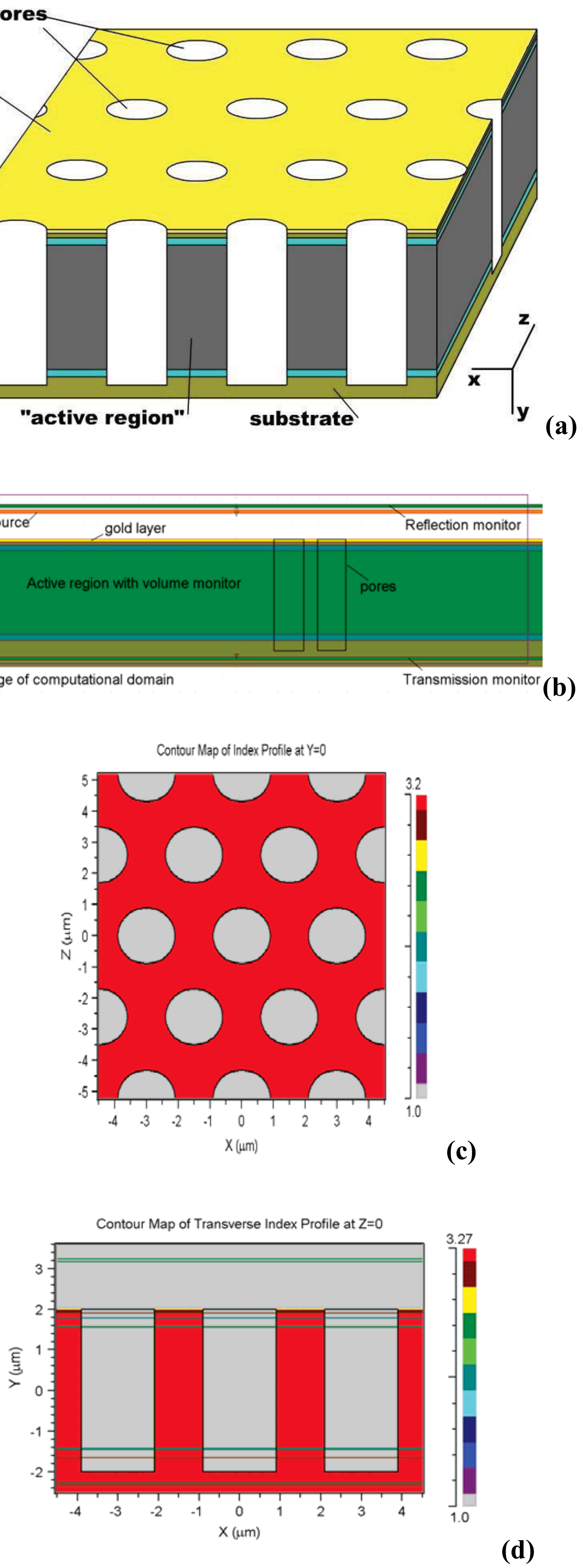

Fig. 3.5. (a): schematic description of the investigated structure. (b): a cross-section of the 3D FDTD model taken from FullWave CAD window. (c): a xz cut of the refractive index profile in the middle of the "active layer" (y=0). d): a xy cross-section of the refractive index profile at z=0.

Table 3.2. Vertical composition of the model structures.

Layer	**Thickness**	**Re(n)**	**Im(n)**
gold	100 nm	n'=3.11	n"=45.3
GaAs	108 nm	n'=3.19	n"=0.0022
$Al_{0.18}Ga_{0.82}As$	216 nm	n'=3.27	n"=0
"active region"	3000 nm	n'=3.2	n"=0
$Al_{0.18}Ga_{0.82}As$	216 nm	n'=3.27	n"=0
GaAs	1000 nm	n'=3.19	n"=0.0022

The estimation of the approximations, limitations and possible inaccuracies:

- The basic limitation which is common for all FDTD simulations is the finite size of a discretization grid cell. Ideally, the size of the discretization grid cell should be infinitely small. This is not achievable in real calculations since this will lead to infinitely large computation time. The main consequence of this limitation is the abrupt change of the refractive index on the interface between two materials is replaced by some transition layer that leads to some change of the geometrical parameters (e.g. radius of the pores) in simulated structure with respect to nominally defined ones. A general way to estimate the inaccuracy caused by an insufficiently fine discretization grid is to test the results for convergence by showing that the results do not change sufficiently if the grid size is decreased.
- The reflectance and transmittance are detected only near the top and bottom of the computational domain, where PML boundary conditions are applied. As a consequence of the periodic boundary conditions, which are applied for four facets parallel to the pores, a wave cannot "escape" through these facets but will reappear in transmittance or reflectance or will be absorbed. So it is difficult to say how a wave "travels" through the structure.
- The source, the transmittance and reflectance monitors are situated at subwavelength distances from the structure. One should remember that in experiment this is usually not the case.
- Since periodic boundary conditions are used in the plane of periodicity of the 2D photonic crystal, the simulation results are strictly true only for structures which are large in *xz* directions.
- The refractive indices of the materials are chosen to have fixed values in the entire examined spectral range. This can lead to some discrepancies in comparison to experiment.

It is necessary to note that typical processor times of a single calculation (for one value of the wavelength of the source) in the 3D model described are 20-90 hours depending on the simulation parameters. Thus, the processor time required to calculate one transmission/reflection spectrum amounts to thousands of hours.

3.2. Simulation results I: photonic crystal slab covered with metal

Let us start with the structure having a layer composition as described in Table 3.2 and with the following PhC parameters: a=3 μm, r=0.3a=0.9 μm and h=4 μm, where a is the period of the PhC, r is the radius of the pores and h is the depth of the pores. The near-field transmittance and reflectance of such a structure for an E_z-polarized plane wave source (i.e. the incident wave has E_z and H_x non-zero components) are shown in Fig. 3.6. We observe at least three pronounced dips in reflectance (and corresponding peaks in transmittance) which will be mentioned below as reflection dips 1, 2 and 3 corresponding to the notations in Fig. 3.6.

It is important to note, that for the given parameters 67% of the surface is covered by a reflecting gold layer and only 33% is occupied by pores. However, the reflectance at λ=6.845 μm (dip 3) is only 0.01 and corresponding transmittance is 0.6 which means that the transmission efficiency, defined as the transmitted power per unit area of the free surface (not covered by gold) is 180%. At the same time, the free-space wavelength is almost 4 times larger than the diameter of the pores and more than two times larger than the period of the hexagonal lattice of air holes.

The information about transmittance, reflectance and absorbance of the three dips is summarized in Table 3.3. It can be seen that in addition to the unexpectedly low reflectance the dips 1 and 3 are characterized by a relatively high absorbance being more than 10 times larger than for the dip 2.

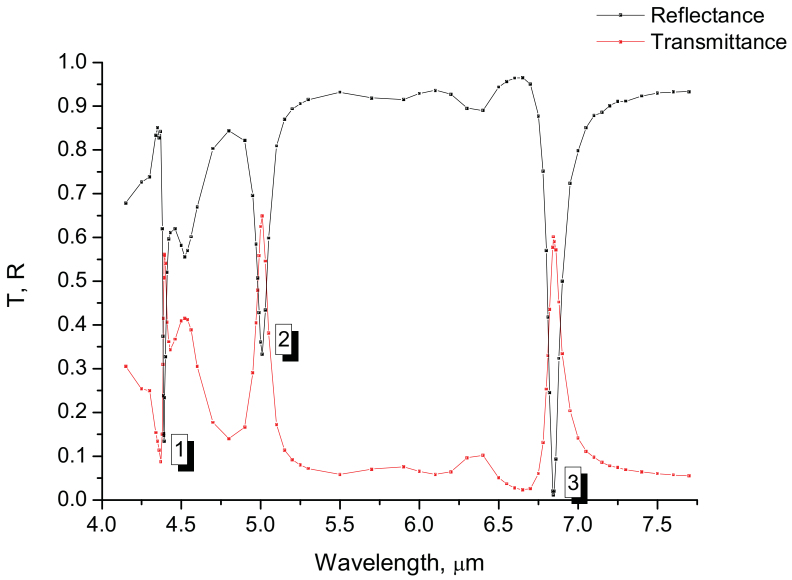

Fig. 3.6 Reflectance (black) and transmittance (red) spectra of a QWIP-like structure with the parameters shown in Table 3.2. The parameters of the 2D PhC are: a= 3 μm, r=0.9 μm, and h=4 μm. The source is E_z-polarized.

Table 3.3. Spectral position, transmittance, reflectance, and absorbance of the dips shown in Fig. 3.6.

	Dip 1	Dip 2	Dip 3
spectral position, μm	4.39	5.01	6.845
R	0.13	0.33	0.01
T	0.56	0.65	0.60
A=1-R-T	0.31	0.02	0.39

In order to understand the nature of the observed spectral features let us consider the distribution of the EM field inside the structure. The xy cross-sections of the distributions of the amplitudes of E_x, E_y and E_z components in steady state are shown in Table 3.4. We choose four different wavelengths to show: 4.39 μm (dip 1), 5.01 μm (dip 2), 6.84 μm (dip 3), and, for comparison, 6.2 μm. The color scale is normalized to the amplitude of the E_z component in the incident plane wave in all the cases, i.e. the amplitude of the E_z field in the generated by the source wave is 1. The white color corresponds to the amplitudes that exceed the maximal value of the scale. The gold layer is located at y=2 μm, the pores extend in vertical direction from y=2 μm to y=-2 μm. The source is located at y=3.2 μm.

First of all, let us consider the E_z field for at λ=6.2 μm (Table 3.4, diagram "l"). This case corresponds to high reflection of approximately 93%, thus the E_z field is concentrated above the gold layer. Between the source and the gold layer the values of the E_z field amplitudes are higher than unity due to the interference between the incident and the reflected waves. The amplitudes of E_y (diagram "h") and E_x (diagram "j") components are very small (but non-zero) within the entire computational domain. It is necessary to note that although the incident wave has no E_y and E_x components they always appear due after diffraction on the edges of the holes in the gold layer.

Let us now turn our attention to the dip 2, λ=5.01 μm. This case corresponds to a transmittance of 65 %, thus the incident wave penetrates through the gold layer that is most clearly seen in the E_z field distribution picture (diagram "f"). The electric field is concentrated mainly within the pores and has amplitudes more than 3 times higher than the incident wave. The amplitudes of the E_y (diagram "e") and E_x (diagram "d") are again non-zero but small within the entire domain.

The most interesting effects are observed for the dip 1, λ=4.385 μm and dip 3, λ=6.84 μm. In both cases the major part of the EM energy is carried by the E_y component which is *absent in the incident wave*! Furthermore, the normalized amplitude of the E_y component is more than 10 for the dip 1 (diagram "b") and more than 5 for the dip 3 (diagram "h"). It should be also noted that the amplitude of the E_y component is maximal just below the gold layer and decreases in the substrate direction.

Thus, the interaction of a linearly polarized incident wave (having only E_z and H_x non-zero field components) with the periodic array of holes in the gold results in the appearance of E_y-polarized mode directly under the gold layer. We will call this effect from now as *polarization conversion*.

Table 3.4. The xy cross-sections of the *amplitudes* of the electric field components at different wavelengths. The color scale is normalized to the amplitude of E_z component in the incident wave. The white color corresponds to the values which exceed the maximum value of the color scale. The source is E_z-polarized.

	Dip 1, λ=4.385 µm	**Dip 2, λ=5.1 µm**	**Dip 3, λ=6.84 µm**	**λ=6.2 µm**
E_x	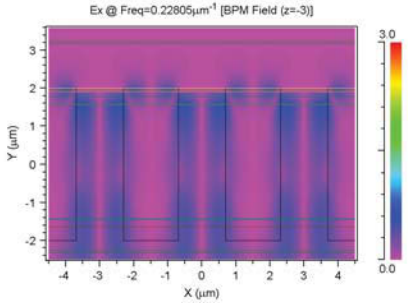 a	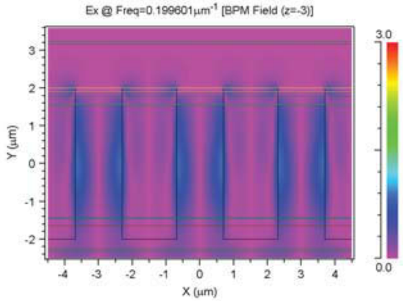 d	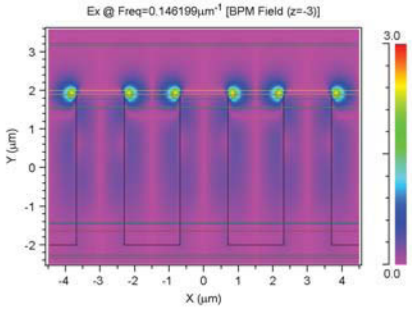 g	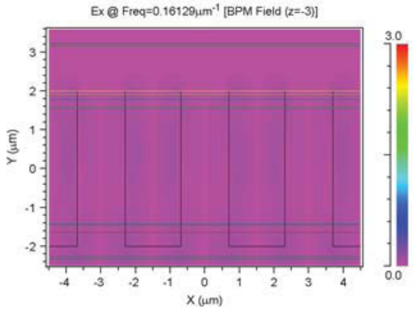 j
E_y	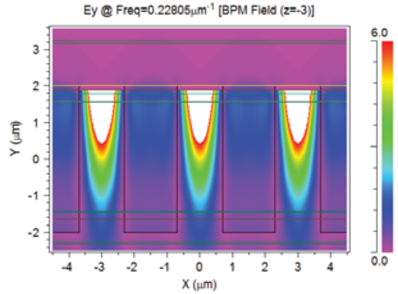 b	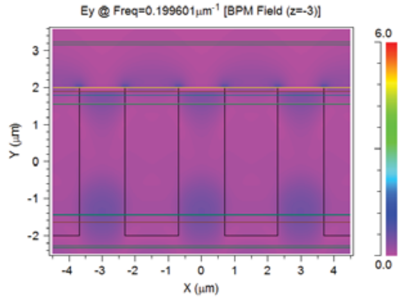 e	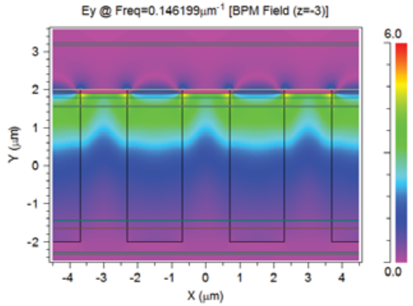 h	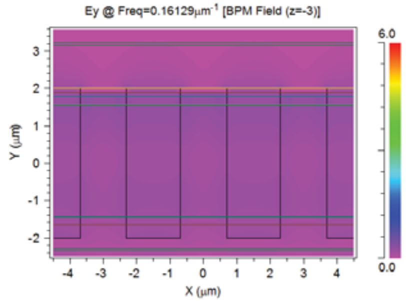 k
E_z	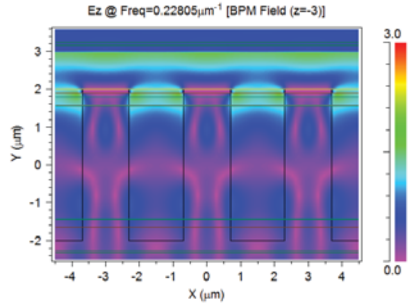 c	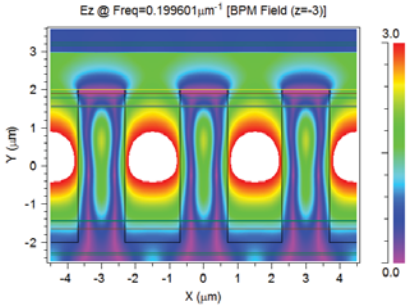 f	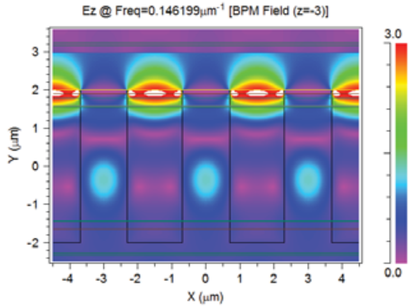 i	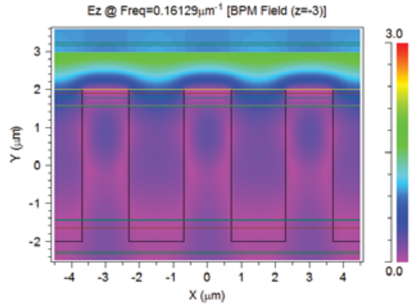 l

3.2.1. The dependence on the polarization of the source.

The reflectance and transmittance shown in Fig. 3.6 was calculated for an E_z polarized source ($E_z \neq 0$, $H_x \neq 0$). The same calculation was also performed with an E_x-polarized source ($E_x \neq 0$, $H_z \neq 0$). The reflectance spectra for the two different source polarizations are combined in Fig. 3.7. One can see that both spectra are practically identical, i.e. the observed spectral features are independent of the polarization of the source. This fact is actually surprising since the triangular lattice is not invariant with respect to a 90 degree rotation.

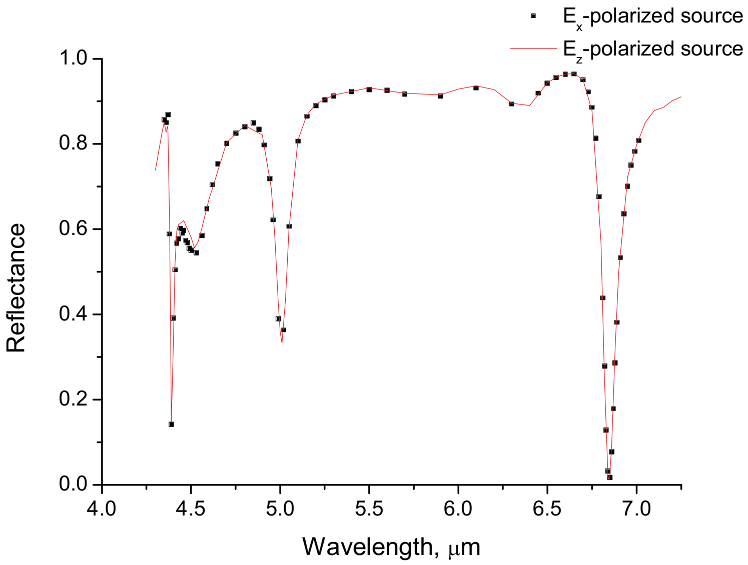

Fig. 3.7. The reflectance spectra of the same structure as in Fig. 3.6 for two polarizations of the incident wave: the black dots are for E_z-polarization; the red curve is for E_x-polarization.

3.4.2. Comparison between 3D FDTD and 2D PWEM.

During a FDTD simulation the information about the field components is saved for each point of the computational domain at each time step. Thus, a 3D distribution of the fields can be easily recorded at each time step. In Fig. 3.8 we show the 3D distribution (top view) of the E_y field recorded within the active region of the structure at the end of simulations. Figs. 3.8a and 3.8b are obtained from dip 1 (λ=4.39 μm) for E_z- and E_x- polarized source, respectively. Figs. 3.8b and 3.8c are for dip 3 (λ=6.84 μm) and for the two polarization of the source. It is necessary to note, that the top surface of the shown field distribution is not directly under the gold layer but approximately 320 nm below it. In this way, we can be sure that a possible effect of the discontinuity of the imaginary part of the refractive index (abrupt change from almost zero in GaAs to 45.3 in Au) on the field distribution is negligible. The horizontal dashed lines in Figs. 3.8a and 3.8c mark the position of the xy cross-sections shown in Table 3.4.

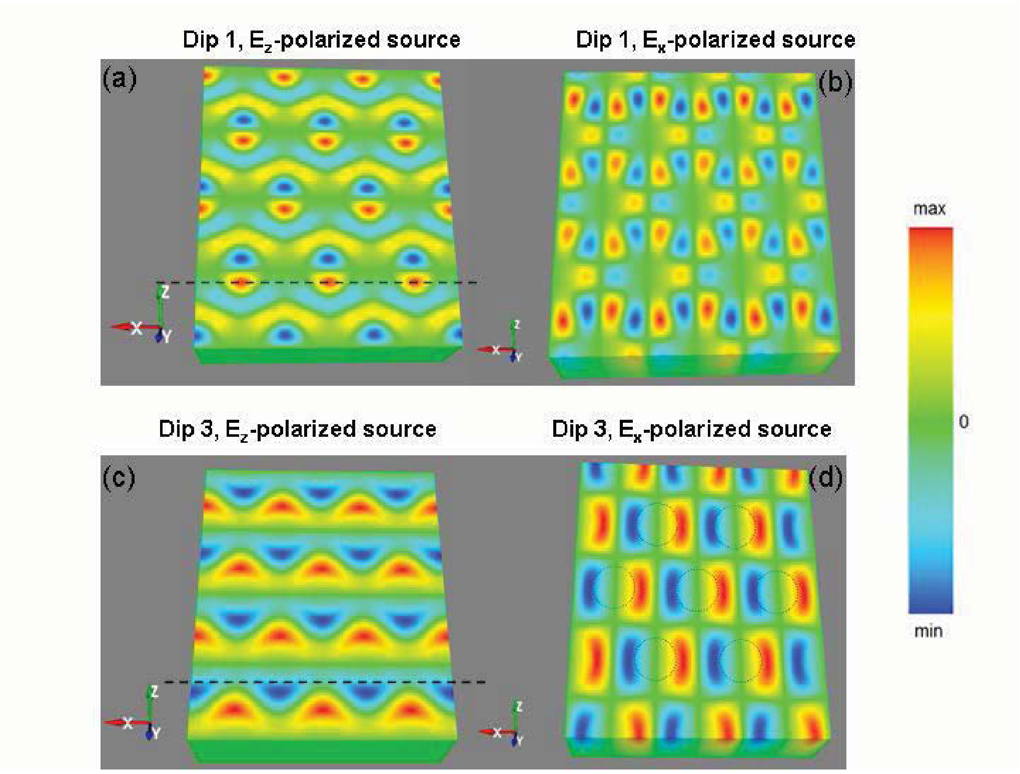

Fig. 3.8. 3D instantaneous distributions of the strength of the E_y component of the electric field. (a) and (b) are taken at the wavelength of λ=4.39 μm (dip 1) for E_z- and E_x-polarized sources, respectively. (c) and (d) are for the dip 3 (λ= 6.84 μm) and two source polarizations. The horizontal dashed lines in (a) and (c) show the positions of the cross sections which are shown in the diagrams "b" and "h" of Table 3.4, respectively. The locations of the pores are shown schematically in (d).

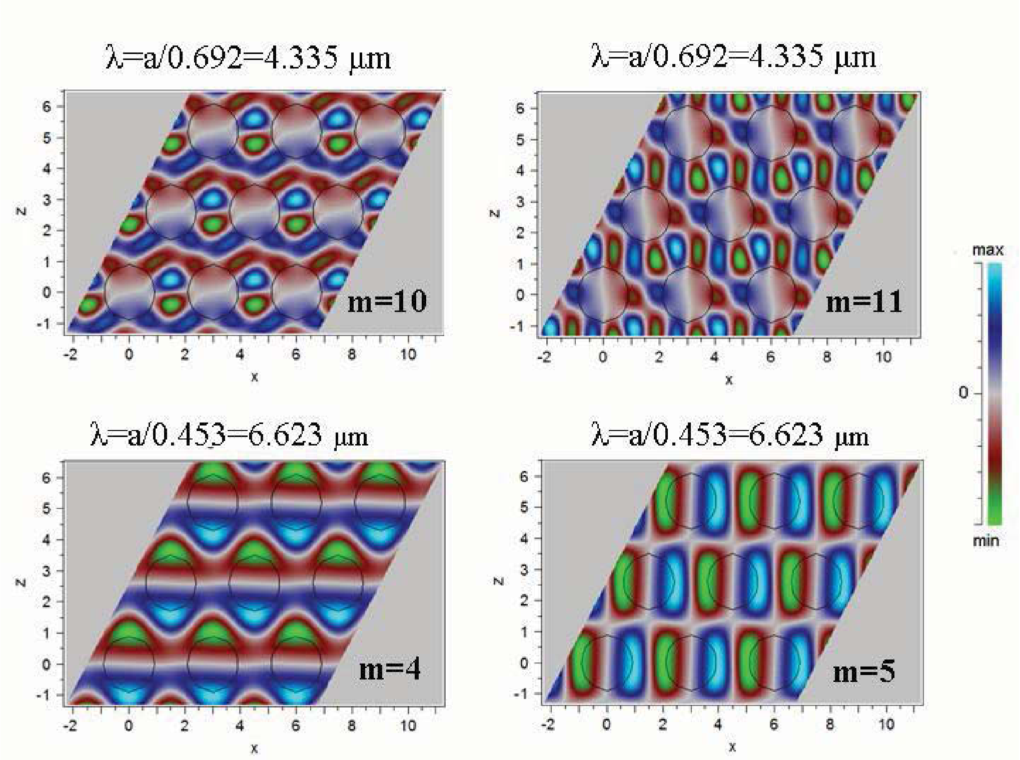

Fig. 3.9. The distributions of the amplitude of the E_y component calculated by the 2D PWEM for doubly degenerated E_1 eigenmodes at the Γ-point of the TM-band structure. The same as in Fig. 3.3.

It is apparent at first sight that the distributions of the E_y field are nothing else as the eigenmodes of a 2D PhC which are shown in Fig. 3.3. In particular, the two patterns at dip 1 correspond to the 10th and 11th modes while the dip 3 patterns are virtually identical to the 4th and 5th modes. These four eigenmodes are shown enlarged in Fig. 3.9 for easier comparison.

It is worth to note that the eigenmodes shown in Fig. 3.9 correspond to the E_1 irreducible representation and have a dipole-like symmetry. The dipole character of the eigenmodes means that on the opposite sides of a pore the E_y field has opposite signs. In one case the dipoles are oriented along the x-axis, in the other case – along the z-axis. Thus, each of the degenerate modes is excited by a wave with the correspondingly polarized source in 3D FDTD simulations. This fact explains why the dips 1 and 3 do not depend on the polarization of the source.

Table 3.5 shows the spectral positions of the reflection dips obtained from FDTD calculations, the spectral position of the corresponding PhC modes calculated by 2D PWEM, and the relative mismatch between them. About 1% mismatch for the dip 1 and 3% for the dip 3 is considered as very good agreement. We want highlight here that 2D PWEM and 3D FDTD simulations are not just different methods applied to the same model. In the former case the structure is infinite (also in y-direction!), there are no sources, metallic parts, or PhC-air interfaces, besides, the wavevector of the waves is supposed to lie exceptionally within the *xz* plane (the plane of periodicity). The FDTD simulations deal with the structure of subwavelength thickness with the gold layer on top and the wavevector of the incident wave has zero projection on the *xz* plane.

Table 3.5 The spectral positions of the dips 1 and 3 calculated by FDTD, PWEM and relative mismatch between them.

	Dip1 PWEM	Dip1 FDTD	relative	Dip3 PWEM	Dip3 FDTD	relative
spectral position	4.33 μm	4.39 μm	0.99	6.62 μm	6.84 μm	0.97

Thus, we conclude that polarization conversion and enhanced transmission of light through the subwavelength holes in the gold layer appears due to the coupling of the incident wave to the doubly degenerate dipole eigenmodes at the Γ-point of the TM band structure.

Now we turn our attention to the dip 2. As follows from the Table 3.4 (diagram "f"), the transmitted light retains the polarization of the incident wave. In addition, the electric field has its highest amplitude within the pores and not in the high-index material. In principle, we can think about two phenomena which can result in the observed situation: (i) a pore can be considered as an isolated cylindrical cavity and the incident wave couples to a mode of this cavity and (ii) the wave couples to one of the PhC eigenmodes.

First, we check whether the assumption (i) is correct. For a cylindrical cavity with radius r and height h the lowest eigenmode (when $h>2r$) has the frequency [126]

$$\omega_{111} = \frac{1.841}{\sqrt{\varepsilon\mu}}\frac{c}{r}\sqrt{\left(1+2.912\frac{r^2}{h^2}\right)}. \tag{3.2}$$

For our parameters (r=0.9 μm and h=4 μm) the wavelength corresponding to this frequency will be λ=2.87 μm which is out of the examined spectral range. Although formula (3.2) is derived for a cavity with perfectly reflecting walls we conclude that dip 2 is most probably not due to the coupling to a mode of a cylindrical cavity.

Regarding the assumption (ii) a *TE band structure* (electric field polarized in the plane of periodicity) of the PhC should be considered. Repeating the procedure which was performed for the dips 1 and 3 we plot first the 3D distributions of E_z and E_x fields within the structure for the two corresponding polarizations of the source (Figs. 3.10a and 3.10b).

By examining the eigenmodes of the TE band structure at the Γ-point it is easy to find those two which correspond to the field distributions obtained in FDTD simulations. These eigenmodes are shown in Figs. 3.11a and 3.11b. Thus, we see that the dip 2 appears due to coupling of the incident wave to the eigenmodes of the *TE band structure* at the Γ-point.

Table 3.6. The spectral positions of the dip 2 calculated by FDTD and PWEM and a relative mismatch.

	Dip2 PWEM	Dip2 FDTD	relative
spectral position	5.23 μm	5.01 μm	0.96

The spectral positions of the dip 2 calculated by 2D PWEM and 3D FDTD are compared in Table 3.6. The mismatch between two values is slightly above 4% which is higher than for the dips 1 and 3 but still can be regarded as satisfactory. We will show later that the dip 2 is very sensitive to the depth of the pores and the mismatch increases with decreasing depth of the pores.

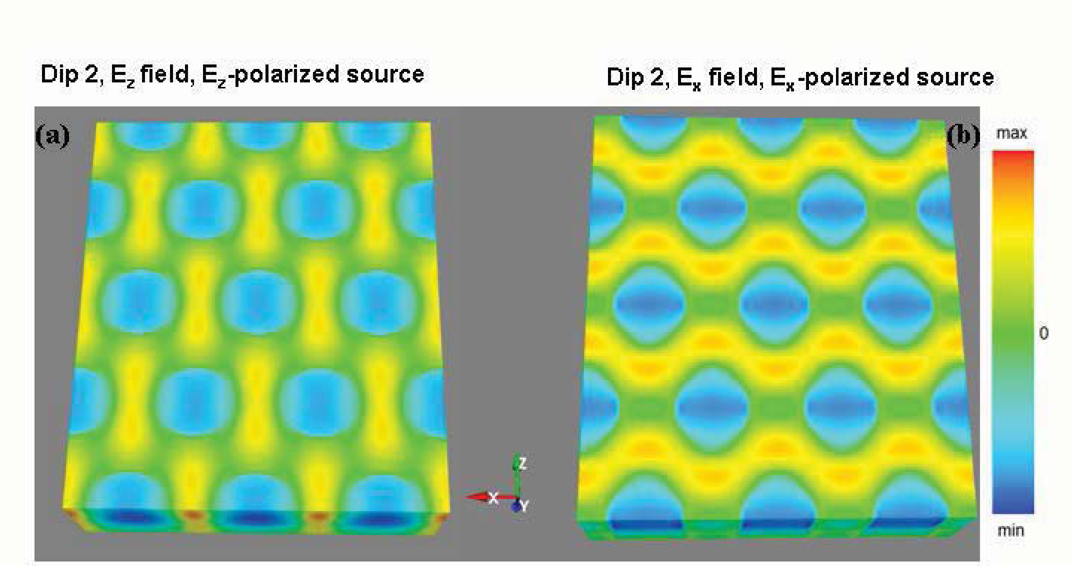

Fig. 3.10. 3D instantaneous distributions of the strength of the E_z (a) and E_x (b) components of the electric field, both are for λ=5.01 μm (dip 2). The polarization of the source is E_z for (a) and E_x for (b).

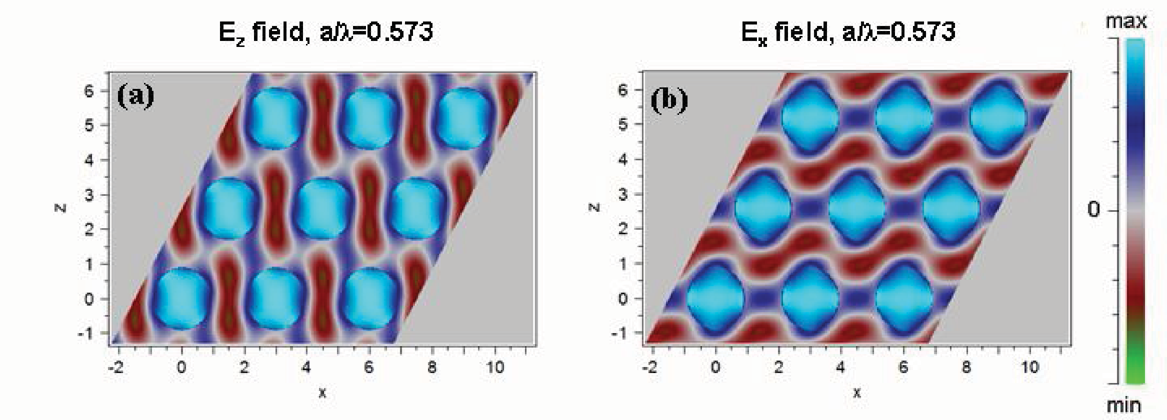

Fig. 3.11. The distributions of the amplitude of the E_z (a) and E_x (b) components calculated by the 2D PWEM for 5th and 6th eigenmodes at the Γ-point of the TE-band structure.

Although the correspondence between the 3D FDTD field distribution and the eigenmodes of the PhC is apparent we have performed simulations for a single hole in otherwise the same structure. This is a direct way to distinguish between the collective effects which are due to periodic structure from that which appear also for a single cylindrical hole.

The transmittance and reflectance for a single hole are shown in Fig. 3.12a. No reflections dips are observed in this case. This calculation was performed with the PML absorbing boundary conditions applied for all facets of the computational domain. This explains why the reflectance is not close to 100%. Cross-section of the E_y component amplitude is shown in Fig. 3.12b for the wavelength of λ=5 μm which corresponds to the dip 2.

Thus, we have proved that the spectral features observed, i.e. the dips 1, 2 and 3, are the result of the interaction of the plane wave with the periodic array of pores. However, there are some important questions which are still not answered. So far we have explained *what* happens: a plane wave couples to distinct PhC modes. In the subsequent sections we will try to answer the further two questions: *how* and *why* the coupling appears.

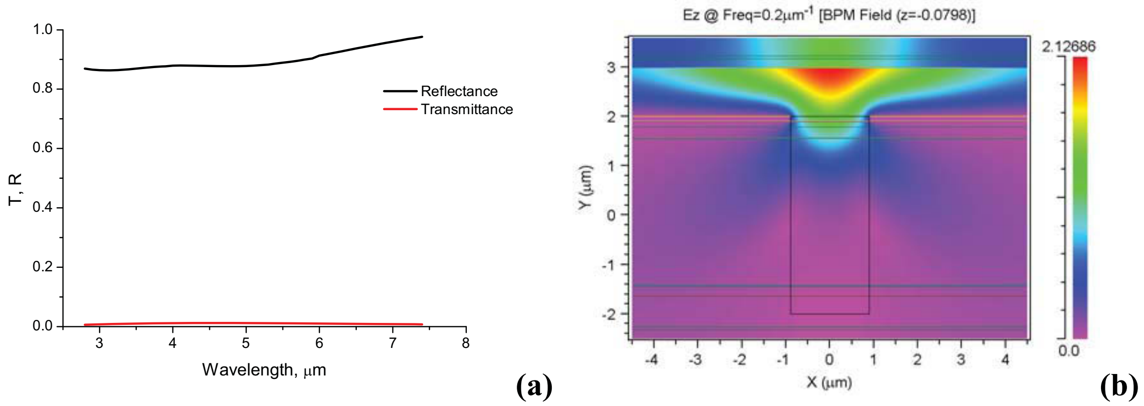

Fig. 3.12. (a) Reflectance and transmittance spectra of a single hole. PML boundary conditions are applied to all facets of the computational domain. (b) The amplitude of the E_z component at λ=5 μm.

3.2.3. Examining the vector fields.

So far we have ascertained that all three reflection dips appear due to the coupling of an incident wave to the eigenmodes of the 2D PhC. In the case of dip 2 the situation is intuitively understandable: a plane wave with a certain polarization excites a TE eigenmode having the same polarization of the electric field. However, it is not apparent *what* forces a plane wave to change its polarization and couple to TM eigenmodes (dips 1 and 3). In order to explain this, a deeper insight into the structure of electromagnetic field within the system is required.

In Fig. 3.13a the xy cross section (z=-3 μm) of the instantaneous distribution of the electric field vectors at the wavelength of λ=4.39 μm (dip 1) is shown for the E_x-polarized source. Figure 3.13b shows the corresponding distribution of the E_y amplitudes averaged over one period. The both pictures are taken at the end of a calculation when the transmittance and reflectance have reached their steady state values. The size of the arrows is proportional to the strength of the field. We want to draw attention to two important points:

(i) the incident wave penetrates for some distance through the pores, as a consequence, the electric field within the pores retains the E_x-polarization of the incident wave (area "1" in the figure);

(ii) It follows from Maxwell's equations that the tangential component of the electric field must be continuous over the interface between two media [1]. Inside the gold both the tangential and normal components of the electric field tend to zero due to the free carriers. Thus, the tangential component of the electric field in the dielectric near the gold-dielectric interface must be also zero (area "2" in the figure).

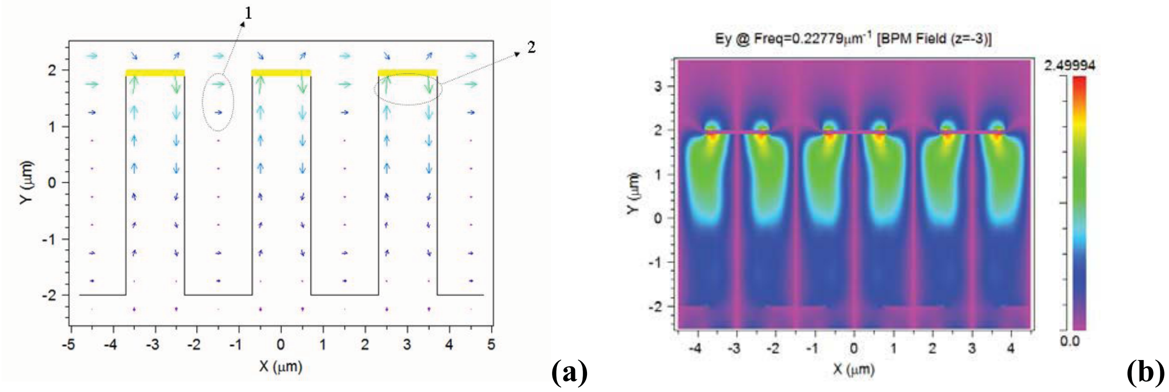

Fig. 3.13. (a) The xy cross-section (z=-3 μm) of the electric field vectors at λ=4.39 μm (dip 1) for E_x-polarized source. The size of the arrows is proportional to the field strength. Within the area depicted by "1" the field is polarized in x-direction; within the area "2" the field is polarized in y-direction. (b) The amplitudes of the E_y field for the same cross-section as in case (a). In the middle of the pores the E_y amplitudes are zero that corresponds to the area "1".

Under these conditions the only possible configuration where the electric field is continuous within the air regions is "dipole-like" i.e. the electric field below the gold layer has opposite direction on the opposite sides of a pore. We illustrate it by means of a sketch shown in Fig. 3.14. The left picture shows the case which is observed in the simulations: opposite signs of the field on the opposite sides of the pore are consistent with the field within a pore resulting in continuous electric field lines shown by the dashed curves. The right picture shows another possible configuration of the electric field lines: the electric field within a pore is aligned in vertical direction. This situation is not preferable in our model since the incident wave is polarized horizontally. Thus, we call the latter situation as "not preferable". The "not preferable" situation, however, could be achieved if an E_y-polarized plane wave will incident from a side.

The fact that a plane wave incident normally on the metal hole array generates a dipole-like pattern in the vicinity of the surface is actually well-known in the literature and was observed by numerical calculations [116] and experimentally [111]. In both cases a metal plate with holes was located in air and the dipole-like pattern was generated on the both sides of the plate.

As we have seen in the previous subsection (see Figs. 3.8 and 3.9) the eigenmodes which are excited at dips 1 and 3 also have dipole-like pattern. Thus, when the frequency of the incident wave approaches the frequency of a PhC dipole mode the electromagnetic energy starts to accumulate in the PhC region resulting in both enhanced transmission and polarization conversion. In other words, *the energy from a dipole-like pattern generated by the metal hole array effectively couples to the dipole eigenmodes of the PhC.*

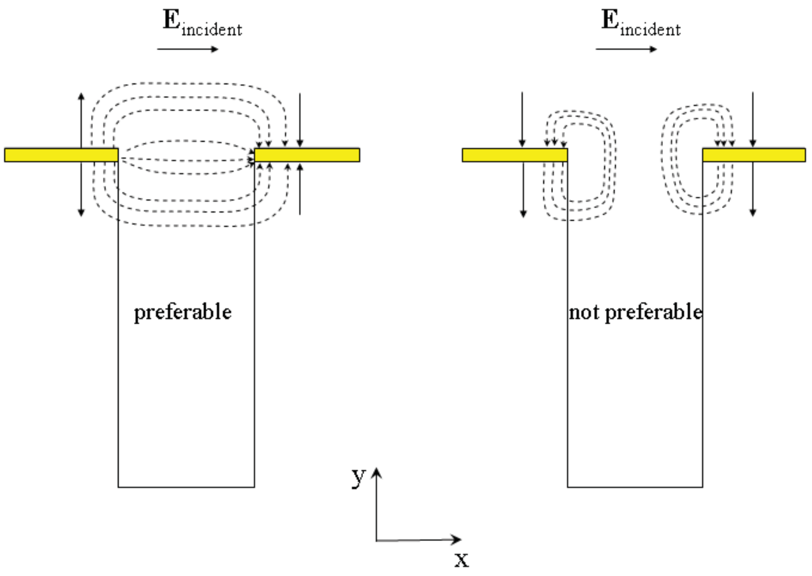

Fig. 3. 14. Sketch of two possible configurations of the electric field lines. The situation in the left picture is consistent with the requirement of vanishing tangential component on the gold interface as well as with E_x-polarized wave within the pore. The situation in the right picture is consistent with the requirement of vanishing tangential component on the gold interface but *not consistent* with horizontally polarized electric field of the incoming wave.

An enlarged picture of electric fields in the vicinity of the gold layer is shown in Fig. 3.15. It is seen that the field vectors really represent the "preferable" situation sketched in Fig. 3.14. Under the gold parts the field is directed strongly along the y-axis, i.e. $E_x \sim 0$. Within the pores both E_x and E_y are non-zero. However, near the left and the right edges of the gold part shown, the E_y is small since it is a tangential component for the gold-air interface there. It is also interesting that the field in the middle of the gold interconnect (at $x=0$) are zero. This is because at $x=0$ the phase of the E_y field changes by $\pi/2$. It is seen in Fig. 3.13b that exactly in the middle of the pores (e.g. at $x=1.5$ μm) the amplitude of E_y

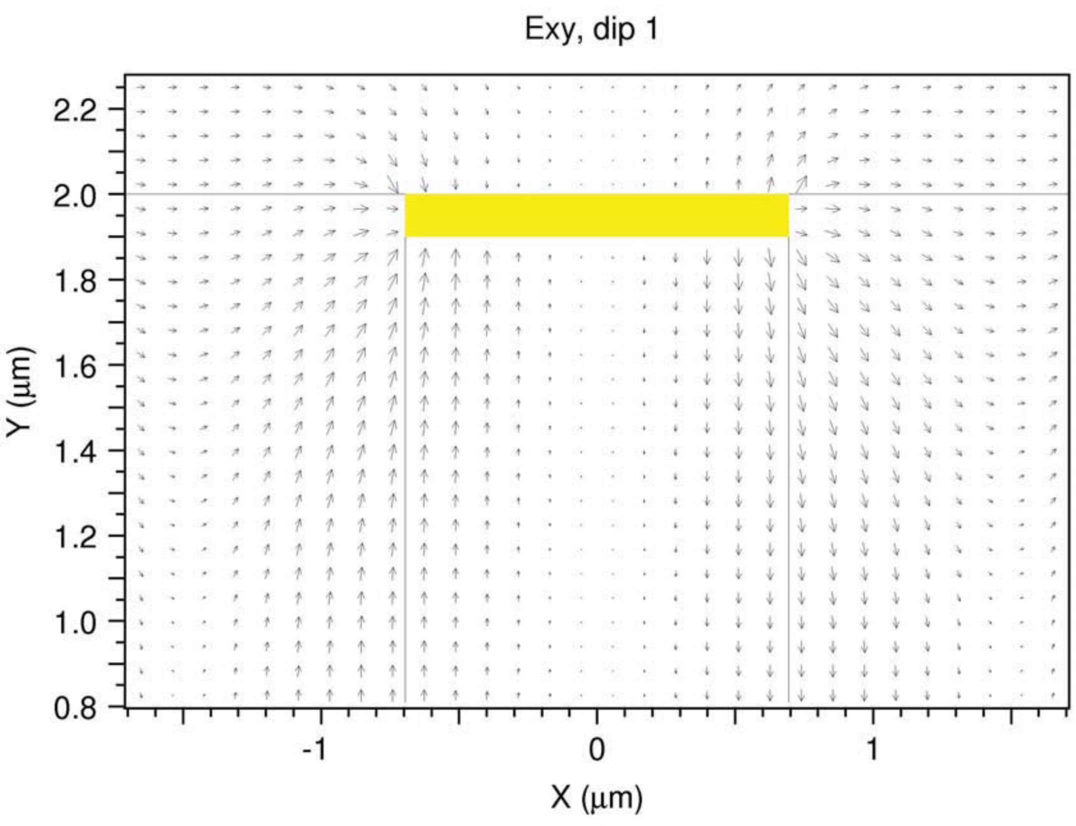

Fig. 3. 15. The xy cross-section (at z=-3 µm) of the instantaneous electric field vectors in the vicinity of the gold at the same time instant and wavelenth as in Fig. 3.13a.

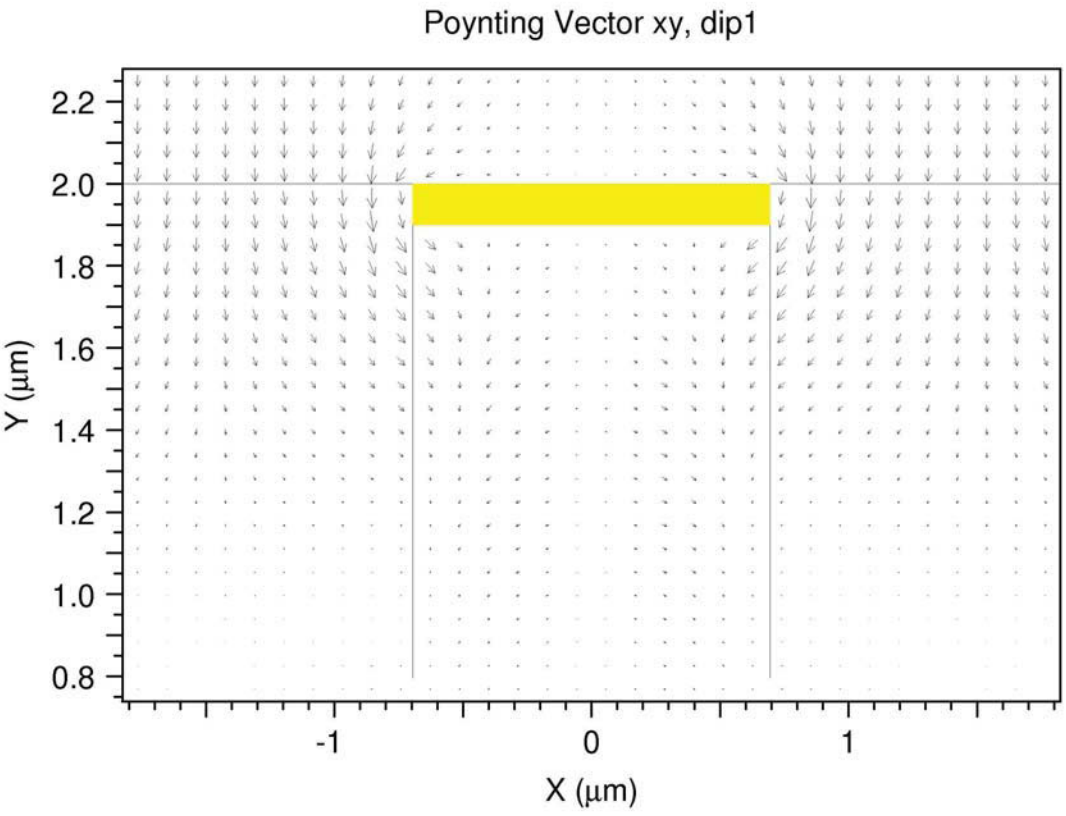

Fig. 3.16. The xy cross-section (at z=-3 µm) of the instantaneous Poynting vectors in the vicinity of the gold at the same time instant and wavelength as in Fig. 3.13a.

field is also zero. This is also a point where the phase of the E_y component changes by $\pi/2$. However, the E_x component is non-zero in this case.

A similar picture can be also obtained for an E_z polarized source, but the zy cross-section should be considered in this case.

Now let us consider the flux of the electromagnetic energy or Poynting vectors for the same simulation. The instantaneous distribution of the Poynting vectors is plotted in Fig. 3.16 for the same time step and the same spatial region as shown in Fig.3.15. In free-space the Poynting vector of a plane wave has the same direction as its wave vector. Thus, initially the x-component of the Poynting vectors was zero. In our case, when the light couples to a TM PhC mode, the energy flux is directed *from the air holes towards the high-index material regions*, as it clearly seen in Fig. 3.16. Within the high-index material regions the energy flux has a complicated character that reflects the fact that excited PhC eigenmodes are at Γ-point of the Brilloun zone, in other words, they correspond to standing waves.

As it was concluded previously the dip 2 is due to coupling to TE eigenmodes, e.g. the electric field retains the polarization of the incident wave. In Fig. 3.17 the xy cross-section (at z=0 μm) of the electric fields at λ=5.01 μm, e.g. at the minimum of the dip 2. E_x-polarized source was used for this calculation. The picture is now completely different in comparison with that for the dip 1. Although above the gold layer the distribution is still dipole-like below the gold the field is polarized almost exclusively in the x-direction, in other words, almost no y-component of the electric field appears within the photonic crystal region. One can also see that the amplitudes of the electric field are much larger within the pores than in the material.

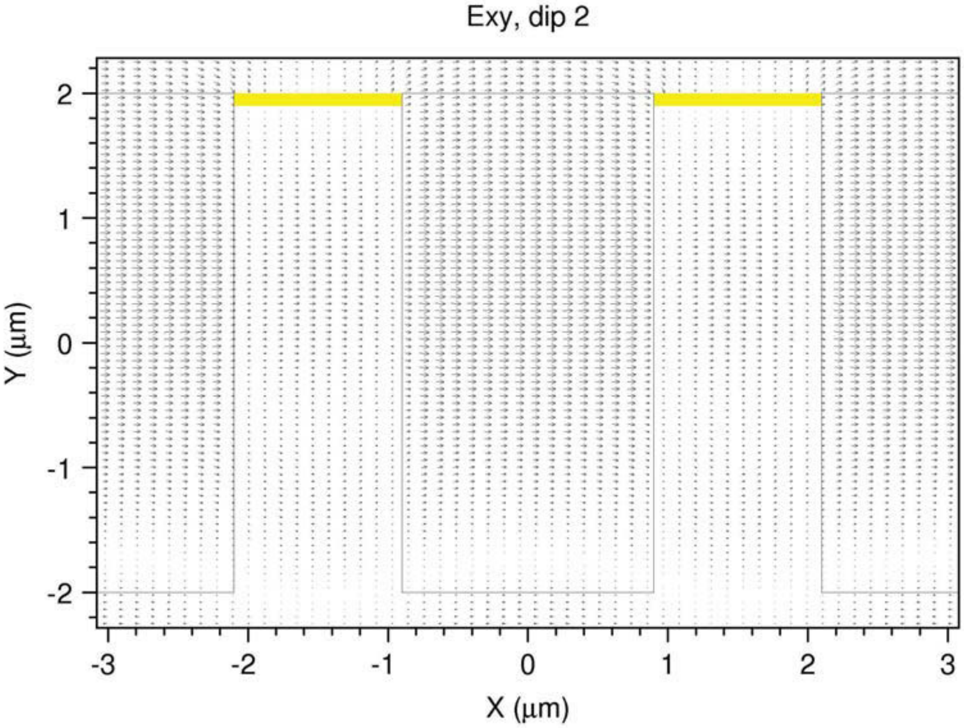

Fig. 3.17. The xy cross-section (z=0 µm) of the instantaneous electric field vectors at λ=5.01 µm (dip 2) for E_x-polarized source. The size of the arrows is proportional to the field strength. The polarization of the EM below the gold is the same as that of the incident wave which corresponds to the excitation of a TE mode of the PhC.

In order complete our analysis of the vector fields we also consider the case of the dip 3. The cross-section of the electric fields at z=0 µm for the E_x-polarized source is shown in Fig. 3.18. The picture is very similar to that obtained for the dip 1: the E_y component dominates below the gold and on the opposite sides of a pore it is directed in opposite directions. However, in the case of dip 3 the field coupled to the PhC mode is more localized below the gold in comparison to the dip 1. The fields are very small at the distance of 2 µm below the gold (y=0 µm) and are almost zero at the distance of 3 µm below the gold (y=-1 µm). The Poynting vector picture (Fig. 3.19) also shows that the energy flux is directed from the air regions into the high-index material. Moreover, the E_x-component of Poynting vectors (which is absent in the incident wave) dominates over the whole region below the pores. It can be also deduced from Fig. 3.19 that the energy accumulated in the excited mode is higher than the energy which passes through the system from the top to the bottom.

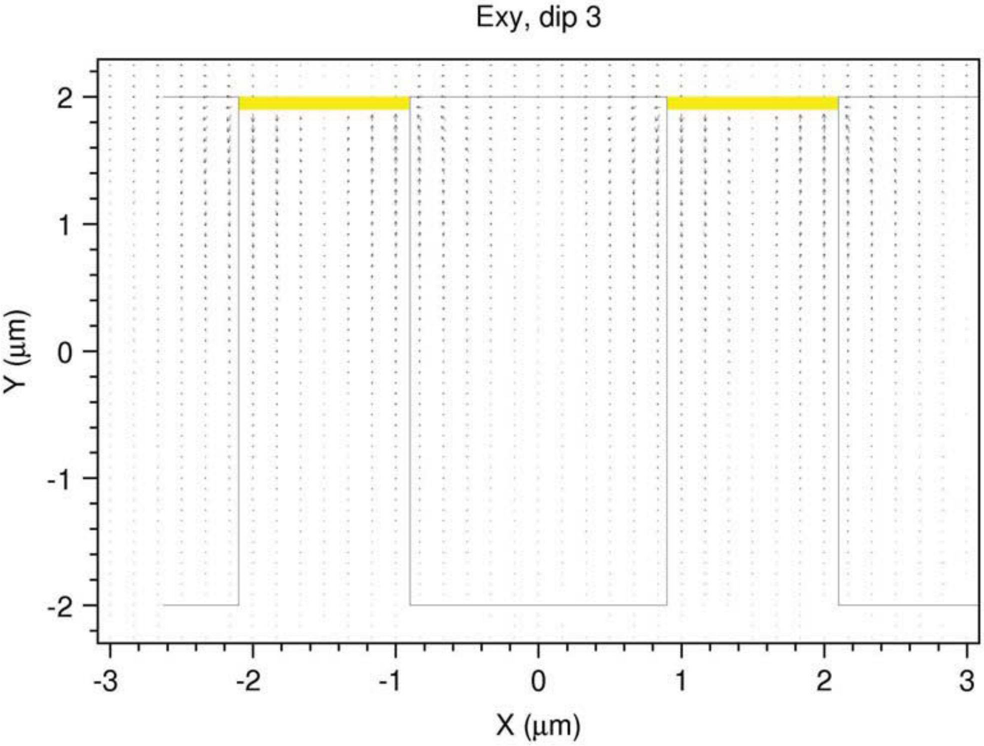

Fig. 3.18. The xy cross-section (at z=0 μm) of the instantaneous electric field vectors at λ=6.84 μm (dip 3) for E_x-polarized source. The EM field below the gold has a dipole-like character and is mostly polarized along the y-axis.

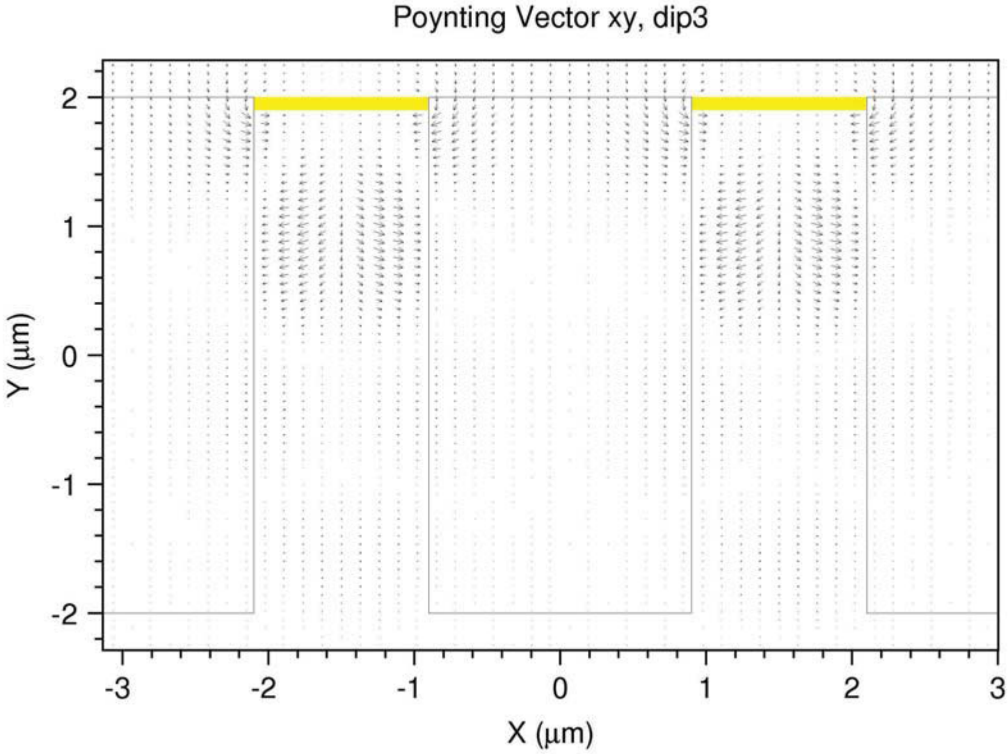

Fig. 3.19. The xy cross-section (at z=0 μm) of the instantaneous Poynting vectors at λ=6.84 μm (dip 3) for E_x-polarized source. The Poynting vectors below the gold have strong x-component which is absent in the incident wave.

It is necessary to note that all distributions of the electric fields and Poynting vectors presented in this subsection are consistent with the previously examined distributions of the field amplitudes. As an example, the conclusion that the mode excited at the dip 3 is more localized below the gold than the mode at the dip 1 can be also made by examining the field amplitudes shown in Table 3.4, in particular by comparison the diagrams "b" and "h".

It is important to remember, however, that the vector distributions are the snapshots, e.g. the instantaneous distributions. Thus, they correspond to certain phases of the electromagnetic field. These phases are actually arbitrary since the pictures are taken at a certain timestep of the calculation (in this subsection ct=1600 µm). In principle, the situation is possible when the fields are "caught" at a time instant when they have zero or close to zero values. Since we do not show the magnetic fields at the same time instant additional calculations were performed where the phase of the source was shifted by $\pi/4$. These calculations confirmed that the shown distributions do represent some average state when the fields are neither at the maxima nor at the minima.

3.2.4. The role of the gold layer

We can consider the investigated structure as being composed of two important constituents: a gold layer with holes and a 2D PhC. According to our conclusions from the previous subsections, the existence of the gold layer plays a crucial role at least for the dips 1 and 3. The Maxwell's boundary conditions "force" the electric field to be perpendicular to the gold interfaces that makes the observed polarization conversion effect possible. At the same time, a PhC structure provides a set of the eigenmodes so that the waves diffracted on the holes can couple to some of them if the frequency of a wave and the symmetry of the diffraction pattern fit that of an eigenmode.

A great advantage of the 3D FDTD simulations is the possibility to easily exclude the ingredients of the system from the simulations. Thus, we can define which role each constituent of the system plays in extraordinary transmission and polarization conversion effects.

In Fig. 3.20 the three reflection curves are plotted: the solid is the same as in Fig. 3.6 (PhC with gold), the dashed is for the same structure but without the gold layer, and the dotted is for the single gold layer with holes in air. One can see that the dips 1 and 3 appear only if both PhC and gold are present.

A PhC without gold (dashed) exhibits generally much lower reflectance with two broad and shallow reflection dips within the examined spectral region. The right dip (λ=5.08 µm) we attribute to the excitation of the same TE PhC eigenmode as in a structure with gold (dip 2). The nature of the left dip (λ= 4.6 µm) is so far unclear, probably it is due to the excitation of another TE mode. The reflection from a single gold layer increases monotonically with increasing wavelength and does not have any features within the examined spectral range.

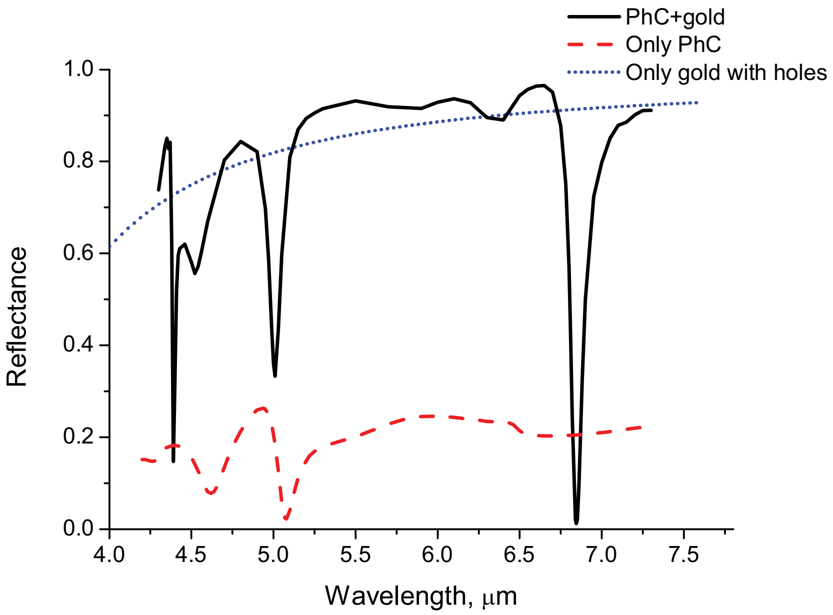

Fig. 3.20. Comparison of the reflectance of the same structure as in Fig. 3.6 (solid), the same structure but without the gold layer (dashed), and single gold plate with holes (dotted).

3.2.5. The influence of the radii of the pores

It is worth to note that the entire previous analysis was done for the same parameters of the 2D hole array. Of course if we have made correct conclusions about the nature of the spectral features they should also appear for a variety of structures with different parameters.

There is a well-known photonic crystal "rule of thumb": if the average refractive index of a photonic crystal decreases then the dispersion branches of the band structure shift to higher frequencies. This gives a very straightforward way to check whether some effect appears due to a PhC or not. In Fig. 3.21 three reflection curves are plotted for three structures with different radii of the pores. All other parameters are the same and shown in the figure caption.

First of all, it is seen that the decrease of the radius of the pores results in the blue shift of the reflection dips. This effect appears most clearly for dip 3. In addition the depth and the width of the dips is different for different radii. For instance, when the pores are large (r=0.365a) the dip 2 has a minimal reflectance of less than 0.5%. The minimum of the dip 2 is significantly higher for r=0.3a being approximately 33%. For the radius r=0.25a the dip 2 is very weak and it practically disappears for r=0.2a (not shown). We explain this phenomenon by the correspondence between the diameter of the pores and the wavelength of the dip 2. In the case (a) the diameter of the pores is 2.19 μm and the dip 2 wavelength is 4.44 μm, e.g. the diameter of the pores is slightly less than the half-wavelength. In other words the light passes through the holes easily and excites the modes in the PhC. In the case (b) the diameter of the pores is 1.8 μm and the dip 2 minimum is at λ=5.01 μm. So, the wavelength is now above the cut-off condition λ~4r and the incident light has to tunnel through the hole [118]. Nevertheless a considerable amount of EM energy reaches the PhC region and the TE eigenmode is excited. In the case (c) the ratio diameter/wavelength is even smaller so only small amount of light passes through the holes, as a consequence, the incident wave couples to the eigenmode very weakly.

It is also clearly seen from Fig. 3.21 that the dips 1 and 3 are still very pronounced also for the radii r=0.25a. We explain this by the fact that the coupling to TM eigenmodes (dips 1 and 3) happens in the *vicinity of the gold layer* while the coupling to the TE mode (dip 2) takes place in the *volume of the PhC*. Thus, even if the incident wave decays quickly with the distance from the gold, it still couples to the TM modes. We will see in the next subsection that the depth of the pores influence the coupling to TE modes very strongly while the coupling to the TM modes depends on the pores depth weakly.

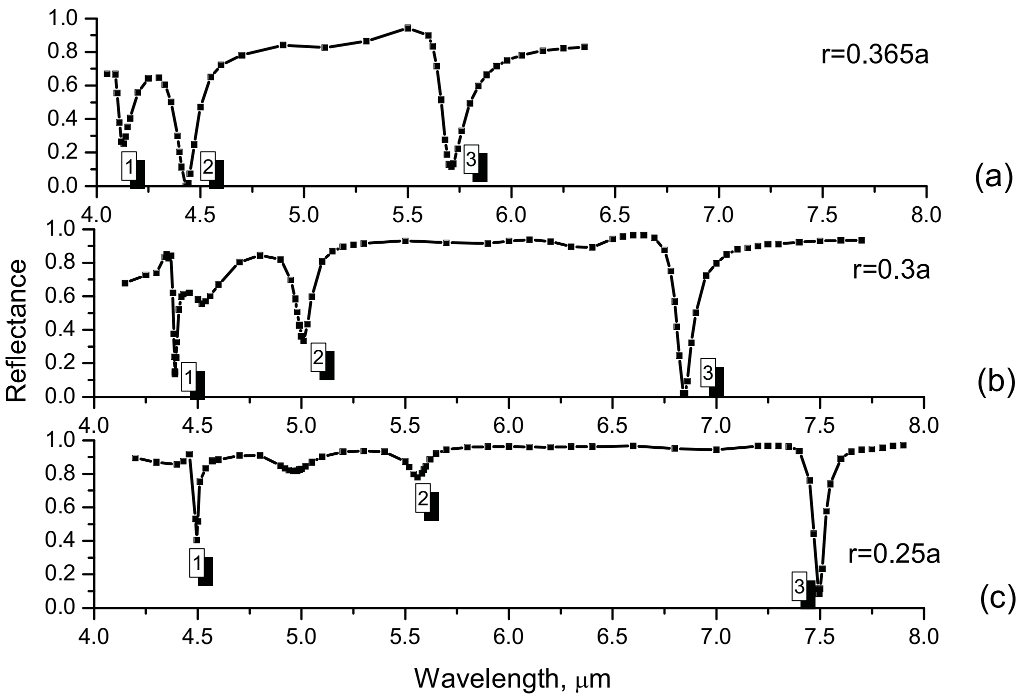

Fig. 3.21. Reflectance spectra of the structures with the same period a=3 μm and refractive index compositions (Table 3.2) but with different radii of the pores: r=0.365a (a), r=0.3a (b), and r=0.25a (c).

We assumed that the redshift of the spectral features with decreasing radii of the pores is due to the redshift of the corresponding PhC eigenmodes. In order to check this we plot the dependence of the spectral positions of the dips 1 and 3 on the size of the pores as well as the positions of the corresponding eigenmodes calculated by the PWEM (Fig. 3.22). We found very good correspondence between the FDTD and PWEM calculations. Moreover, the mismatch between the FDTD and PWEM results is almost constant: the wavelengths calculated by the PWEM are ~1.5% and 3-4% lower than obtained from 3D FDTD model for dips 1 and 3, respectively. We will discuss the possible sources of this mismatch later.

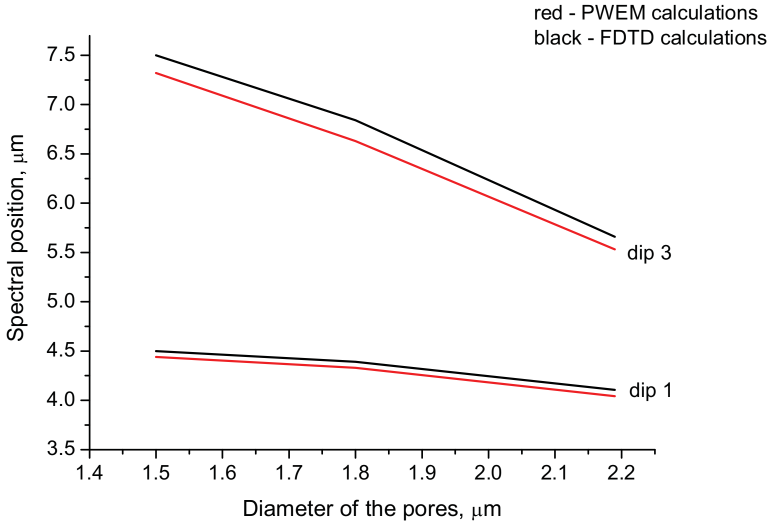

Fig. 3.22. The spectral positions of the dips 1 and 3 vs. diameter of the pores. The black lines are obtained from the FDTD calculations, the red ones– from the PWEM.

3.2.6. The influence of the depth of the pores

In the previous subsections we have used the PWEM for the calculations of the eigenmodes and eigenfrequencies of a 2D PhC. In the PWEM calculations it is implicitly assumed that a 2D PhC is infinitely large in the out-of-plane (parallel to the pores axes) directions. Of course in our 3D model this is not the case. Moreover, the depth of the pores is even lower than the free-space wavelengths of the incident wave. Thus, we have made a set of additional calculations in order to define the influence of the depth of the pores on the obtained results.

We have considered three different values of the pores depths (h=4 μm, h=2.5 μm, and h=1.5 μm) for two different values of the pores radii (r=0.365a and r=0.3a) keeping the lattice constant unchangeable (a=3 μm). The results are presented in Fig. 3.23.

We want to draw attention to the strong dependence of dip 2 on the pores depth. The decrease of the depth of the pores from 4 μm to 2.5 μm results in the blueshift and broadening of dip 2. Further decrease of the depth to 1.5 μm eliminates dip 2 totally.

In contrast, dips 1 and 3 are very pronounced even for h=1.5 μm. In the case of r=0.3a (Fig. 3.23a) the change of the depth from 4 μm to 2.5 μm affects the dips 1 and 3 insignificantly: a slight broadening is observed while the positions and the values of the minima remain the same. For h=1.5 μm the dips 1 and 3 are much broader and shallower, the minimal reflectance now are 43% and 39%, respectively.

The situation is again different for *r*=0.365*a* (Fig. 3.23b). Although the broadening of the dips is observed in this case as well, the dips 1 and 3 are deeper for *h*=2.5 μm and *h*=1.5 μm than for *h*=4 μm.

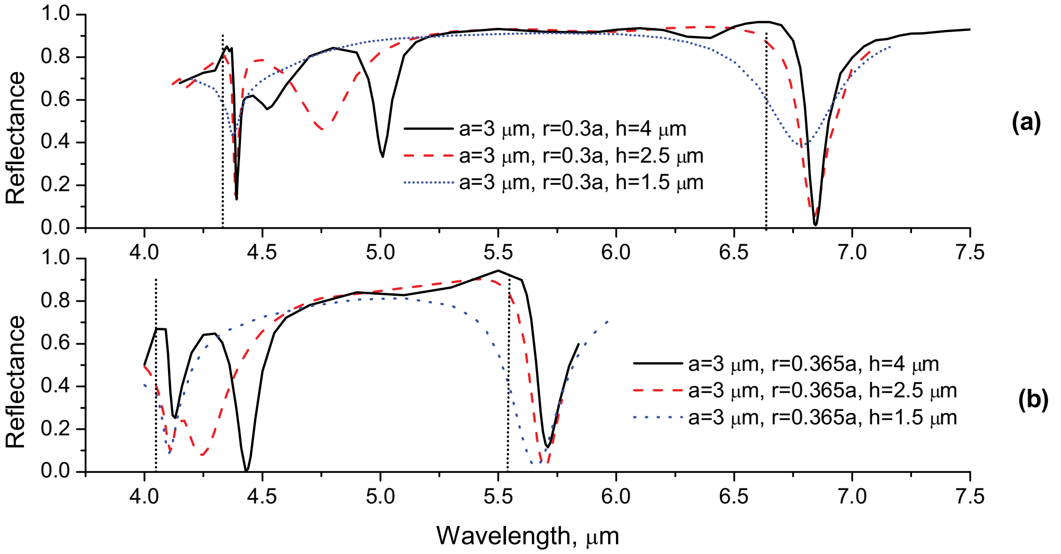

Fig. 3.23. Reflectance spectra for two structures: *a*=3 μm, *r*=0.3*a* (a) and *a*=3 μm, *r*=0.365*a* (b) for different depths of the pores: *h*=4 μm (solid), *h*=2.5 μm (dashed), and *h*=1.5 μm (dotted).

Thus, we conclude that, in addition to the different polarization of the excited eigenmodes, the coupling process itself is different for TE (dip 2) and TM (dips 1 and 3) eigenmodes: in the former case the coupling occurs in the volume of a 2D PhC, so the depth of the pores is crucial, while in the latter case the coupling takes place in the vicinity of the gold layer that results in weaker influence of the pores depth.

Insufficient depth of the pores is most probably the reason for higher mismatch in spectral position between the PWEM and FDTD calculations for the dip 2. We suppose that for the pores depths $h>\lambda_0$ (λ_0 is the wavelength in vacuum) the mismatch will be below 3 %.

3.2.7. The influence of the refractive index of the slab

In this subsection we examine the behavior of the reflectance spectra when the refractive index of the high-index material is changed. Now all geometrical parameters of the structures are fixed: *a*=3 μm, *r*=0.3*a*, *h*=4 μm. In Fig. 3.24 three reflectance spectra are shown for different values of the refractive index. The curve (b) is the same as in Fig. 3.6 and corresponds to the multilayer vertical composition of the PhC with refractive index of the "active region" n=3.2. In the cases (a) and (c) the gold layer is lying on top of homogeneous materials with refractive indices n=3.5 and n=2.5, respectively. It is clearly seen from the figure that the decrease of the refractive index of the PhC leads to a blueshift of the spectral features. In addition, since the low-wavelength part of the spectrum in Fig. 3.24c is already below the cut-off the reflectance is generally low there and some additional dips appear.

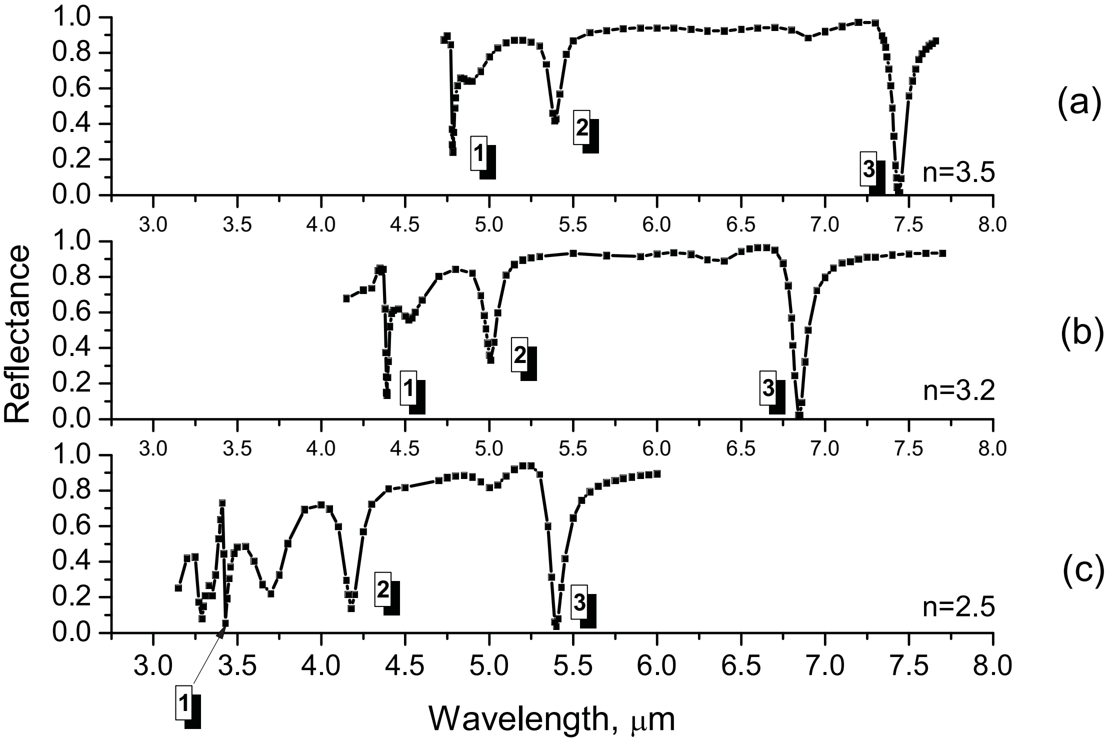

Fig. 3.24. Reflectance spectra of the structures with the same period a=3 μm and radius of the pores r=0.3a but with different refractive indices of the background material. Case (b) corresponds to the multilayer structure (Table 3.2). In the cases (a) and (c) the high-index material of the PhC is homogeneous with refractive index n=3.5 and n=2.5, respectively.

The dependence of the spectral positions of the dips 1 and 3 as well as the positions of the corresponding PhC modes on the refractive index is shown in Fig. 3.25. Similarly to Fig. 3.22 the spectral positions calculated by FDTD are higher than obtained by the PWEM. The mismatch becomes lower as the refractive index decreases.

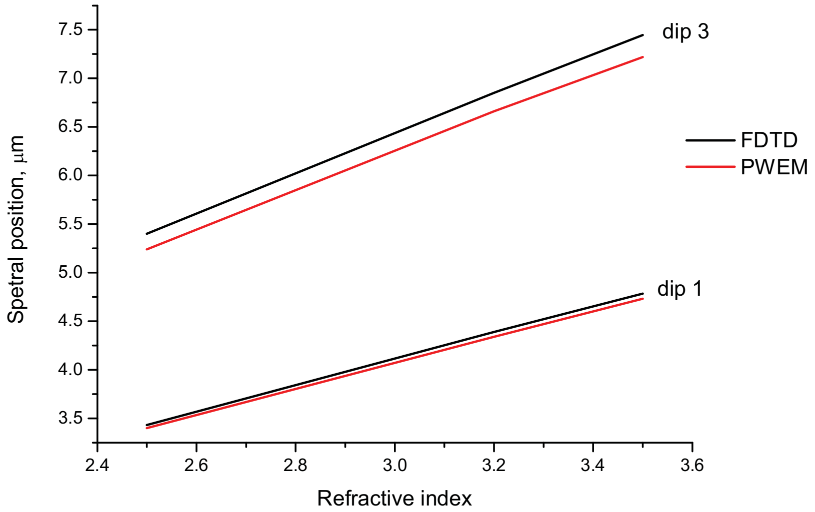

Fig. 3.25. The spectral positions of the dips 1 and 3 vs. refractive index. The black lines are obtained from the FDTD calculations, the red ones are obtained by the PWEM.

3.2.8. Time evolution and finite-size effects

In our 3D FDTD model the four facets of the computational domain which are parallel to the axes of the pores have the periodic boundary conditions (PBC). The model with PBC simulates a structure which is infinitely large within the plane of periodicity of the 2D PhC. Therefore, there are only three ways for EM energy to escape from the system: it can be absorbed by a material with non-zero imaginary part of the refractive index, it can reach the bottom facet of the computational domain with PML and contribute in transmittance, or it can reach the top PML facet and contribute to reflectance. Since all real structures are finite, it is very important to investigate how the coupling effects depend on the size of the structure within the plane of periodicity.

We see several ways to estimate the finite size effects:

1. In the direction of the wave propagation (from top to bottom) our model is 6.1 µm long. That means that after a time of ct=6.1 µm a plane wave would reach the bottom facet if the computational domain contains only air. Since the speed of light in a material with a refractive index n is $v=c/n$ we estimate the longest time for a wave to reach the bottom edge of the computational domain to be approximately ct=15 µm. In any FDTD simulation measured magnitudes (e.g. transmittance and reflectance) need some time to reach a steady state, let us call this time as "steady-state time" t_{ss}. Here we assume that a system has reached steady-state if the change in transmittance and reflectance during a period of $c\Delta t$=200 µm is less than 2%. We believe that by considering t_{ss} it is possible to estimate (roughly) how the light travels through the system.

2. Our model contains a material with a high imaginary part of the refractive index – the gold layer. This gold layer is the major source of the energy dissipation. We suppose that

higher absorption rates would correspond to a situation where the waves "stay" longer in the vicinity of the gold.

3. The previous two approaches are of course indirect. The direct way would be to put PML ABC on the all facets of the computational domain and perform a set of simulations with different lateral sizes of the structure. This approach, however, requires time expensive calculations.

First of all we consider the time-dependent transmittance and reflectance for dip 1, dip 2, λ=5.3 μm ("control point"), and dip 3 shown in Figs. 3.26a – 3.26d, respectively. The arrows show the steady-state times.

The shortest steady state time is observed for the "control point" (Fig. 3.26c): ct_{ss}~300 μm. Interestingly, the steady state time for the transmittance is lower than for the reflectance despite the fact that the distance to transmission monitor is larger.

In the case of dip 2 (Fig. 3.26b) the steady-state time ct_{ss} is approximately 500 μm. We suppose that this time is higher than that for the control point because the incident wave couples resonantly to a PhC mode. In the case of dip 1 (Fig. 3.26a) and dip 3 (Fig. 3.26d) the steady state times are ct_{ss}~2000 μm and ct_{ss}~1000 μm, respectively. We believe that higher steady state times in these cases are due to the polarization conversion and localization of the excited TM PhC eigenmodes below the gold layer. Since the excited

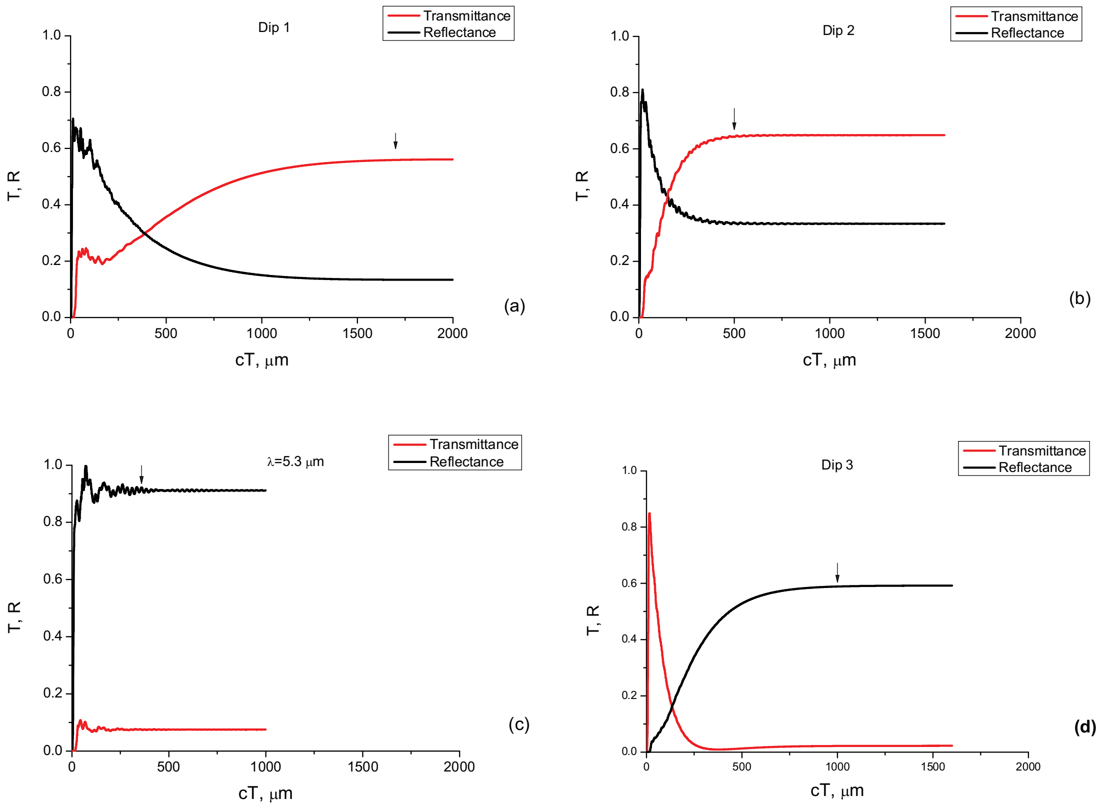

Fig. 3.26. The time dependent transmittance and reflectance for dip 1 (a), dip 2 (b), λ=5.3 μm (c), and dip 3 (d). The arrows show the steady-state time values.

modes are polarized preferably in y-direction the propagation in y-direction is not allowed (an EM wave would be longitudinal in this case). For the same reason the waves cannot couple back to the free space. Thus, the excited TM eigenmode is "localized" below the gold layer. Of course, a part of the incident EM wave still propagates through the structure since we detect transmittance below the PhC. But we will see in the next subsection that the "localized" energy is an order of magnitude higher than the propagating one.

Another fact which indicates a localization of the excited TM dipole modes is the amount of absorbance shown in Table 3.3. The absorbance for dips 1 and 3 is much higher than for dip 2: 31%, 39% and 2 %, respectively. As already said above, the high absorbance can be attributed to the high "dwell time" of the photons in the vicinity of the gold layer, in other words, the wave "stays" in the vicinity of the gold for a long time.

The finite-size effects were also estimated directly. In Fig. 3.27 the reflectance of the model with periodic boundary condition is compared with models which are finite in the plane of periodicity. The red curve is the reflectance with periodic boundary conditions (the same as in Fig. 3.6). The black curve is for a simulation with PML absorbing boundary conditions applied to all six facets of the computational domain. The lateral dimensions of the structure are 12x15.6 μm^2 which is approximately 3x5 periods of the PhC. The blue curves show the reflectance spectrum for a finite structure with lateral size of 18x20.7 μm^2. It is necessary to note that in the calculations with PML ABC in the lateral directions the plane wave irradiated by the source has a Gaussian spatial profile, i.e. the amplitude of the wave is maximal in the center and minimal on the edges of the source. In all cases an E_z-polarized source was used.

It can be seen from Fig. 3.27 that already the black curve exhibits clear dips 2 and 3. The dip 1, however, is very weak in this case. For a larger structure (blue curves) all three dips are more pronounced: the minima of dips 2 and 3 are closer to values of an infinitely large structure, the dip 1 is now clearly seen but still weak. A slight redshift (~1-2%) of all reflection dips with respect to infinite structure is also observed. Currently we are not able to explain this redshift.

The examination of finite size effects brings us to a very important from the experimental point of view conclusion: the coupling to the lowest TM dipole eigenmode (dip 3) appears already for laterally small structures. We suppose that for a structure with lateral dimension of 10*a*x10*a* (*a* is the period of a PhC) the minimum of dip 3 approaches closely the value for infinite structure. At the same time, the dip 1 appears to be very sensitive to the size of the structure. Thus, it might be much more difficult to detect it experimentally.

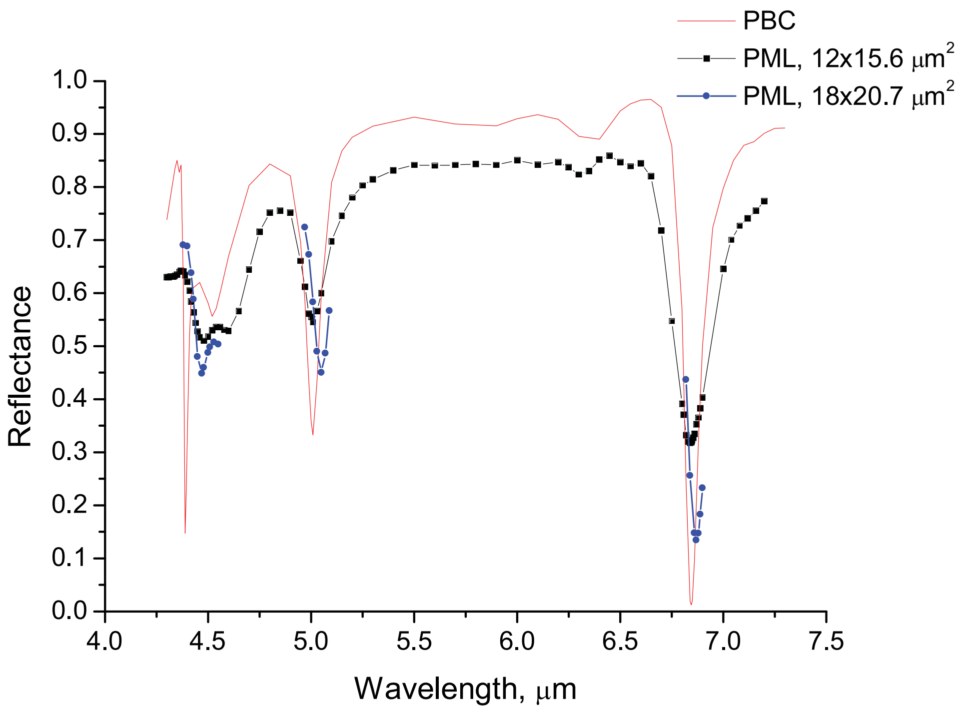

Fig. 3.27. Estimation of finite-size effects. The red curve is for the model with periodic boundary conditions (PBC), e.g. for the structure which is infinite in the lateral directions. The black and the blue curves are for perfectly matched layer absorbing boundary conditions (PML ABC) applied to all facets of the computational domain. The lateral size of the structure is 12x15.6 μm^2 and 18x20.7 μm^2 for the black and the blue curve, respectively. The vertical composition of the structures are shown in Table 3.2; the parameters of the 2D PhC are a=3 μm, r=0.3a.

3.2.9. Quantitative characterization of the polarization conversion

In this subsection we have used an additional C++ program for the calculations of the average energy density of the electric field components below the gold layer at the wavelengths corresponding to dips 1 and 3. The program code is listed in Appendix IV.

The average energy density of the field components is calculated according to the formula:

$$\left\langle |E_\alpha|^2 \right\rangle = \frac{1}{N_V}\sum_{i=1}^{N_V} |E_\alpha^{(i)}|^2 , \tag{3.3}$$

where α denotes one the component (x, y, or z) of the electric field E, N_V is the number of the computational grid points within the integration volume, and $E_\alpha^{(i)}$ is the amplitude of an electric field component in a grid point i within the volume. The information about the fields in separate points of the computational grid is deduced from the 3D field distribution files. Since the 3D distributions of the EM are instantaneous distributions we have performed a pair of calculations – one with zero phase shift and another with the phase shift of π/2. By adding two values of $\left\langle |E_\alpha|^2 \right\rangle$ with the phase difference of π/2 a total intensity of the corresponding field component is obtained.

All values of electric field amplitudes are normalized to the amplitude of the electric field in the generated wave.

We characterize the polarization conversion by the following parameter:

$$\beta = \frac{\left\langle | E_y |^2 \right\rangle}{\left\langle | E_{source} |^2 \right\rangle}, \tag{3.4}$$

where E_{source} means the electric field component which is non-zero in the incident wave (E_x or E_z).

In principle, both average energy density (3.3) and polarization conversion parameter (3.4) depend on the choice of the integration volume. We have chosen two volumes: the volume of the "active region" according to Table 3.2 and the volume of the layer with a thickness of 1.5 µm directly below the gold layer.

The results are summarized in Table 3.7. The second column defines the parameters of the structure and refers to the corresponding reflectance spectrum. The third column shows the volume of integration. The next six columns contain the values of average energy density of the electric field components calculated by (3.6) and the polarization conversion parameter β for dips 1 and 3.

First of all, in all cases shown, the $\left\langle | E_y |^2 \right\rangle$ is higher than $\left\langle | E_{source} |^2 \right\rangle$. This result is not surprising since we have already seen that the electric field below the gold is polarized mostly in y-direction. The value of β is in average about 10 having the minimal value of 4.25 and the maximal one of 19.2. However, the value of β=4.25 was obtained for dip 1 at the wavelength of λ=3.43 µm (see Fig. 3.24c) which is below the cut-off wavelength for the holes (λ<4r) [118]. So, an incident wave is not evanescent within the holes. This leads to higher amount of directly transmitted power (i.e. with the same polarization as in the incident wave).

Rows 4 and 6 contain the data calculated for the same structure but for different integration volumes then for rows 3 and 5, respectively. It is seen that the density of the electric fields averaged over the near-surface volume (0 – 1.5 µm below the gold) are significantly higher then averaged over the volume of the "active region". This confirms our conclusion that excited TM modes are localized below the gold.

Table 3.7. The values of integrated average density of the electric field components at dip 1 and dip 3 for different parameters of the structures. More detailed description: see text.

	Parameters of the structure	Volume of integration	Dip 1			Dip 3		
			$\langle \lvert E_{source} \rvert^2 \rangle$	$\langle \lvert E_y \rvert^2 \rangle$	$\boldsymbol{\beta}$	$\langle \lvert E_{source} \rvert^2 \rangle$	$\langle \lvert E_y \rvert^2 \rangle$	$\boldsymbol{\beta}$
1	r=0.3a multilayer Fig. 3.21b	"active region"	0.39	4.22	10.8	0.32	5.12	12.5
2	r=0.25a multilayer Fig. 3.21c	"active region"	0.19	2.97	15.6	0.29	5.56	19.2
3	r=0.3a n=3.5 Fig. 3.24a	"active region"	0.35	3.05	8.7	0.36	4.85	13.5
4	r=0.3a n=3.5 Fig. 3.24a	0 – 1.5 µm below the gold layer	0.49	6.77	13.8	0.9	11.58	12.8
5	r=0.3a n=2.5 Fig.3.24c	"active region"	0.7	2.98	4.25	0.52	5.0	9.62
6	r=0.3a n=2.5 Fig.3.24c	0 – 1.5 µm below the gold layer	0.88	6.43	7.3	1.18	12.32	10.44

3.3. Simulation results II: single gold plate with holes.

Our investigations would not be complete without an analysis of the optical properties of a single metal plate with holes. Despite the fact that metal hole arrays (MHAs) are already well investigated as was stated in the introduction to this Chapter, we have not found in the literature a comprehensive 3D numerical analysis which is analogous to what we have done in section 3.2 for a PhC covered with metal. In addition, we can use the same but simplified model that gives a nice opportunity to directly compare the results with and without PhC structure.

We have already seen in subsection 3.2.4 that a gold layer in air does not exhibit any reflection dips in the spectral region from 4 μm to 7.5 μm. However, it was shown in the original research [106] as well as in subsequent papers [107-122] that metal hole arrays in air should exhibit a reflection dip (and corresponding transmission peak) at wavelengths which are close to the period of the 2D lattice. It is important to note, that major part of the investigations of the extraordinary optical transmission involves square-lattice MHAs. For instance, in the recent review [122] triangular-lattice MHAs were not mentioned at all.

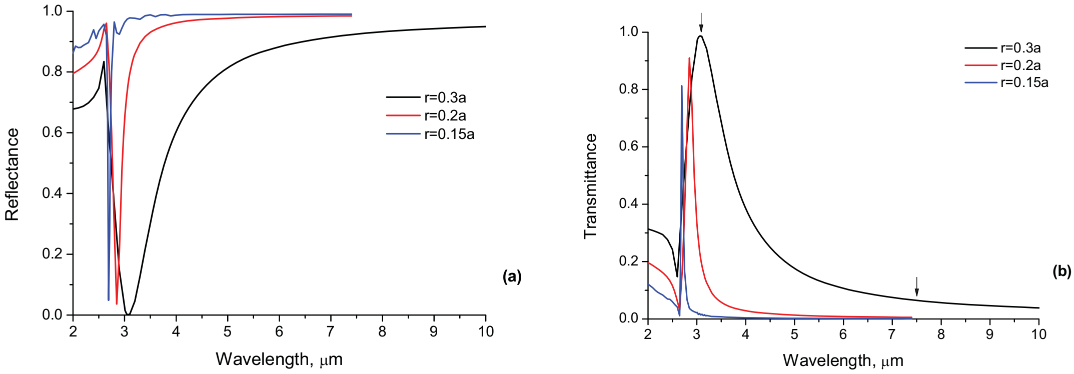

Fig. 3.28. Reflectance (a) and transmittance (b) of a single gold plate with triangular lattice of holes in air. Different colors of the curves correspond to different radii of the holes: r=0.3a (black), r=0.2a (red), and r=0.15a (blue). Period of triangular lattice a=3 μm

The reflection and transmission spectra of a 100 nm-thick gold layer with triangular lattice of circular holes in air are shown in Figs. 3.28a and 3.28b, respectively. Different colors of the curves correspond to different radii of the holes: r=0.3a (black), r=0.2a (red), and r=0.15a (blue). The period of the triangular lattice is 3 μm. The transmission peaks around the wavelength of 3 μm are the "classical" extraordinary transmission effect. The transmission efficiency observed for r=0.15a (Fig. 3.28b, blue curve) is almost 10.

We observe a slight shift of the transmission peak to higher wavelengths with increasing the radius of the pores. Additionally, the EOT peak becomes higher and broader as the radius increases. For $r=0.3a$ (Fig. 3.28b, black curve) the maximal transmittance reaches unity. These conclusions coincide with that made for hole arrays with square lattice [127, 128].

Let us now consider the distribution of EM field for two wavelengths: (i) resonant wavelength $\lambda=3.06$ μm and (ii) non-resonant wavelength $\lambda=7.5$ μm, both for $r=0.3a$. These two points are marked by the arrows in Fig. 3.28b.

The information about the steady-state electromagnetic field within the structure for resonant and non-resonant wavelengths is summarized in Figs. 3.29 and 3.30, respectively. An E_x-polarized source was used for the calculations. All color scales are normalized to the amplitude of the electric field in the wave generated by the source. The 3D field distributions as well as the vector plots show instantaneous pictures, i.e. snapshots. Figs. 3.29a and 3.29b as well as Figs 3.30a and 3.30b show the amplitudes.

As follows from Fig. 3.28b, at the resonance the transmittance reaches unity. This is clearly seen in Fig. 3.29a: the blue areas (the amplitude of the E_x component ~ 1) located above and below the gold layer indicate the incident and transmitted waves. Inside and in the vicinity of the holes the amplitude of the E_x-component is enhanced reaching a value of 4 directly on the edges of the holes. At the same time, the E_x-component just above and below gold parts is close to zero since it is a tangential component there. Thus, from the point of view of the E_x-field the processes appearing at the resonance can be described as follows: a plane wave with an amplitude of 1 impinges the metal hole array; in the vicinity of the hole array E_x-field is redistributed so that the amplitudes have maximal values (up to 4) within the holes and minimal values (down to 0) just above and below the gold parts, further below (>2 μm) the MHA the field is again redistributed so that a *plane wave* is going out of the system. The later fact is most clearly seen on the 3D distribution of the E_x-field (Fig. 3.29c).

The E_y-component (Fig. 3.29b) is absent in the incident wave. Nevertheless the amplitude of the E_y-field reaches a value of 4 above and below the gold parts. It is clearly seen in Fig. 3.29d that the distribution of the E_y-field has a dipole-like character which we have already observed in section 3.2. The amplitude of the E_y-component decays quickly with the distance from the gold and is practically zero at $y=0$ μm (i.e. 2 μm below the gold). From the point of view of the E_y component the interaction of an EM wave with the MHA at the resonance can be described as follows:

- the incoming E_x-polarized wave diffracts at the edges of the holes. Directly above and under the metal parts the E_x component of the diffracted waves tends to zero (due to the boundary conditions for EM field) that results in growth of E_y component there;
- due to the interference between the incident and the diffracted waves the distribution of the E_y field has a dipole-like character (see Fig. 3.14 and corresponding text);
- the same (but antisymmetric with respect to reflection over the surface of the MHA) dipole-like structure is generated on the bottom surface of the metal;

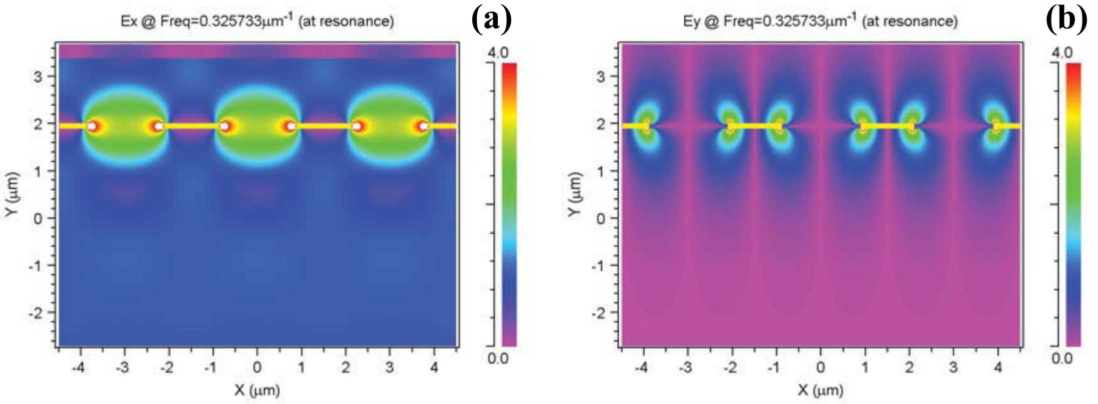
E_x-field, amplitudes

E_y-field, amplitudes

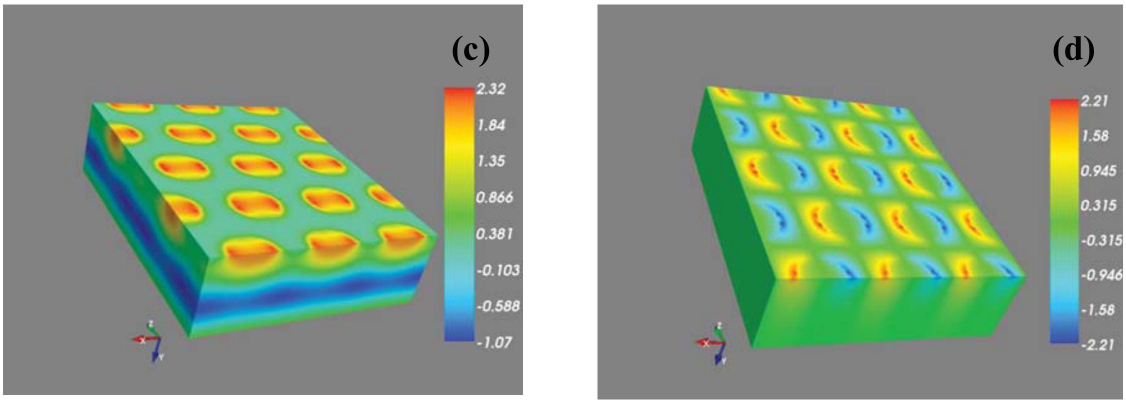
E_x-field below the MHA, 3D, snapshot

E_y-field below the MHA, 3D, snapshot

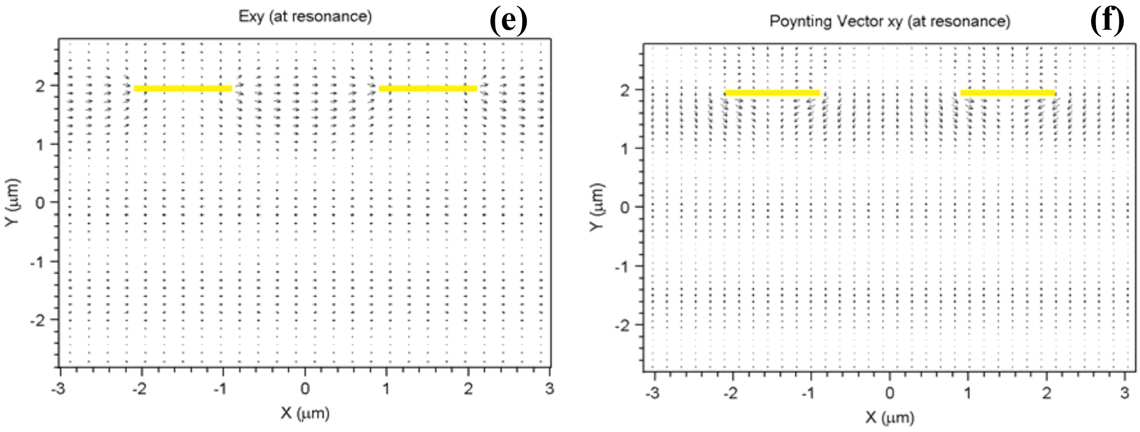
Electric field vectors, snapshot

Poynting vectors, snapshot

Fig. 3.29. Steady-state electromagnetic field for a single MHA in air at resonant wavelength λ=3.07 µm (left arrow in Fig. 3.28). The period of the lattice is 3 µm, the radius of the holes is 0.3a=0.9 µm. The E_x-polarized source was used. (a) and (b) show the 2D cross-sections of amplitudes of the E_x and E_y components, respectively. (c) and (d) are the instantaneous 3D distributions of the E_x and E_y components, respectively. (e) and (f) show the instantaneous electric field and Poynting vectors, respectively.

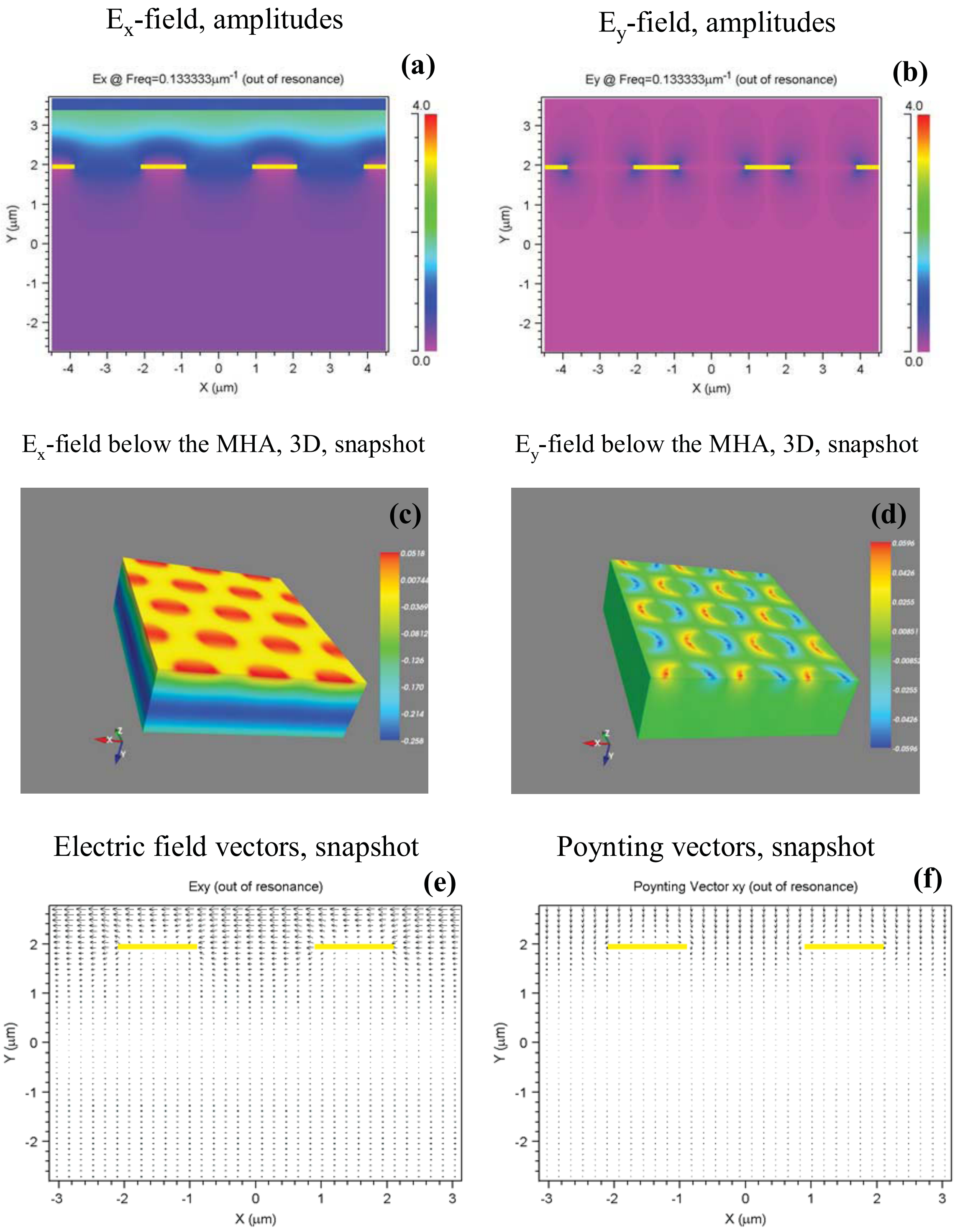

Fig. 3.30. Steady-state electromagnetic field for a single MHA in air at non-resonant wavelength λ=7.5 μm (right arrow in Fig. 3.28). The period of the lattice is 3 μm, the radius of the holes is 0.3a=0.9 μm. The E_x-polarized source was used. (a) and (b) show the 2D cross-sections of amplitudes of the E_x and E_y components, respectively. (c) and (d) are the instantaneous 3D distributions of the E_x and E_y components, respectively. (e) and (f) show the instantaneous electric field and Poynting vectors, respectively.

The distributions of electric field and Poynting vectors are shown in Figs. 3.29e and 3.29f, respectively. The both confirm that the outgoing wave is a plane wave. In Fig. 3.29e, for instance, approximately at y=0 μm as well as at y=-1.5 μm one can see that the vectors are polarized horizontally (E_y~0) and have the same phase. Moreover, at y=0 the electric field vectors are aligned from right to left while at y=-1.5 μm they are aligned from left to right. The distance of 1.5 μm corresponds to approximately half of the wavelength or, in other words, to a phase difference of π/2. In the Poynting vectors distribution it is seen that the energy flux below the MHA is directed from a hole under the gold part.

For the wavelength of λ=7.5 μm (out of resonance) the reflectance is high and the transmittance is low (Fig. 3.28b, right arrow). This fact is clearly observed in the pictures showing the distribution of E_x-component (Fig. 3.30a and Fig. 3.30c). Interestingly, although the amplitude of E_y is also much lower in this case, the dipole-like pattern which is shown in Fig. 3.30d has the same shape as for λ=3.06 μm. Thus, we can make a very important conclusion: *the pattern of the E_y-field appearing after interaction of a plane wave with a MHA in the vicinity of the holes does not depend on the wavelength of the wave.* We suppose that this pattern is defined only by the parameters of the metal plate – the period of the hole lattice and the radius of the holes.

The transmittance spectra of gold MHAs on a substrate are shown in Fig. 3.31. Different colors of the curves correspond to different radii of the holes: *r*=0.3*a* (black), *r*=0.2*a* (red). The dashed curves correspond to the substrate index of *n*=1.5, the solid curves are for *n*=2.2. An increase of the substrate refractive index leads to a redshift of the EOT peaks. Additionally, the maximal transmittance does not reach unity as in the case of an MHA in air.

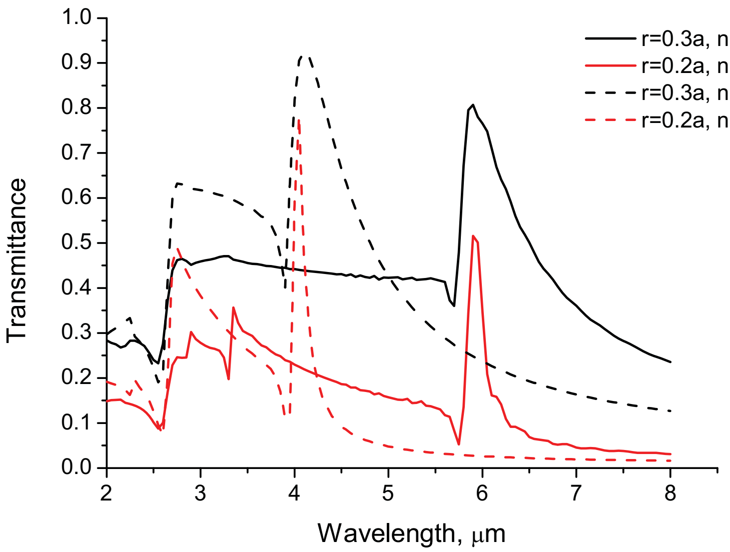

Fig. 3.31. Transmittance through a gold plate with a triangular lattice of holes on a substrate. Different colors of the curves correspond to different radii of the holes: *r*=0.3*a* (black), *r*=0.2*a* (red). The dashed curves correspond to the substrate index of n=1.5, the solid curves are for n=2.2.

The role of surface plasmons.
As we already mentioned in subsection 3.1.1, it is believed that the EOT peaks appear due to excitation of surface plasmons (SP). As an example of a typical explanation of the processes that take place at the resonance we cite the following passage [118]: "… the process can be divided into three steps: the coupling of light to the SPs on the incident surface, transmission through the holes to the second surface and then re-emission from the second surface. At the peak transmissions, standing SP wave are formed on the surface." We do observe a mode which is bound to the surface and has a standing wave character – this is our dipole-like pattern. In our opinion the main requirement for generation of this mode is the existence of a large imaginary part of the refractive index of a material. Due to the boundary conditions for the EM field, the tangential component of the diffracted on the holes wave tends to zero near the metal-dielectric interface. At the same time, the normal component, which is in our case the E_y component (above and below the metal parts), is allowed. This leads to the most "convenient" field distribution with continuous electric field lines – the dipole-like pattern. Thus, it does not matter whether the material of a hole array is a real metal, perfect electric conductor or doped semiconductor – the only requirement is substantial imaginary part of the refractive index. Actually, we observed the dipole-like pattern also for lossless dielectrics but the amplitude of the E_y-field was very small in that case.

Nevertheless the SP model of the EOT effect is the most widely accepted model now. Let us check the correspondence of this model to our results obtained for triangular-lattice MHAs.

A surface plasmon or, more generally, a surface electromagnetic mode can exist on a flat interface between two media if one of the media has a negative real part of the dielectric constant [129]. This condition is satisfied for most of the metals for frequencies below the plasma frequency. Generally, metals are characterized by a complex dielectric constant $\varepsilon_m = \varepsilon_{rm} + i\varepsilon_{im}$ and the dispersion equation of a surface mode depends on both real and imaginary parts of ε_m [129]. However, if the condition

$$\varepsilon_{rm} < 0,\ |\varepsilon_{rm}| >> \varepsilon_{im},\ |\varepsilon_{rm}| > \varepsilon_d \tag{3.5}$$

is satisfied then the real part of the wavevector of the surface mode (on a flat surface without holes) is given by [129]

$$k_r = \frac{\omega}{c}\sqrt{\frac{\varepsilon_{rm}\varepsilon_d}{\varepsilon_d + \varepsilon_{rm}}}, \tag{3.6}$$

where ε_d is the dielectric constant of the non-metallic medium. In our simulations the refractive index of the gold is given by n_{Au}=3.11+i45.3. The corresponding dielectric constant is then ε_{Au}=-2042+i282. Thus the conditions (3.5) are satisfied in our model.

The formula for calculations of the wavelength of first-order transmission peak due to excitation of surface plasmons in triangular-lattice MHAs is then given by [118]

$$\lambda_{\max} = \frac{a\sqrt{3}}{2}\sqrt{\frac{\varepsilon_{rm}\varepsilon_d}{\varepsilon_{rm}+\varepsilon_d}}, \tag{3.7}$$

where a is the lattice constant. We want to draw attention to the fact that the dependence of the peak position on the radius of the holes is not included in the expression (3.7). This is because (3.7) is obtained by combining the expression for a SP wavevector on a surface without holes (3.6) and grating momentum-matching condition [118]. Thus, (3.7) is more exact for smaller radii of the holes, in other words, when the flat metal surface is less disturbed by a 2D grating of holes.

The comparison between the positions of peaks maxima calculated by (3.7) and the ones obtained from 3D FDTD is shown in Table 3.8 for different refractive indices of the substrate. The 3D FDTD values are obtained with a hole radius r=0.2a =0.6 μm. We conclude that the values obtained by 3D FDTD method are red-shifted with respected to the ones predicted by (3.7). This redshift was observed in many theoretical and experimental papers [122]. Our calculations show that the spectral positions of the EOT peaks tend to the values given by Eq. (3.7) as the radius of the pores decreases (see, for example, Fig. 3.28b, blue curve).

Detailed investigation of the EOT effect in MHAs without underlying PhC is actually out of the scope of this thesis. An extensive review to this topic can be found, for example in [122].

Table 3.8. The comparison of the wavelengths of the EOT peak calculated by Eq. (3.7) and obtained by the FDTD method.

Refractive index of the substrate	$\lambda_{\max}$ calculated by (3.7)	$\lambda_{\max}$ observed in 3D FDTD simulations
1	2.6 μm	2.85 μm
1.5	3.9 μm	4.05 μm
2.2	5.72 μm	5.9 μm
3.5	9.1 μm	9.5 μm

3.4. Discussion and conclusions

There are two different physical effects which can lead to the observation of the EOT. In the case of a MHA between two homogeneous media (Section 3.3) an incident plane wave finally couples to an outgoing plane wave. In the case of the MHA lying on top of a PhC an incident wave couples to one of the PhC eigenmodes. Moreover, if this eigenmode is a TM eigenmode a polarization conversion is observed and the excited mode is localized within a subwavelength distance below the metal. In both cases a dipole-like standing wave mode plays a role of a "mediator" helping to transfer the EM energy through the subwavelength holes. We have seen in the section 3.3 that this dipole-like pattern appears for all wavelengths (at least within the examined spectral range) and its structure is defined by the geometry of the hole array. To be more precise, the size of each dipole is defined by the diameter of the holes the while dipole-to-dipole distance is defined by the period of the lattice.

In the case of MHA-PhC structures the strong coupling to TM modes is possible *only* due to the existence of this dipole-like standing wave pattern. In contrast to single MHAs the coupling condition is defined not by the period of the lattice, but by the frequency of corresponding PhC eigenmode. As a result, the spectral positions of the reflection dips (dips 1 and 3 in section 3.2) can be shifted within a large range by changing the parameters of the PhC, e.g. the radius of the pores or the refractive index of the background material. The excited TM modes are localized within a subwavelength distance below the MHA having the maximal field amplitudes just below the gold. This localization is due to the fact that the amplitude of the E_y-component is high only in the vicinity of the gold and tends to zero as distance from the gold increases. In addition, the EM energy from the excited TM mode cannot decouple to propagating waves because the electric field is polarized parallel to the propagating direction. Since the coupling to TM modes takes place only in the vicinity of the gold (where the E_y field is high), the depth of the pores does not influence the coupling efficiency significantly. We have shown that for a pore depth of 2.5 μm the coupling is still very efficient. The reflection dips are still pronounced even for a pore depth of 1.5 μm which is more than 4 times smaller than the wavelength corresponding to the dip 3 minimum.

It is interesting to discuss the differences between the coupling to the lowest (dip 3) and higher (dip 1) dipole modes. Apparently, the dip 3 is always broader and always deeper than dip 1. We can explain this by considering the E_y field patterns of the corresponding PhC modes. For the lowest mode (see for example Figs. 3.8c and 3.8d) each pore is "surrounded" by only one dipole which is oriented along the polarization direction of the incident wave. This picture corresponds to the wavelength-independent dipole-like pattern appearing in the vicinity of a stand-alone MHA (see Fig. 3.29d). Therefore, no redistribution of the field is required for the coupling to lowest dipole TM mode of a PhC. In the case of a higher dipole mode (see Figs. 3.8a and 3.8b) the field pattern is more complicated: there are several dipoles "surrounding" each hole, and there is no direct correspondence to the dipole-like pattern of the stand-alone MHA. That is the reason why the coupling efficiency to the higher mode is lower and the dip 1 is never as deep as dip 3. For the same reason the steady-state times (subsection 3.2.8) are highest for dip 1. In addition, the dip 1 disappears (subsection 3.2.8) if the structure is not large enough in the lateral directions.

In the subsections 3.2.5 and 3.2.7 we have seen that the spectral positions of the minima of the dips 1 and 3 are always slightly (~2-4%) redshifted with respect to the positions of the corresponding eigenmodes calculated by the 2D PWEM. To explain this shift we want to remind that in FDTD model the refractive index is defined only at discrete points of the computational grid. An abrupt change of the refractive index (e.g. on a wall of a pore) from 3.2 to 1 is simulated in the FullWAVE with the help of some transition interlayer having a refractive index between the two values. This makes the radii of the pores a bit smaller than the value given. As it was shown in the subsection 3.2.5, a decrease of the pores radius results in a redshift of the PhC eigenmodes. Thus, the small mismatch between the FDTD and PWEM calculation might appear because the radii of the pores are slightly smaller than predefined. Another possible reason for the mismatch between PWEM and FDTD results is the finiteness of the structure in y-direction. PWEM calculations are two dimensional implying that the structure is infinitely large in y-direction, i.e. that the pores are infinitely deep. In the FDTD model the pores have the depth of 4 μm and less.

Calculated transmission efficiencies of the MHA-PhC structures are lying between 180% and 230% depending on the particular parameters of a structure. It is necessary to note that at the wavelength where the TM PhC modes are excited (dips 1 and 3) a high absorption (up to 40%) is observed. This is because the EM energy coupled to TM modes is localized below the gold. Therefore, the photons "stay" longer in the vicinity of the gold. We believe that dissipation of the EM energy by the gold is the main factor limiting the transmission efficiency in MHA-PhC structures.

We have estimated the polarization conversion quantitatively by calculating average density of the electric field components below the gold (subsection 3.2.9) at the wavelengths corresponding to the dips 1 and 3. The main conclusion: the energy density carried by the E_y component is an order of magnitude higher than the energy carried by the electric field having the same polarization as in the incident wave.

In MHA-PhC structures a TE mode of the PhC can be also excited by the wave incident normally onto the MHA (dip 2 in section 3.2). In this case, the electric field in the excited mode retains the polarization of the source. Since the electric field is perpendicular to the propagation direction, the EM energy can decouple from the excited mode into propagating outgoing wave. In addition, TE modes are excited in the bulk of the PhC and have the maximal field strength in the middle of the pores (Table 3.4, diagram "f"). This makes the reflection dip 2 very sensitive to the depth of the pores. The decrease of the depth of the pores from 4 μm to 2.5 μm results in the blueshift and broadening of the dip 2. Further decrease of the depth to 1.5 μm eliminates the dip 2 totally. Actually, the excitation of a PhC TE mode *does not require* the metal layer. Coupling to TE modes is observed also for a PhC without metal on top (Fig. 3.20). The gold makes the reflection dip more pronounced by increasing the reflection of non-resonant wavelengths.

We have explained the coupling processes which appear in MHA-PhC structures without involving surface plasmons. The appearance of the standing dipole-like mode in the vicinity of the gold was attributed to the interference between the incident wave and diffracted at the holes waves. We have shown (see Fig. 3.14) that the dipole-like pattern is the only configuration of EM field which satisfies two requirements: (i) in the vicinity of the gold the electric field is polarized normally to the gold-dielectric interface and (ii) within the holes the electric field is polarized mostly in the same direction as in the incident wave. Within this model it does not matter whether the metal is a real metal or a perfect conductor – the dipole-like surface mode would be excited in both cases.

The coupling of light to PhC TM modes has several potential applications. First of all, resonant polarization conversion which leads to appearance of the strong electric field polarized parallel to the pores axis can be used to improve the efficiency of quantum well infrared photodetectors (QWIPs). In such PhC QWIPs the dark current should be lower then in conventional QWIPs due to lower volume of the active region, at the same time, the electromagnetic wave is highly polarized normal to the quantum wells, the energy is concentrated mostly within the active region, and the "dwell time" of the photons is increased due to the resonant nature of the effect.

The reflectance from the MHA-PhC structures at dip 3 minima could be as small as 1%. This could be utilized for narrow-band anti-reflection coatings or transparent electrical contacts.

The MHA-PhC structures have a great potential to be utilized in integrated photonics devices. At reflection dips 1 and 3 a plane wave coming from "infinity" couples to a planar PhC modes. We have shown that the density of EM energy trapped within a subwavelength distance below the metal could be an order of magnitude higher than the energy density of the incident wave.

From a fundamental point of view, the examined structures represent an interesting type of optical resonator. The "Encyclopedia of Laser Physics and Technology" [130] gives the following definition of an optical resonator: "An optical resonator (or resonant optical cavity) is an arrangement of optical components which allows a beam of light to circulate in a closed path. Such resonators can be made in very different forms." Usually, the confinement of light in optical resonators is achieved by formation of standing waves due to multiple reflections as, for instance, in Fabry-Perot or whispering-gallery resonators. Vertical confinement of light in MHA-PhC structures is achieved without multiple reflections. The light is confined within the vicinity of the metal because the surface dipole-like mode exists only there.

3.5. Open questions and future work

The results presented in this Chapter raised a couple of interesting questions for future work.

It is important to perform an experimental research confirming the EOT and polarization conversion in MHA-PhC structures. All simulations consider to some degree idealized structures. Some idealizations have more effect, some less: only careful experiment can make us sure that the model chosen describes an effect well.

At the time of the publication of this thesis, an experiment was in a preparatory stage. It is planned to perform transmission and reflection measurements in mm-wave region on structures similar to those investigated in section 3.2, but scaled-up by a factor of 1000. We have chosen a machinable ceramic material called Macor (n=2.5) as a dielectric material. The hexagonal hole arrays with period a=3 mm and with two different radii, r=0.9 mm and r=0.6 mm were drilled in the Macor plates with dimensions: 78x78x7 mm^3. A photo of a Macor plate with holes is shown in Fig. 3.32. The plates will be then covered with a thin metal foil and holes in the metal foil will be superimposed with the holes in a Macor plate. We expect to observe a dip in reflection which should correspond to the dip 3 in our calculations. For the plate with the holes radius of 0.9 mm the dip 3 is supposed to appear at the wavelength of 5.4 mm.

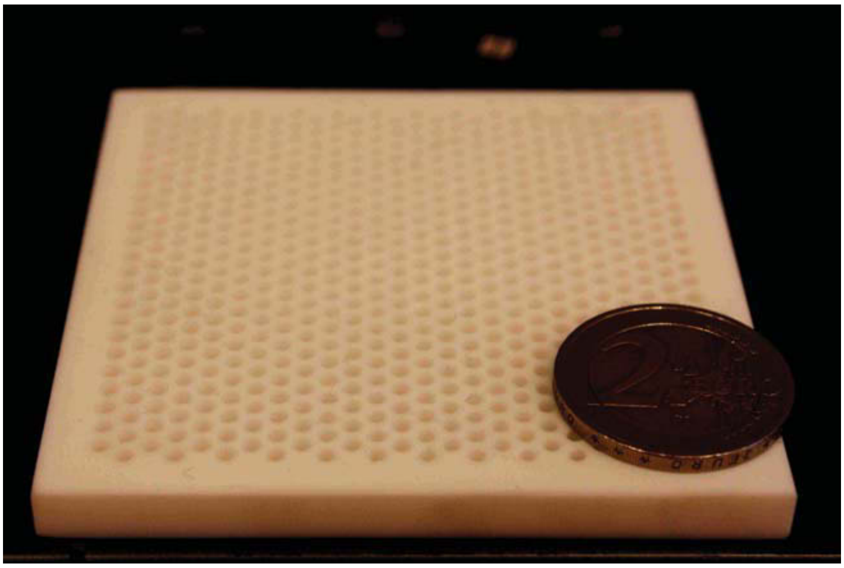

Fig. 3.32. A plate of machinable ceramic material Macor with hexagonal array of holes. After covering of the plate with a thin metal foil and superimposing the holes in metal with the holes in the plate transmission and reflection will be measured.

Of particular interest in our opinion is the influence of the angle of incidence on the coupling processes. This is very important for some application of the MHA-PhC systems, for instance in QWIPs.

It might be interesting to perform a similar analysis as was done in this Chapter for the structures with a square lattice of holes. Dipole modes are also eigenmodes of the square-lattice PhCs so similar effects are expected to appear.

Another interesting question is whether it is possible to achieve a conversion of the wavevector direction? If the EM energy coupled to a TM mode (which is trapped below the gold) could be forced to propagate in the plane of periodicity then such system would be a perfect coupler for planar silicon photonics.

One of the possible directions of further investigations could be an "upgrade" of the model. For instance a second gold layer (with or without holes) put at some distance below the first gold layer could improve the cavity characteristics of the structure. First simulations in this direction showed that the energy trapped in the excited TM mode can be increased at least by a factor of 2 if a homogeneous gold layer without holes is placed below the PhC.

In all simulations presented here a plane wave excitation was used. It might be interesting to investigate the coupling between an optical fiber and MHA-PhC structure.

References

---

[1] M. Born, E. Wolf, "*Principles of Optics*", Second (Revised) Edition, Pergamon press, (1964)

[2] K. Sakoda, "*Optical properties of Photonic crystals*", Springer-Verlag, Berlin (2001)

[3] E. Yablonovich, "Inhibited spontaneous emission in solid-state physics and electronics" Phys Rev. Lett. **58,** 2059 (1987)

[4] S. John "Strong localization of photons in certain disordered dielectric superlattices" Phys. Rev. Lett. **58**, 2486 (1987)

[5] E. Yablonovich, T. Gmitter, "Photonic band structure: the face-centered-cubic case" Phys. Rev. Lett. **63**, 1950 (1989)

[6] S. John, R. Rangarajan, "Optimal structures for classical wave localization: an alternative to the ioffe-regel criterion" Phys. Rev. B. **38,** 10104 (1988)

[7] E. N. Economou, A. Zdetsis, "Classical wave propagation in periodic structures" Phys. Rev. B. **58**, 1334 (1989)

[8] K. M. Ho, C. T. Chan, C. M. Soukoulis, "Existence of a photonic band gap in periodic dielectric structure" Phys Rev. Lett. **65**, 3152 (1990)

[9] Z. Shang, S. Satpathy, "Electromagnetic wave propagation in periodic structures: Bloch wave solutions of Maxwell's equations" Phys Rev. Lett. **65**, 2650 (1990)

[10] K. M. Leung, Y. F. Liu, "Full vector-wave calculation of photonic band structures in face-centered-cubic dielectric media" Phys Rev. Lett. **65**, 2646 (1990)

[11] E. Yablonovich "Photonic band gap materials" J. Opt. Soc. Am. B, **10**, 283 (1993)

[12] E. Yablonovich, T. J. Gmitter, K. M. Leung, "Photonic band structure: the face-centered-cubic case employing nonspherical atoms" Phys Rev. Lett. **67,** 2295 (1991)

[13] K.M. Ho, C.T. Chan, C.M. Soukoulis, R. Biswas, M. Sigalas, "Photonic band gaps in three dimensions: New layer-by-layer periodic structures " Solid State Commun. **89,** 413 (1994)

[14] E. Ozbay, G. Tuttle, E. Michel et. al. "Micromachined millimeter-wave photonic band-gap crystals" Appl. Phys. Lett **64,** 2059 (1994)

[15] E. Ozbay, A. Abeyta, G. Tuttle, K.M. Ho et. al. "Measurement of three-dimensional photonic band gap in a crystal structure made of dielectric rods" Phys. Rev. B. **50,** 1945 (1994)

[16] M. Plihal, A.A. Maradudin, "Photonic band structure of two-dimensional systems: The triangular lattice" Phys. Rev. B. **44**, 8565 (1991)

[17] P. R. Villeneuve, M. Piche, "Photonic band gaps in two-dimensional square and hexagonal lattices" Phys. Rev. B. **46**, 4969 (1992)

[18] P. R. Villeneuve, M. Piche, "Photonic band gaps in two-dimensional square lattice: square and circular rods" Phys. Rev. B. **46**, 4969 (1992)

[19] R. D. Mearde, K. D. Brommer, A. M. Rappe, J. D. Joannopoulos, "Existence of a photonic band gap in two dimensions" Appl. Phys. Lett. **61**, 495 (1992)

[20] S.L. McCall, P.M. Platzman, R. Dalichaouch, D. Smith, S. Schultz, "Microwave propagation in two-dimensional dielectric lattices" Phys. Rev. Lett. **67,** 2017 (1991)

[21] E. Yablonovich, T. J. Gmitter, R. D. Meade, A. M. Rappe, K. D. Brommer, J.D. Joannopoulos, " Donor and acceptor modes in photonic band structure " Phys. Rev. Lett. **67**, 3380 (1991)

[22] R. D. Meade, A. Devenyi, J. D. Joannopoulos, O. L. Alerhand, D. A. Smith, K. Kash, "Novel applications of photonic band gap materials: low-loss bends and high Q cavities" J. Appl. Phys. **75**, 4753 (1994)

[23] A. Mekis, J. C. Chen, I. Kurland, S. Fan, P. R. Villeneuve, J. D. Joannopoulos, "High transmission through sharp bends in photonic crystal waveguides" Phys. Rev. Lett. **77**, 3787 (1996)

[24] S. Y. Lin, E. Chow, V. Hietala, P. R. Villeneuve, J. D. Joannopoulos, "Experimental demonstration of guiding and bending of electromagnetic waves in a photonic crystal" Science **282**, 274 (1998)

[25] M. Loncar, D. Nedeljkovich, T. Doll, J. Vuckovic, A. Scherer, T. P. Pearsall, "Waveguiding in planar photonic crystals" Appl. Phys. Lett. **77**, 1937 (2000)

[26] Y. Akahane, T. Asano, B.-S. Song, S. Noda, " Fine-tuned high-Q photonic-crystal nanocavity" Opt. Exp. **13**, 1202 (2005)

[27] O. Painter, R. K. Lee, A. Scherer, A. Yariv, J. D. O'Brien, P. D. Dapkus, I. Kim, "Two-Dimensional Photonic Band-Gap Defect Mode Laser " Science **284**, 1819 (1999)

[28] F. Couny, et. al. "Visualizing the photonic band gap in hollow core photonic crystal fibers" Opt. Exp. **13**, 558 (2005)

[29] C. Chen, A. Laronche, G. Bouwmans, L. Bigot, Y. Quiquempois, J. Albert, "Sensitivity of photonic crystal fiber modes to temperature, strain and external refractive index" Opt. Express **16**, 9645 (2008)

[30] W. J. Bock, J. Chen, T. Eftimov, W. Urbanczyk, "A photonic crystal fiber sensor for pressure measurements" IEEE Trans. Instrum. Meas. **55** 1119 (2006)

[31] D. Monzon-Hernandez, V. P. Minkovich, J. Villatoro, M. P. Kreuzer, G. Badenes, "Photonic crystal fiber microtaper supporting two selective higher-order modes with high sensitivity to gas molecules" Appl. Phys. Lett. **93** 081106 (2008)

[32] M. Cho, J. Kim, H. Park, Y. Han, K. Moon, E. Jung, H. Han, "Highly birefringent terahertz polarization maintaining plastic photonic crystal fibers" Opt. Express **16**, 7 (2008)

[33] G. Ren, Y. Gong, P. Shum, X. Yu, J. Hu, G. Wang, M. O. L. Chuen, V. Paulose, "Low-loss air-core polarization maintaining terahertz fiber" Opt. Express **16**, 13593 (2008)

[34] S. T. Huntington, B. C. Gibson, J. Canning, K. Digweed-Lyytikainen, J. D. Love, V. Steblina, "A fractal-based fibre for ultra-high throughput optical probes" Opt. Express **15**, 2468 (2007)

[35] H. Y. Choi, S. Y. Ryu, J. Na, B. H. Lee, I. B. Sohn, Y. C. Noh, J. Lee, "Single-body lensed photonic crystal fibers as side-viewing probes for optical imaging systems" Opt. Lett. **33**, 34 (2008)

[36] J. Limpert, O. Schmidt, J. Rothhardt, F. Roser, T. Schreiber, A. Tunnermann, S. Ermeneux, P. Yvernault, F. Salin, "Extended single-mode photonic crystal fiber lasers" Opt. Express **14**, 2715 2006

[37] F. Sebastien, et. al. "High-power photonic-bandgap fiber laser" Opt. Lett. **33**, 989 (2008)

[38] A. Figotin, Y. A. Godin, I. Vitebsky, "Two-dimensional tunable photonic crystals" Phys. Rev. B **57**, 2841 (1998)

[39] S.W. Leonard et. al. "Tunable two-dimensional photonic crystal using liquid-crystal infiltration" Phys. Rev. B **61**, 2389 (2000)

[40] S.W. Leonard, H. M. van Driel, J. Schilling, R. B. Wehrspohn, " Ultrafast band-edge tuning of a two-dimensional silicon photonic crystal via free-carrier injection" Phys. Rev. B **66**, 161102 (2002)

[41] A. D. Bristow, et. al. " Ultrafast nonlinear tuning of the reflection properties of AlGaAs photonic crystal waveguides by two-photon absorption" J. Appl. Phys. **96**, 4729 (2004)

[42] S. Kim, V. Gopalan, "Strain-tunable photonic band gap crystals" Appl. Phys. Lett. **78**, 3015 (2001)

[43] S. D. Cheng, R. Biswas, E. Ozbay, S. McCalmont, G. Tuttle, K. M. Ho, "Optimized dipole antennas on photonic band gap crystals" Appl. Phys. Lett. **67**, 3399 (1995)

[44] B. Temelkuran, M. Bayindir, E. Ozbay, R. Biswas, M. M. Sigalas, G. Tuttle, K. M. Ho, "Photonic crystal-based resonant antenna with a very high directivity" J. Appl. Phys. 87, 603 (2000)

---

[45] H. Kosaka, T. Kawashima, A. Tomita, N. Notomi, T. Tamamura, T. Sato, S. Kawakami, "Superprism phenomena in photonic crystals" Phys. Rev. B **58**, 10096 (1998)

[46] E. Cubukcu, K. Aydin, E. Ozbay, S. Foteinopoulou, C. M., "Subwavelength Resolution in a Two-Dimensional Photonic-Crystal-Based Superlens" Phys. Rev. Lett. **91**, 207401 (2003)

[47] T. Matsumoto, S. Fujita, and T. Baba, "Wavelength demultiplexer consisting of Photonic crystal superprism and superlens" Opt. Exp. **13**, 10768 (2005)

[48] A. Glushko, L. Karachevtseva, "PBG properties of three-component 2D photonic crystals", Phot. Nanostr. Fund. Apl., 4, 141-145 (2006)

[49] K. S. Yee, "Numerical solution of initial boundary value problems involving Maxwell's equations in isotropic media", IEEE Trans. Antenn. Propag., **14**, 302 (1966)

[50] A. Taflove and S. C. Hagness, "*Computational Electrodynamics: The Finite-Difference Time-Domain Method", 2nd ed.* Norwood, MA: Artech House, 2000

[51] www.rsoftdesign.com

[52] Z. Jaksic, M. Maksimovich, O. Jaksic, et. al. "*Fabrication-induced disorder in structures for nanophotonics*" Microelectr. Eng, **83**, 1792, (2006)

[53] V.A. Tolmachev, T.S. Perova, J.A. Pilyugina, R.A. Moore "Experimental evidence of photonic band gap extension for disordered 1D photonic crystals based on Si" Opt. Comm. **259,** 104 (2006)

[54] H. Li, H. Chen, X. Qiu "Band gap extension of disordered 1D binary photonic crystals" Physica B **279**, 164 (2000)

[55] M.A. Kaliteevski, D.M. Beggs, S. Brand, R.A. Abram, V.V. Nikolaev "Statistics of the egenmodes and optical properies of one-dimensional disordered photonic crystals", Phys. Rev. E **73**, 056616 (2006)

[56] M.A. Kaliteevski, D.M. Beggs, S. Brand, R.A. Abram, V.V. Nikolaev "Stability of the photonic band gap in the presence of disorder" Phys. Rev. B **73**, 033106 (2006)

[57] H. Sami Sozuer and K. Sevim "Robustness of one-dimensional photonic band gaps under random variations of geometrical parameters" Phys. Rev. B **72**, 195101 (2005)

[58] M.A. Kaliteevski, J. Manzanares Martinez, D. Cassagne, J.P. Albert "Disorder-induced modification of the transmission of light in a two-dimensional photonic crystal" Phys. Rev. B **66**, 113101 (2002)

[59] D.M. Beggs, M.A. Kaliteevski, S. Brand et. al. "Disorder induced modification of reflection and transmission spectra of a two-dimensional photonic crystal with an incomplete band gap" J. Phys.: Condens. Matter **17**, 4049 (2005)

[60] M.M. Sigalas, C.M. Soukoulis, C.-T. Chan, and D. Turner "Localization of electromagnetic waves in two-dimensional disordered systems" Phys. Rev. B **53**, 8340 (1996)

[61] E. Lidorikis, M.M. Sigalas, E.N. Economou, C.M. Soukoulis "Gap deformation and classical wave localization in disordered two-dimensional photonic band gap materials" Phys. Rev. B **61**, 13458 (2000).

[62] A.A. Asatryan, P.A. Robinson, L.C. Botten et. al. "Effects of disorder on wave propagation in two-dimensional photonic crystals" Phys. Rev. E **60,** 6118 (1999)

[63] A.A. Asatryan, P.A. Robinson, L.C. Botten et. al. "Effects of geometric and refractive index disorder on wave propagation in two-dimensional photonic crystals" Phys. Rev. E **62**, 5771 (2000)

[64] H.-Y. Ryu, J.-Ki Hwand, Y.-H. Lee "Effect of size nonuniformities on the band gap of two-dimensional photonic crystals" Phys. Rev. B **59** 5463 (1999).

[65] Zhi-Yuan Li, X. Zhang, and Zhao-Qing Zhang "Disordered photonic crystals understood by a perturbation formalism" Phys. Rev. B **61** 15738 (2000)

[66] R. Meisels, F. Kuchar "Density-of-states and wave propagation in two-dimensional photonic crystals with positional disorder" J. Opt. A: Pure Appl. Opt., **9**, 396 (2007)

[67] W.R. Frei and H.T. Johnson "Finite-element analysis of disorder effects in photonic crystals" Phys. Rev. B **70** 165116 (2004)

---

[68] M. Bayindir, E. Cubukcu, I. Bulu et. al. "Photonic band gaps, defect characteristics, and waveguiding in two-dimensional disordered dielectric and metallic photonic crystals" Phys. Rev. B **64** 195113 (2001)
[69] H. Li, B. Cheng, D. Zhang "Two-dimensional disordered photonic crystals with an average periodic lattice" Phys. Rev. B **56**, 10734 (1997)
[70] Sigalas M. M., Soukoulis C. M., Chan C. T., Biswas R., Ho K. M., "Effect of disorder on photonic band gaps" Phys. Rev. B **59**, 12767 (1999)
[71] Li Z.-Y., Zhang Z.-Q., "Fragility of photonic band gaps in inverse-opal photonic crystals" Phys. Rev. B **62**, 1516 (2000)
[72] Vlasov Yu. A., Kaliteevski M. A., Nikolaev V. V., " Different regimes of light localization in a disordered photonic crystal" Phys. Rev. B **60**, 1555 (1999)
[73] Stoytchev M., Genack A. Z., " Microwave transmission through a periodic three-dimensional metal-wire network containing random scatterers" Phys. Rev. B **55**, 8617 (1997)
[74] Freilikher V. D., Liansky B. A., Yurkevich I. V., Maradudin A. A., McGurn A. R., Phys. Rev. E **51**, 6301 (1995)
[75] Vlasov Yu. A., Astratov V. N., Baryshev A. V., Kaplyanskii A. A., Karimov O. Z., Limonov M. F., " Manifestation of intrinsic defects in optical properties of self-organized opal photonic crystals" Phys. Rev. E **61**, 5784 (2000)
[76] Astratov V. N., Adawi A. M., Fricker S., Skolnick M. S., Whittaker D. M., Pusey P. N., " Interplay of order and disorder in the optical properties of opal photonic crystals " Phys. Rev. B **66**, 165215 (2002)
[77] Galisteo-Lopez J. F., Palacios-Lidon E., Castillo-Martinez E., Lopez C., " Optical study of the pseudogap in thickness and orientation controlled artificial opals " Phys. Rev. B **68**, 115109 (2003)
[78] Braginsky L., Shklover V., "Light propagation in an imperfect photonic crystal" Phys. Rev. B **73**, 085107 (2006)
[79] B.C. Gupta, Z. Ye "Disorder effect on imaging of a negative refractive lens made by arrays of dielectric cylinders" J. Appl. Phys. **94** 2173 (2003)
[80] X. Wang and K. Kempa " Effects of disorder on subwavelength lensing in two-dimensional photonic crystal slabs" Phys. Rev. B **71**, 085101 (2005)
[81] A. Rodriquez, M. Ibanescu, J.D. Joannopoulos, S.G. Johnson "Disorder-immune confinement of light in photonic-crystal cavities" Opt. Lett. **30** 3192 (2005)
[82] E. Kuramochi, S.Hughes, A. Shinya, M. Notomi "Si-based photonic crystal components: relationship between performance and structural disorder" NTT Tech. Rev. **3**(12) 69 2005
[83] K.-C. Kwan, X. Zhang, Z.-Q. Zhang, C. T. Chan "Effects due to disorder on photonic crystal-based waveguides" Appl. Phys. Lett. **82** 4414 (2003)
[84]T.N. Langtry, L.C. Botten, A.A. Asatryan, M.A. Byrne, A. Bourgeois "Localization and disorder in the design of 2D photonic crystal devices" ANZIAM J., 45, c744-758 (2004)
[85] C.G. Poulton, C. Koos, M. Muller, F. Glocker et. al. "Sidewall roughness and deformations in high index-contrast waveguides and photonic crystals" Proc. 17th Annual Meeting of the IEEE Lasers and Electro-Optics Society (LEOS 2004), Puerto Rico, USA; November 2004.
[86] D. Gerache, L.C. Andriani "Low-loss guided modes in photonic crystal waveguides" Opt. Exp. **13**, 4939 (2005)
[87] M. Notomi, A. Shinya, S. Mitsugi, E. Kuramochi, H.-Y. Ryu "Waveguides, resonators and their coupled elements in photonic crystal slabs" Opt. Express **12**, 1551 (2004)
[88] O. Glushko, R. Meisels, F. Kuchar, R. Danzer, "Numerical and experimental investigations of surface roughness in 1D photonic crystals", J. Phys. Cond. Matt. **20**, 454220 (2008)
[89] O. Glushko, R. Meisels, F. Kuchar, "Simulations of wave propagation and disorder in 3D non-close-packed colloidal photonic crystals with low refractive index contrast", Opt. Exp. **18**, 7101 (2010)

---

[90] Stefanou N, Yannopapas V and Modinos A, Comp. Phys. Comm. **132,** 189 (2000)

[91] N. Stefanou, V. Yannopapas, A. Modinos, "MULTEM 2: A new version of the program for transmission and band-structure calculations of photonic crystals," Comp. Phys. Comm. **132,** 189-196 (2000)

[92] W. L. Vos, M. Megens, C. M van Kats and P. Bösecke, "Transmission and diffraction by photonic colloidal crystals," J. Phys.: Condens. Matter **8,** 9503-9507 (1996)

[93] H. Míguez, F. Meseguer, C. López, A. Mifsud, J. S. Moya, and L. Vázquez, "Evidence of FCC Crystallization of SiO2 Nanospheres," Langmuir, **13**, 6009–6011 (1997)

[94] K. Busch, S. John, "Photonic band gap formation in certain self-organizing systems," Phys. Rev. E **58**, 3896 - 3908 (1998)

[95] G. Subramania, K. Constant, R. Biswas, M. M. Sigalas, K.-M. Ho, "Optical photonic crystals fabricated from colloidal systems," Appl. Phys. Lett. **74**, 3933 (1999)

[96] G. S. Lozano, L. A. Dorado, R. A. Depine, H. Migues, "Towards a full understanding of the growth dynamics and optical response of self-assembled photonic colloidal crystal films," J. Mater. Chem. **19**, 185-190 (2009)

[97] M. Bardosova, R.H. Tredgold, "Ordered layers of monodispersive colloids," J. Mater. Chem **12,** 2835-2842 (2002)

[98] M. Bardosova, P. Hodge, L. Pach, M.E. Pemble, V. Smatko, R.H. Tredgold, D. Whitehead, "Synthetic opals made by the Langmuir-Blodgett method," Thin Solid Films **473**, 276-279 (2003)

[99] H. Nakamura, M. Ichii, "Effects of medium composition on optical properties and microstructures of non-close-packed colloidal crystalline arrays," Colloid. Polym. Sci. **285,** 833-837 (2007)

[100] Yu. Iwayama, J. Yamanaka, Yo. Takiguchi, M. Takasaka, K. Ito, T. Shinohara, T. Sawada, M. Yonese, "Optically tunable gelled photonic crystal covering almost the entire visible light wavelength region," Langmuir **19,** 977-980 (2003)

[101] A. Toyotama, J. Yamanaka, M. Yonese, T. Sawada, F, Uchida, " Thermally Driven Unidirectional Crystallization of Charged Colloidal Silica," J. Am. Chem. Soc.*,* **129,** 3044 -3045, 2007

[102] B.V.R Tata, S. S. Jena, "Ordering dynamics and phase transitions in charged colloids," Sol. State Comm. **139**, 562-580 (2006)

[103] R. Goldberg, H. J. Schope, "Opaline hydrogels: polycrystalline body-centered-cubic bulk material with an in situ variable lattice constant," Chem. Mater., 19, 6095–6100 (2007)

[104] J. F. Bertone, P. Jiang, K. S. Hwang, D. M. Mittleman, V. L. Colvin, "Thickness dependence of the optical properties of ordered silica-air and air-polymer photonic crystals," Phys. Rev. Lett. **83**, 300-303 (1999)

[105] F. Galisteo-Lopez, F. Garcia-Santamara, D. Golmayo, B.H. Juarez, C. Lopez, E. Palacios-Lidon, "Design of photonic bands for opal-based photonic crystals," Phot. Nanostr.: Fund. Appl. **2** 117–125 (2004)

[106] T.W. Ebessen, H.J. Lezec, H.F. Ghaemy, T. Thio, and P.A. Wolf, "Extraordinary optical transmission through sub-wavelength hole arrays", Nature, **391**, 667 (1998)

[107] U. Schröter and D. Heitmann, "Surface-plasmon-enhanced transmission through metallic gratings", Phys. Rev. B, **58**, 15419 (1998)

[108] L. Martin-Moreno, F. J. Garcia-Vidal, H. J. Lezec, K. M. Pellerin, T. Thio, J. B. Pendry, and T. W. Ebbesen, "Theory of Extraordinary Optical Transmission through Subwavelength Hole Arrays" Phys. Rev. Lett. **86**, 1114 (2001)

[109] L. Martin-Moreno, F. J. Garcia-Vidal, "Optical transmission through circular hole arrays in optically thick metal films", Opt. Exp. **12**, 3619 (2004)

[110] H.J. Lezec and T. Thio, "Diffracted evanescent wave model for enhanced and suppressed optical transmission through subwavelength hole arrays", Opt. Exp. **12**, 3629, (2004)

---

[111] B. Hou, Z. Hong Hang, W. Wen, C. T. Chan, and P. Sheng, "Microwave transmission through metallic hole arrays: Surface electric field measurements", Appl. Phys. Lett., **89**, 131917, (2006)

[112] F. Medina, J.A. Ruiz-Cruz, F. Mesa, J.M. Rebollar, J.R. Montejo-Garai, and R. Marques, "Experimental verification of extraordinary transmission without surface plasmons", Appl. Phys. Lett., **95**, 071102 (2009)

[113] N. Papasimakis, V. A. Fedotov, A. S. Schwanecke, N. I. Zheludev, and F. J. Garcia de Abajo, Appl. Phys. Lett., **91**, 081503, (2007)

[114] F. Miyamaru, M. Hangyo, "Finite size effect of transmission property for metal hole arrays in subterahertz region" Appl. Phys. Lett. **84**, 2742 (2003)

[115] J. Gomez Rivas, C. Schotsch, P. Haring Bolivar, H. Kurz, "Enhanced transmission of THz radiation through subwavelength holes" Phys. Rev. B **68**, 201306 (2003)

[116] R. Ortuno, C. Garcia-Meca, F. J. Rodriguez-Fortuno, J. Marti, Alejandro Martinez, "Role of surface plasmon polaritons on optical transmission through double layer metallic hole arrays" Phys. Rev. B, **79**, 075425 (2009)

[117] Jiang-Yan Li, Yi-Lei Hua, Jin-Xin Fu, Zhi-Yuan Li, "Influence of hole geometry and lattice constant on extraordinary optical transmission through subwavelength hole arrays in metal films" J. Appl. Phys. **107**, 073101 (2010)

[118] C. Genet and T.W Ebessen, Light in tiny holes, Nature, **445**, 39 (2007)

[119] M. M. J. Treacy, "Dynamical diffraction in metallic optical gratings," Appl. Phys. Lett. 75, 606-608, 1999

[120] F.J. Garcia de Abajo, "Light scattering by particle and hole arrays", Rev. Mod. Phys., **79**, 1267 (2007)

[121] J. Weiner, "The physics of light transmission through subwavelength apertures and aperture arrays", Rep. Prog. Phys., **72**, 064401 (2009)

[122] F. J. Garcia-Vidal, L. Martin-Moreno, T.W Ebessen, L. Kuipers, " Light passing through subwavelength apertures" Rev. Mod. Phys. **82**, 729 (2010)

[123] S. Schartner, S. Golka, C. Pfluegl, W. Schrenk, A. M. Andrews, T. Roch, and G. Strasser, "Band structure mapping of photonic crystal intersubband detectors", Appl. Phys. Lett. **89**, 151107 (2006)

[124] S. Schartner, M. Nobile, W. Schrenk, A. M. Andrews, P. Klang, and G. Strasser, "Photocurrent response from photonic crystal defect modes", Opt. Exp., **16**, 4797 (2008)

[125] F. Albert Cotton, *"Chemical Applications of Group Theory"*, 3rd Ed., John Wiley & Sons, 1990, pp 90-91.

[126] J.D. Jackson, "*Classical Electrodynamics*", John Wiley & Sons, New-Jork-London, 1992

[127] Naweed, A., F. Baumann, W. A. Bailey, A. S. Karakashian, and W. D. Goodhue, "Evidence for radiative damping in surface-plasmon-mediated light transmission through perforated conducting films", J. Opt. Soc. Am. B **20**, 2534 (2003)

[128] van der Molen, K. L., F. B. Segerink, N. F. van Hulst, and L. Kuipers, "Influence of hole size on the extraordinary transmission through subwavelength hole arrays", Appl. Phys. Lett. **85**, 4316 (2004)

[129] F. Yang, J.R. Sambles, G.W. Bradberry, "Long-range surface modes supported by thin films", Phys. Rev. B **44**, 5855 (1991)

[130] http://www.rp-photonics.com/encyclopedia.html

APPENDIX I. The MatLab program code realizing PWEM for 2D triangular lattice PhC with the inclusion of the third component.

The program code starts from the next line:

```
                           %%%%%%%%%%%%%%%%%%%%%%%%%%%%%%%%%%%%%%%%%%%%%%
                           % PLANE-WAVE METHOD FOR 2D PHOTONIC CRYSTALS.%
                           %           THREE-COMPONENT                  %
                           %          TRIANGULAR LATTICE                %
                           %       Developed by Oleksandr Glushko       %
                           %  Any questions?   -->  a_glushko@ukr.net   %
                           %%%%%%%%%%%%%%%%%%%%%%%%%%%%%%%%%%%%%%%%%%%%%%
clear all;
close all;
%Setting initial parameters
m=5;ea=1;eb=11;ei=1;a=2*pi;R=0.43*a;step=0.02;Max=5;TEmax=6;d=0.0*a;kz=0;
edg=1/sqrt(3);lastkp=1/3+edg;
pointnumb=2*lastkp/step; param=1.5; maxomega=0.6;
N=(2*m+1)^2;numb=Max+1;
f1=2*pi*edg*R^2/a^2; fi=2*pi*edg*((R+d)^2-R^2)/a^2;
f2=1-f1-fi;fsh=2*pi*edg*(R+d)^2/a^2;
k0=f1/ea+f2/eb+fi/ei;
b1x=1;b1y=-edg;b2x=0;b2y=2*edg;
%Setting initial parameters
N
disp(f1);
Gx=zeros(1,N);
Gy=zeros(1,N);
l=1;
for i=-m:m
    for j=-m:m
        Gx(l)=i*b1x+j*b2x;Gy(l)=i*b1y+j*b2y;
        l=l+1;
    end
end
Delta=zeros(N);
for i=1:N
    for j=1:N
        Delta(i,j)=sqrt((Gx(i)-Gx(j))^2+(Gy(i)-Gy(j))^2);
    end
end

ke=zeros(N);

for i=1:N
    for j=1:N
        if Delta(i,j)~=0
        ke(i,j)=(1/ea-1/ei)*f1*2*besselj(1,Delta(i,j)*R)/(Delta(i,j)*R)+...
            (1/ei-1/eb)*fsh*2*besselj(1,Delta(i,j)*(R+d))/(Delta(i,j)*(R+d));
        else
            ke(i,j)=k0;
        end
    end
end
clear Delta;
disp('--');
                                     %   Main program

                                      %%%%%%%%%%%%%%%%%%%%%%%%%%%%%%%%%%%%%
                                      %            P- MODES               %
                                      %%%%%%%%%%%%%%%%%%%%%%%%%%%%%%%%%%%%%

                                 %p- MODES 1 GK-curve
kx=0;ky=0;kz=0;
main=zeros(2*N);
kp=[];
band=cell(1,Max);
for ky=0:step:edg
```

```
    for i=1:N
        for j=1:N
        main(i,j)=ke(i,j)*((ky+Gy(j))^2+kz^2);
        main(i,j+N)=-ke(i,j)*(kx+Gx(j))*(ky+Gy(j));
        main(i+N,j)=-ke(i,j)*(kx+Gx(j))*(ky+Gy(j));
        main(i+N,j+N)=ke(i,j)*((kx+Gx(j))^2+kz^2);
        end
    end
eival=sort(eig(main));
eival1=eival((N+1):(N+Max));
kp=[kp,kx+ky];
    for n=1:Max
        if cival1(n)<1c-004
           eival1(n)=0;
        end
    band{n}=[band{n},{[sqrt(eival1(n))]}];

    end
end


                                            %p- MODES 2 KX - curve
disp('-----');
kx=0;ky=edg;
for kx=0:step:1/3
    for i=1:N
        for j=1:N
        main(i,j)=ke(i,j)*((ky+Gy(j))^2+kz^2);
        main(i,j+N)=-ke(i,j)*(kx+Gx(j))*(ky+Gy(j));
        main(i+N,j)=-ke(i,j)*(kx+Gx(j))*(ky+Gy(j));
        main(i+N,j+N)=ke(i,j)*((kx+Gx(j))^2+kz^2);

        end
    end
eival=sort(eig(main));
eival1=eival((N+1):(N+Max));
kp=[kp,kx+ky];
    for n=1:Max
    band{n}=[band{n},{[sqrt(eival1(n))]}];
    end
end

                                                 %p- MODES 3 XG - curve
disp('----------');
kyy=[];
kx=1/3;ky=edg;

while ky>=0
    kyy=[kyy,ky];
    for i=1:N
        for j=1:N
        main(i,j)=ke(i,j)*((ky+Gy(j))^2+kz^2);
        main(i,j+N)=-ke(i,j)*(kx+Gx(j))*(ky+Gy(j));
        main(i+N,j)=-ke(i,j)*(kx+Gx(j))*(ky+Gy(j));
        main(i+N,j+N)=ke(i,j)*((kx+Gx(j))^2+kz^2);
        end
    end
eival=sort(eig(main));
eival1=eival((N+1):(N+Max));
kx=ky*edg;
kp=[kp,2*lastkp-(kx+ky)];
    for n=1:Max
        if eival1(n)<1e-004
           eival1(n)=0;
        end
        band{n}=[band{n},{[sqrt(eival1(n))]}];
    end
if ky<step && ky~=0
    ky=0; kx=0; continue
end
ky=ky-step;
end

xnumb=size(kp);
```

```
for n=1:Max
    for i=1:xnumb(1,2)                    %plotting p-polarized curves
    cur(i)=band{n}{i};
    end
    p_Min(n)=min(cur);
    p_Max(n)=max(cur);
    plot(kp,cur,'k');
    xlim([0 1.8214]);
    hold on
end
disp('*******P-POLARIZATION*******')
for n=1:(Max-1)
    p_gap(n)=p_Min(n+1)-p_Max(n);
    if p_gap(n)>0.001
        disp(p_Max(n));                          %displaying p-gaps edges
        disp(p_Min(n+1));
        disp(p_gap(n));
        disp(n)
    end
end
disp('*******P-POLARIZATION*******')

                                     %%%%%%%%%%%%%%%%%%%%%%%%%%%%%%%%%%%%%
                                     %            S- MODES              %
                                     %%%%%%%%%%%%%%%%%%%%%%%%%%%%%%%%%%%%%

                                          %s- MODES 1 GK-curve
disp('--');

Max=TEmax;
kx=0;ky=0;kz=0;
main=zeros(N);
kp=[];
band=cell(1,TEmax);
for ky=0:step:edg
    for i=1:N
        for j=1:N
        main(i,j)=ke(i,j)*((kx+Gx(j))^2+(ky+Gy(j))^2);

        end
    end
eival=sort(eig(main));
eival1=eival(1:Max);
kp=[kp,kx+ky];
    for n=1:Max
        if eival1(n)<1e-004
           eival1(n)=0;
        end
    band{n}=[band{n},{[sqrt(eival1(n))]}];

    end
end
                                            %s- MODES 2 KX - curve
disp('-----');
kx=0;ky=edg;
for kx=0:step:1/3
    for i=1:N
        for j=1:N
        main(i,j)=ke(i,j)*((kx+Gx(j))^2+(ky+Gy(j))^2);
        end
    end
eival=sort(eig(main));
eival1=eival(1:Max);
kp=[kp,kx+ky];
    for n=1:Max
    band{n}=[band{n},{[sqrt(eival1(n))]}];
    end
end

                                                 %s- MODES 3 XG - curve
disp('----------');
kyy=[];
kx=1/3;ky=edg;
```

```
while ky>=0
    kyy=[kyy,ky];
    for i=1:N
        for j=1:N
        main(i,j)=ke(i,j)*((kx+Gx(j))^2+(ky+Gy(j))^2);
        end
    end
eival=sort(eig(main));
eival1=eival(1:Max);
kx=ky*edg;
kp=[kp,2*lastkp-(kx+ky)];
    for n=1:Max
        if eival1(n)<1e-004
           eival1(n)=0;
        end
        band{n}=[band{n},{[sqrt(eival1(n))]}];
    end
if ky<step && ky~=0
    ky=0; kx=0; continue
end
ky=ky-step;
end

xnumb=size(kp);
for n=1:Max
    for i=1:xnumb(1,2)                     %plotting s-polarized curves
    cur(i)=band{n}{i};
    end
    s_Max(n)=max(cur);
    s_Min(n)=min(cur);
    plot(kp,cur,'--k');
    title('triang','FontSize',10);
    ylabel('a/\lambda','FontSize',16);
    xlabel(texlabel('k_II'));
    set(gca,'XTick',[0,1/3^(1/2),1/3+1/3^(1/2),1.8214],'FontSize',14);
    set(gca,'XTicklabel',{'G','K','X','G'})
    plot(kp,cur,'--k');
    xlim([0 1.8214]);
    hold on
end
disp('*******S-POLARIZATION*******')
for n=1:(Max-1)
    s_gap(n)=s_Min(n+1)-s_Max(n);                %displaying of s-gaps edges
    if s_gap(n)>0.001
        disp('*******')
        disp(s_Max(n));
        disp(s_Min(n+1));
        disp(s_gap(n));
        disp(n)
    end
end
disp('*******S-POLARIZATION*******')
```

%end of the program code

Description of the parameters and variables:

m is the number of reciprocal vectors in one direction, the total number of reciprocal vectors is given by $N = (2\mathrm{m}+1)^2$. In other words, *N* is a plane-wave cut-off value.

ea, eb are the dielectric constants of the media

a is the minimal distance between the centers of nearest neighbor pores (lattice constant)

R is the radius of the pores

d is the thickness of the additional layer (see Fig. 1.14)
ei is the dielectric constant of the additional layer
max is the number of bands that will be calculated
step is the step of evaluation along k_1 and k_2
f is the filling fraction
k0 is the value of $\eta(\vec{G}_{II} - \vec{G}'_{II})$ when $\vec{G}_{II} - \vec{G}'_{II} = 0$
ke is the values of $\eta(\vec{G}_{II} - \vec{G}'_{II})$ when $\vec{G}_{II} - \vec{G}'_{II} \neq 0$
b1x, *b1y*, *b2x*, *b2y* are the components of primitive translation vectors of the reciprocal lattice
Gx, Gy are the components of basis reciprocal vectors
edg is the edge of Brilliuon zone (*edg=1/sqrt(3)* for triangular structure)
main[i,j] is a two-dimensional array which represents the matrix *M* (see Eqs. 1.12 and 1.13)
band{n} is an array containing the calculated values of all eigenfrequencies. For instance, *band{2}* contains the eigenfrequencies of the second dispersion curve.
kx, *ky*, *kz*, *kp* are correspondingly k_1, k_2, k_3, and k_{II}

APPENDIX II. MatLab code for introduction of the random values in an RSoft CAD input file.

```
%%%%%%%%%%%%%%%%%%%%%%%%%%%%%%%%%% Rsoft disorder %%%%%%%%%%%%%%%%%%%%%%%%%%%%%%%%%%%%%%%
%% The propgram for introduction of random magnitudes into Rsoft CAD input file (*.ind)%%
%% Creates new *.ind file%%
%%%%%%%%%%%%%%%%%%%%%%%%%%%%
close all;
clear all;
line='zero';
tab=char(9);
fid=fopen('C:\_Work\Glushko\new_plates\np_2dis0_1_Res300\np_5Lperfect.ind','r+'); % openinng initial file for reading
fidn=fopen('C:\_Work\Glushko\new_plates\np_2dis0_1_Res300\np_5L_2dis0_1_Res300_run2.ind','w+'); % creating new file for writing
while ischar(line)==1
    line=fgetl(fid); %lyne-by-line reading of initial file
    if strcmp(line,[tab,'zscale = Zscale'])==1 % searching for required parameter
        back2=fprintf(fidn,'%s\n',[tab,'zscale = Zscale*',num2str(0.2*rand(1)+1)]); % replacing of original line by the new line with random
value
    else
        if ischar(line)==1
            fprintf(fidn,'%s\r\n',line); % "copying" all the rest lines
        end
    end

end
fclose(fid);
fclose(fidn);
```

APPENDIX III. MULTEM2 input file for 3D colloidal photonic crystals with bcc lattice. [110] propagation direction.

"

```
unit: 3.000000e+14 for omega, 4.774648e+13 for frequency

  KTYPE = 1  KSCAN = 1  KEMB  = 1   LMAX = 4   NCOMP= 1  NUNIT =  7
 ALPHA =    1.000000  BETA =    1.000000  FAB =  70.528800  RMAX =  16.000000
 NP = 500  ZINF =   2.70000000  ZSUP =  3.100000000
  THETA/AK(1) =   0.00000000    FI/AK(2) =   0.00000000   POLAR =S    FEIN =   0.00

Give information for the 'NCOMP' components

   IT  =  2
    NUMED =   1.00000000   0.00000000    EPSMED=   1.76890000   0.00000000
  NPLAN = 2  NLAYER = 1
     S =   0.46188000     MUSPH =   1.00000000   0.00000000    EPSSPH=   2.13160000   0.00000000
xyzDL 0.0  0.0  0.40825
xyzDR 0.0 0.28868 0.40825
     S =   0.46188000     MUSPH =   1.00000000   0.00000000    EPSSPH=   2.13160000   0.00000000
xyzDL 0.0 0.28868 0.40825
xyzDR 0.0 0.0 0.40825
  MUEMBL =   1.00000000   0.00000000    EPSEMBL =   1.76890000   0.00000000
  MUEMBR =   1.00000000   0.00000000    EPSEMBR =   1.76890000   0.00000000
```

"

APPENDIX IV. C++ program code for calculation of the average energy density from a 3D field distribution (vtk-files). Developed by Ronald Meisels.

```
#include<stdio.h>
#include<math.h>
#include<string.h>
#include<stdlib.h>
int main(int argc, char* argv[])
{
int nges;
double sum;
char infilename[280];
char linebuffer[10000]; /* holds one line*/
char dummy[10000];
int nx,ny,nz; /* dimension of array*/
int ix,iy,iz; /*indices*/
double x1,y1,z1; /* initial coordinates*/
double dx,dy,dz; /*spacing*/
double A=3.0;
double Ax,Cx,Cz;
double r=0.01*A;/*hole radius*/
FILE *infile;
FILE *outfile;
FILE *namesfile; /* argc[1] name of file containing name of vtk files */
int iA,iC; /*index of circles*/
int maxn=10; /* maximal index*/
double rcomp; /*radius to compare with*/
double x,y,z;
int numpoints=0;
double fieldval;
int holehit;
double powsum;
Ax=A; Cx=A/2; Cz=A*sqrt(3.0)/2.0;
printf("starting\n");
printf("argv0:%s\n",argv[0]);
printf("argv1:%s\n",argv[1]);
printf("argv2:%s\n",argv[2]);
namesfile = fopen(argv[1],"r");
outfile = fopen(argv[2],"w");
if (namesfile==0){printf("didn't find file with names\n");exit(1);}
if (outfile==0){printf("didn't open output\n");exit(1);}
while(!feof(namesfile))
{
      numpoints=0;
      powsum=0.0;
 fgets(infilename,100,namesfile);
 printf("last char:%d\n",infilename[strlen(infilename)-1]);
 if(infilename[strlen(infilename)-1]<32)infilename[strlen(infilename)-1]=0; /*remove non printing*/
 printf("filename here:%s\n",infilename);
 if (feof(namesfile)) break;
 infile=fopen(infilename,"r");
 if(!infile) {printf("bad filename: >>%s<<\n",infilename);break;}
 printf("starting to read\n");
 do{
 fgets(linebuffer,1000,infile);
 printf("buffer:%s\n",linebuffer);
 }while(strncmp(linebuffer,"DIMENSIONS",10)); /*until line with DIMENSIONS*/
  printf("before sscanf\n");
 sscanf(linebuffer,"%s%d%d%d",dummy,&nx,&ny,&nz);
 printf("after sscanf\n");
 printf("dummy>>%s<< dimensions, nx=%d, ny=%d, nz=%d\n",dummy,nx,ny,nz);
 do{
  fgets(linebuffer,1000,infile);
 }while(strncmp(linebuffer,"ORIGIN",6)); /*until line with DIMENSIONS*/
 sscanf(linebuffer,"%s%lf %lf %lf",dummy, &x1,&y1,&z1);
  printf("dummy>>%s<< oigin, x1=%lf, y1=%lf, z1=%lf\n",dummy,x1,y1,z1);
 do{
  fgets(linebuffer,1000,infile);
```

```
 }while(strncmp(linebuffer,"SPACING",7)); /*until line with DIMENSIONS*/
 sscanf(linebuffer,"%s%lf %lf %lf",dummy, &dx,&dy,&dz);
 do{
   fgets(linebuffer,1000,infile);
 }while(strncmp(linebuffer,"POINT_DATA",10)); /*until line with DIMENSIONS*/
 sscanf(linebuffer,"%s %d", dummy, &nges);
   do{
 fgets(linebuffer,1000,infile);
 }while(strncmp(linebuffer,"LOOKUP_TABLE",12)); /*until line with DIMENSIONS*/
 printf("reached lookup\n");
 for(iz=0;iz<nz;iz++)for(iy=0;iy<ny;iy++)for(ix=0;ix<nx;ix++)
 {
    x=x1+ix*dx;y=y1+iy*dy;z=z1+iz*dz;
    fgets(linebuffer,10000,infile);
    /* check if any hole hit*/
    holehit=0; /* not yet*/
    for(iA=-maxn;iA<=maxn;iA++)for(iC=-maxn;iC<=maxn;iC++)
    {
     rcomp=r;
     rcomp=rcomp*rcomp; /* use square*/
     if((x-iA*Ax-iC*Cx)*(x-iA*Ax-iC*Cx)+(z-iC*Cz)*(z-iC*Cz)<rcomp){holehit=1;break;} /*hole found*/
    }
    if (holehit==0){
          sscanf(linebuffer,"%lf",&fieldval);
          powsum+=fieldval*fieldval;
          numpoints++;
    }

 }/* vtk points loop*/
 fclose(infile);
 printf("%le,%s\n",powsum/numpoints, infilename);
   fprintf(outfile,"%le,%s\n",powsum/numpoints, infilename);
}/* end file loop*/

fclose(namesfile);
fclose(outfile);
exit(0);
}
```

List of abbreviations (alphabetic order):

ABC – absorbing boundary conditions

DOS – density of states (in this thesis: photonic density of states)

FDTD – finite-difference time-domain method

FFT – fast Fourier transform

FWHM – full width at half maximum

EM – electromagnetic

EOT – extraordinary optical transmission

MHA – metal hole array

MSM – multiple scattering method

PBG – photonic band gap

PhC – photonic crystal

PML – perfectly matched layer

PWEM – plane wave expansion method

QWIP – quantum well infrared photodetector

TMM – transfer matrix method

List of Publications

- **O. Glushko**, R. Meisels, F. Kuchar, *"Simulations of wave propagation and disorder in 3D non-close-packed colloidal photonic crystals with low refractive index contrast"*, Opt. Exp. **18**, 7101 (2010)
- E. Glushko, **A. Glushko**, V. Evteev, A. Stepanyuk, "*All-optical signal processing based on trapped modes of a photonic crystal resonator*" Proc. SPIE, Vol. **7354**, 75040l (2009)
- **O. Glushko**, R. Meisels, F. Kuchar, R. Danzer, *"Numerical and experimental investigations of surface roughness in 1D photonic crystals"*, J. Phys. Cond. Matt. **20**, 454220 (2008)
- L. Karachevtseva, **A. Glushko**, V. Ivanov, M. Karas, V. Onischenko, *"Polaritonic resonances in 2D silicon photonic crystals"* Proc. SPIE, Vol. **6588**, 65880X (2007)
- **A. Glushko** and L. Karachevtseva, *"PBG properties of three-component 2D photonic crystals"*, Phot. Nanostr. Fund. Apl. **4**, 141-145, (2006)
- **A. Glushko** and L. Karachevtseva, *"Photonic band structure of oxidized macroporous silicon"*, Opto-El. Rev. **14**, 201, (2006)
- **A. Glushko**, *"Plane wave method for out-of-plane propagation in 2D photonic crystals"*, Mathematical Methods in Electromagnetic Theory, MMET, Conference Proceedings, art. no. 1689805, pp. 406-408 (2006)
- **A. Glushko**, L Karachevtseva "*Band gap transformation in three-component 2D photonic crystals*", Proc. SPIE, **5950**, 59500g (2005)
- L. Karachevtseva, **A. Glushko**, M. Karas, V. Onischenko, "*Surface waves in 2D photonic macroporous silicon structures*" Proc. SPIE, **5733**, p. 297 (2005)

Acknowledgements

I would like to thank people who (directly or indirectly) helped me during my study in the Institute of Physics at the University of Leoben.
So, many thanks to

- *Em.O.Univ.-Prof. Friedemar Kuchar* for the opportunity to perform PhD study in Leoben, for a nice and professional supervision as well as for all the small but important things which I have learned from him

- *Ao.Univ.-Prof. Ronald Meisels* for his help with simulation programs, for installation of the cluster, for valuable discussions and explanations, and of course for reading and correcting all that what I've written including this thesis

- *Univ.-Prof. Oskar Paris* for his support of the final stage of my PhD study

- *Prof. Dr. DI. Kurt Hingerl* for taking time to read my thesis and to come to Leoben as second referee

- *Heide Kirchberger and Magdalena Ottrin* for their help with all the documents, for being always ready to answer questions and to solve problems

- *Peter Mocharitsch and Heinz Pirker* for the help in solving technical problems

- *all other members of the Institute of Physics* for a pleasant but working atmosphere. Personally *Franz Schmied* for being such a nice office-mate.

- *Stephan Kalchmair* from TU Wien for discussions of the EOT effect as well as for the experimental data

- *my father* for bringing me in Physics, and for his total support in the beginning of my career

- *Nadine* for her support and for making my life more complete

- *Elli-the-dog* for additional hours of fresh air and good mood